



저작자표시-비영리-변경금지 2.0 대한민국

이용자는 아래의 조건을 따르는 경우에 한하여 자유롭게

- 이 저작물을 복제, 배포, 전송, 전시, 공연 및 방송할 수 있습니다.

다음과 같은 조건을 따라야 합니다:



저작자표시. 귀하는 원저작자를 표시하여야 합니다.



비영리. 귀하는 이 저작물을 영리 목적으로 이용할 수 없습니다.



변경금지. 귀하는 이 저작물을 개작, 변형 또는 가공할 수 없습니다.

- 귀하는, 이 저작물의 재이용이나 배포의 경우, 이 저작물에 적용된 이용허락조건을 명확하게 나타내어야 합니다.
- 저작권자로부터 별도의 허가를 받으면 이러한 조건들은 적용되지 않습니다.

저작권법에 따른 이용자의 권리는 위의 내용에 의하여 영향을 받지 않습니다.

이것은 [이용허락규약\(Legal Code\)](#)을 이해하기 쉽게 요약한 것입니다.

[Disclaimer](#)

Thesis for the Degree of Master of Engineering

Understanding Ion Conduction in Multifunctional Polymer Electrolytes for Safe Energy Storage Devices



by
Yeon Hwa Song

Department of Polymer Engineering

The Graduate School

Pukyong National University

February 2020

Understanding Ion Conduction in Multifunctional Polymer Electrolytes for Safe Energy Storage Devices

(안전한 에너지 저장 장치를 위한
다기능 고분자 전해질의 이온 전도 이해)



Advisor: U Hyeok Choi

by

Yeon Hwa Song

A thesis submitted in partial fulfillment of the requirements for the degree of

Master of Engineering

in Department of Polymer Engineering, The Graduate School
Pukyong National University

February 2020

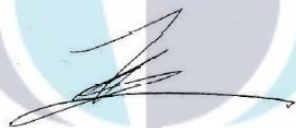
Understanding Ion Conduction in Multifunctional Polymer Electrolytes for Safe Energy Storage Devices

A thesis

by

Yeon Hwa Song

Approved by:



(Chairman) Prof. Youngho Eom



(Member) Prof. Seong Il Yoo



(Member) Prof. U Hyeok Choi

February 2020

Understanding Ion Conduction in Multifunctional Polymer Electrolytes for Safe Energy Storage Devices

Yeon Hwa Song

Department of Polymer Engineering, The Graduate School,
Pukyong National University

Abstract

In the development of next-generation safety all-solid-state energy storage devices, which not only have high current density, power density, and coulomb efficiency but also maintain these electrochemical properties under mechanical deformation, it is necessary to create multifunctional solid polymer electrolytes (SPEs) with high ionic conductivity and mechanical properties. The SPE may also be a promising alternative to replace conventional flammable liquid electrolytes that have explosion issues due to the formation of lithium dendrite between an electrode and an electrolyte. Therefore, there is a need to improve SPE with excellent electrical, mechanical, and electrochemical properties.

In this study, we prepared two different multifunctional SPEs; epoxy- and lithium acrylate-based SPEs. The epoxy-based SPEs containing ionic liquid, lithium solvating oligoether, and lithium salt show high ionic conductivity and flexibility due to their polymerization-induced microphase separation. The lithium acrylate-based SPEs, combined with cross-linkable vinyl silica nanoparticles (SNP) also exhibit high ionic conductivity and extreme stretchability. In order to understand ion transport mechanism in these SPEs, we systematically investigated their mechanical properties, ion conductivities, thermal stabilities, and morphology, using various experimental methods, such as dynamic mechanical analyzer, universal testing machine,

dielectric spectroscopy, impedance spectroscopy, differential scanning calorimetry, thermal gravimetric analysis, and Fourier transformation-infrared resonance spectroscopy.



안전한 에너지 저장 장치를 위한 다기능성 고체 고분자 전해질의 이온전도에 대한 이해

송 연 화

부경대학교 대학원 고분자공학과

요약

최근, 기계적 변형 하에서 전기 화학적 특성을 우수하게 유지하는 것과 동시에 고풍 특성이나 연신특성을 가지고 있는 다기능성 차세대 에너지 저장장치의 개발이 활발하게 진행되고 있다. 대표적인 에너지 저장장치로는 리튬이온 배터리와 슈퍼 커패시터가 있다. 이들은 양쪽 전극과 전극사이에 존재하는 전해질 및 분리막으로 구성되어 있다. 기존 에너지저장장치에 사용되던 액체전해질은 장시간 사용하는 경우 전극과 반대편 전극 사이에 리튬 덴드라이트를 형성하여 폭발이나 화재의 문제를 일으켰다. 이를 보완하기 위해 고체 고분자 전해질의 개발이 1960 년부터 현재까지 꾸준히 진행되어 오고 있다. 고체 고분자 전해질은 고상으로 이루어져 있어 기계적 변형 하에서 누수나 화재 같은 안정성 문제가 발생하지 않을 뿐 아니라 고분자 특성에 따른 다기능성까지 나타낼 수 있어 매우 촉망받는 재료로 떠오르고 있다.

본 연구에서는 기계적 물성이 우수한 에폭시 기반의 다기능성 고체 고분자 전해질과 연신 특성을 가진 리튬 아크릴레이트 기반의 고체 고분자 전해질에 대한 연구를 진행하였다. 첫번째로는 리튬 염과 리튬 이온을 해리 시켜 배위결합을 하는 올리고 에테르, 그리고 이온성 액체와 에폭시 매질을 혼합한 뒤 에폭시의 개환 중합을 통하여 에폭시 기반의 고체 고분자 전해질을 제작하였다. 전해질을 이루는 물질들과 에폭시와의 친화도에 의한 분자간 미세-상분리를 통해 나노 크기의 이온 채널과 에폭시 채널을 형성하였고 이는 높은 이온전도도 및 유연 특성 발현의 중요한 요인으로 역할을 하였다. 두번째는 표면에 비닐기를 포함하고 있는 실리카 나노 입자와 리튬 아크릴레이트 단분자를 라디칼 중합하여 실리카 나노 입자가 가교된 폴리리튬아크릴레이트 기반의 고체 고분자 전해질을 합성하였다. 분자내 기능기에 의해 연신특성을 가진 고분자와 응력이 집중 시 완충제 역할을 하는 실리카 입자에 의해 매우 높은 이온전도성을 함유하면서 우수한 신축성 및 복원 특성을 나타냈다.

동적 기계 분석기 (DMA), 범용 시험기 (UTM), 유전체 분광기 (DRS), 임피던스 분광기, 시차 주사 열량기 (DSC), 열중량 분석기 (TGA) 그리고 전계방출형 주사전자현미경 (Fe-SEM)과 에너지분산형 분광분석법 (EDS mapping)을 이용하여 각 다기능성 고체전해질의 기계적 특성, 이온전도도, 열 안정성 및 샘플 구조를 각각 측정하여 분석하였다.

Table of Contents

Table of Contents	iv
List of Figures	vi
List of Tables.....	xv
Acknowledgments	xvi
Chapter I. Introduction	1
I-1. Introduction and Motivation	1
I-1.1 Dual Ion Polymer Electrolytes	4
I-1.2 Single Ion Polymer Electrolytes.....	7
I-2. Background of Ion conduction in polymer electrolyte	9
I-2.1 Ion conductivity analysis.....	10
I-2.2 Dielectric relaxation analysis	13
I-3. References	15
Chapter II. Influence of Li salt concentration on Ion Conduction of epoxy-based solid polymer electrolyte for supercapacitors	18
II-1. Introduction	18
II-2. Experimental Section	25
II-2.1 Materials	25
II-2.2 Synthesis of epoxy-based solid polymer electrolyte.....	26
II-2.3 Fabrication of epoxy-based supercapacitor	27
II-2.4 Characterization.....	28
II-3. Result and Discussion	30
II-3.1 Thermal Analysis.....	30
II-3.2 Morphology	33
II-3.3 Ionic conductivity	38
II-3.4 Dielectric Relaxation	47
II-3.5 Mechanical Property	54
II-3.6 Electrochemical Property of Solid-State Supercapacitor.....	58
II-4. Conclusions	66
II-5. References	68

Chapter III. High Stretchable and Ion Conductive Lithium acrylate Hydrogel polymer electrolyte for stretchable supercapacitors.....	75
III-1. Introduction.....	75
III-2. Experimental Section.....	77
III-2.1 Materials	77
III-2.2 Synthesis of acrylic acid-based solid-state polymer electrolyte	78
III-2.3 Preparing stretchable all-solid-state supercapacitors	80
III-2.4 Characterization.....	81
III-3. Result and Discussion	83
III-3.1 Structural properties of PAALi-SNPs.....	83
III-3.2 Thermal Analysis.....	89
III-3.3 Ionic Conductivity	92
III-3.4 Mechanical Property.....	99
III-3.5 Morphology	101
III-3.6 Electrochemical Property of fiber-shaped supercapacitor	104
III-4. Conclusion	106
III-5. Reference	107

List of Figures

- Figure 1-1.** Development history of flexible electronic devices.
- Figure 1-2.** Schematic Process in Electrical Double Layer Capacitor (EDLC)
- Figure 1-3.** Angular frequency dependence of in-phase conductivity $\sigma'(\omega)$.
- Figure 1-4.** Schematic representation of dielectric relaxation process of ion-containing polymer electrolyte.
- Figure 2-1.** Schematic description of bicontinuous network morphology generation by PIMS. (a) A homogeneous mixture containing electrolyte (blue) components (TG, LiTf₂N, and BT) and epoxy (yellow) components [DEBA, methyl tetrahydrophthalic anhydride (MTA) curing agent, and N,N-dimethylbenzylamine (DMBA) catalyst] and showing chemical structures of each component. (b, c, and d) Varying LiTf₂N salt content tunes phase-separated morphology: (b) micro-scale phase separation, (c) nano-scale phase separation, and (d) less phase separation.
- Figure 2-2.** (a) Representative DSC thermogram of 2 M_70% with its T_gs, indicated by the arrows. Compositional variation of (b) the LiTf₂N

molarity and of (c) the weight fraction of BT (Φ_{BT}) in the glass transition temperature T_g for epoxy-based SPEs, where two T_g values are observed: T_g of epoxy-rich domain (T_g^{epo} , open symbols) and T_g of electrolyte-rich domain (T_g^{ele} , filled symbols). The horizontal dotted lines indicate T_g of pure epoxy (0%, black color), a mixture of TG and LiTf₂N (red color), and BT (blue color). The dashed and solid curves represent Fox prediction (Eq 2-1) and Gordon-Taylor equation fits (Eq 2-2 with $K = 15$ for T_g^{ele} and $K = 0.22$ for T_g^{epo}), respectively.

Figure 2-3. FE-SEM micrographs of (a) 0 M_70%, (b) 0.5 M_70%, (c) 1 M_70%, (d) 1.5 M_70%, (e) 2 M_70%, and (f) 4.5 M_70%, showing that the extraction of electrolyte components from SPE produces percolating pores (black regions) in a cross-linked epoxy matrix (bright regions), and the pore size decreases with increasing LiTf₂N molarity.

Figure 2-4. Angular frequency dependence of in-phase conductivity $\sigma'(\omega)$ at various temperatures from 120 to -30 °C. The horizontal dashed line indicates the DC ionic conductivity σ_{DC} .

Figure 2-5. Temperature dependence of ionic conductivity for (a) epoxy-based SPEs with different electrolyte contents ($\Phi_{LiTf_2N+TG+BT} = 30, 50$ or 70 wt%) and for (b) epoxy-based SPEs with and without BT: the solid

curves are the VTF equation fits (Eq 2-4). The insets in (a) and (b) show activation energies E_a s for ion conduction.

Figure 2-6. (a) Temperature dependence of ionic conductivity for epoxy-based SPEs with various LiTf₂N molarities (σ_{DC} vs T_0/T in the inset): the solid curves are VTF (Eq 4) fits to data. LiTf₂N molarity variation in (b) room temperature ionic conductivity of SPEs (σ_{DC}^{SPE} , filled symbols, left axis) and their corresponding pure electrolytes (σ_{DC}^{ele} , open symbols, left axis) and activation energy (E_a , X symbols, right axis), in (c) pre-exponential constant (A, filled symbols, left axis) and wavenumber difference ($\Delta\omega$, open symbols, right axis), and in (d) effective conductivity (σ_{eff}) and tortuosity (τ , in the inset): the solid and dashed lines are only guides for the eyes.

Figure 2-7. ATR-FTIR spectra of BMIM-Tf₂N, 0 M_70%, 0.5 M_70%, 1 M_70%, 1.5 M_70%, 2 M_70%, and 4.5 M_70% in the region from 1080 to 1020 cm⁻¹ at room temperature.

Figure 2-8. Dielectric derivative spectra ε_{der} at 253 K and their fits (solid lines) of the sum of a power law for electrode polarization (EP) and derivative forms of the HN function for MWS, α_2 , and α processes (dashed

lines) for (a) 0 M₇₀%, (b) 0.5 M₇₀%, (c) 1 M₇₀%, and (d) 1.5 M₇₀%.

Figure 2-9. (a and b) Angular frequency dependence of (a) dielectric derivative $\varepsilon_{\text{der}}(x\omega)$ and (b) dielectric permittivity $\varepsilon'(x\omega)$ at 253 K shifted by horizontal shift factor, x [0 M₇₀% ($x = 0.11$), 0.5 M₇₀% ($x = 0.09$), 1 M₇₀% ($x = 0.16$), and 1.5 M₇₀% ($x = 1.00$)], to superimpose in the region of electrode polarization; solid and dashed curves in (a) are fits of relaxation processes (Figure 2-8) and solid horizontal lines in (b) represent the static dielectric constant ε_s (Figure 2-10). The insets in (a) and (b) show $\Delta\varepsilon$ (filled symbols) and ε_s (open symbols) vs LiTf₂N molarity, respectively. (c) Angular frequency dependence of in-phase conductivity σ' (left axis, filled symbols) and ε_{der} (right axis, open symbols) for 0 M₇₀% and 0.5 M₇₀% at 263 K; solid horizontal lines indicates the DC conductivity σ_{DC} and dashed vertical lines are the relaxation peak frequencies of the MWS and α_2 .

Figure 2-10. Dielectric permittivity $\varepsilon'(\omega)$ of 1 M₇₀% at 253 K is comprised of frequency-dependent contributions from $\varepsilon'_{\alpha_2}(\omega)$ (blue dashed line), $\varepsilon'_{\alpha}(\omega)$ (green dashed line), and $\varepsilon'_{\beta}(\omega) + \varepsilon_{\infty}$ (orange dashed line).

The red solid line, corresponding to the sum of $\varepsilon'_{\alpha_2}(\omega)$, $\varepsilon'_{\alpha}(\omega)$, and $\varepsilon'_{\beta}(\omega) + \varepsilon_{\infty}$, indicates the static dielectric constant $\varepsilon_s = \varepsilon'_{\alpha_2}(\omega) + \varepsilon'_{\alpha}(\omega) + \varepsilon'_{\beta}(\omega) + \varepsilon_{\infty}$.

Figure 2-11. (a) Stress-strain curves of epoxy-based SPEs (0 M_70% in the inset) at room temperature. (b) Young's modulus (left axis, filled symbols) and elongation at break (right axis, open symbols) as a function of LiTf₂N molarity at room temperature.

Figure 2-12. (a and b) Correlation plots of ionic conductivity vs either (a) elongation at break or (b) Young's modulus at room temperature for all the SPE studied [X M_70% and 2 M_50% (= LiTf₂N+TG+BT_50%, LiTf₂N+DT+BT_50%, LiTf₂N+TG_50%, and LiTf₂N+DT_50%)], including literature data from ref 31, 64, and 65. Dashed lines are only guides for the eye. (c) Multifunctional plot of room temperature ionic conductivity (left axis, square symbols) and Young's modulus (right axis, circle + symbols) as a function of elongation at break. The only 1 M_70% SPE is located in the orange area, where SPE has $\sigma_{DC} \geq 10^{-4}$ S/cm, elongation at break > 100%, and Young's modulus > 0.1 MPa at the same time.

Figure 2-13. Electrochemical properties of all-solid-state supercapacitor composed of the epoxy-based SPE (1 M_70%) and two AC electrodes. (a)

Potential dependence of current density (CV profiles) at different scan rates from 10 to 100 mV/s with the inset showing a photograph of the supercapacitor pouch cell. (b) Time dependence of potential (GCD profiles) at various current densities from 0.1 to 1 A/g. (c) Specific capacitance vs. current density (square symbols, left and bottom axes) and Ragone plot of power density vs. energy density (circle symbols, right and top axes). (d) Capacitance retention as a function of cycle number (Nyquist plot of the supercapacitor before and after cycling in the inset). (e and f) Photographs show the device powering a LED.

Figure 2-14. Ragone plot of power density vs. energy density of our supercapacitor, compared with literature values.

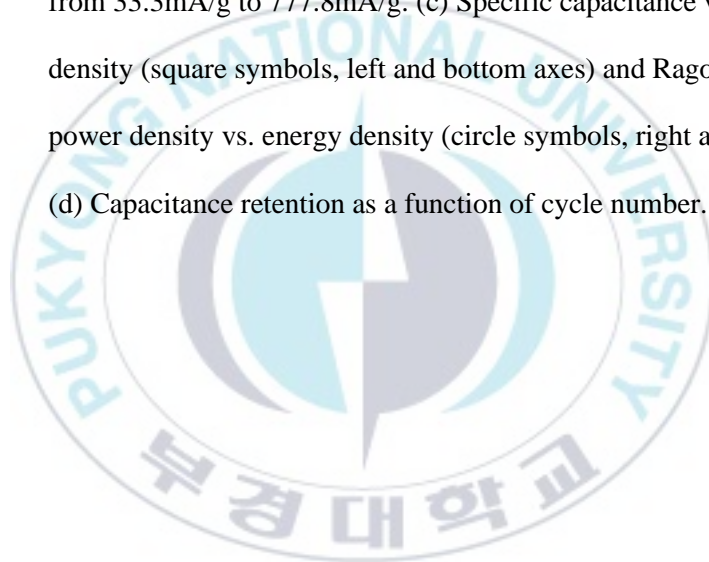
Figure 2-15. (a) Bending and rolling tests of epoxy/AC-based supercapacitor demonstrating a good flexibility. (b) CV curve comparison at 20 mV/s of flat (initial), bending, rolling, and flat (recovery) states, where no obvious change of capacitance is observed. (c) Specific capacitance obtained from GCD test at a current density of 0.7 A/g under four different mechanical deformation conditions. (d) Capacitance retention at a current density of 0.7 A/g under rolling. (e and f) Photographs show the supercapacitor powering a LED under (e) bending and (f) rolling.

- Figure 3-1.** Synthesis of (a) vinyl silica nanoparticles, (b) lithium acrylate, and (C) poly(lithium acrylate) containing SNPs
- Figure 3-2.** (a) FT-IR spectrum of VTES and SNPs (b) m-TEM (Transmission electron microscope) image of SNPs
- Figure 3-3.** ICP (Inductively coupled plasma) data of lithium acrylate monomer
- Figure 3-4.** (a) Representative FT-IR spectrum of PAA-SNPs and PAALi-SNPs
(b) The $3700 - 2800\text{ cm}^{-1}$ spectral region in OH peak (dashed curves in (b) are gaussian fitting of OH peaks)
- Figure 3-5.** The DSC thermograms (a) PAA-SNPs (inset figure magnification of melting point) (b) PAALi-SNPs
- Figure 3-6.** Temperature dependence on ionic conductivity and solid curves are VTF fitting Eq 3-1. (a) PAA-SNPs and PAALi-SNPs (b) Compare DC conductivity at 298K of PAA-SNPs and PAALi-SNPs
- Figure 3-7.** (a) The temperature dependence on ionic conductivity of different ratio of AALi monomer (5.49 m, 8.24 m, and 10.98 m) and solid curves are VTF fitting Eq 3-1. (b) Compare DC conductivity at 298K (pristine and after heating at $100\text{ }^{\circ}\text{C}$) of different ratio of SPEs.

- Figure 3-8.** The ionic conductivity σ_{DC} of PAALi-SNPs with various content of SNPs at 298K. (Inset figure explains in-phase part of conductivity $\sigma'(\omega)$ as a function of angular frequency for the SPEs)
- Figure 3-9.** The ionic conductivity σ_{DC} of PAALi-SNPs with various content of water at 298K. (Inset figure explains in-phase part of conductivity $\sigma'(\omega)$ as a function of angular frequency for the SPEs)
- Figure 3-10.** (a) Stress-strain curve of PAA-SNPs and PAALi-SNPs (b) Tensile strength of SPEs (c) Elongation break of SPEs
- Figure 3-11.** (a) Stress-strain curve of PAA-SNPs and PAALi-SNPs (b) Tensile strength of SPEs (c) Elongation break of SPEs
- Figure 3-12.** (a) Cross-sectional FE-SEM of PAA-SNPs (b-c) Elemental mapping of (b) carbon and (c) silica. (d) Overlapping image showing (a) and (c). (e) Cross-sectional FE-SEM of PAALi-SNPs (f-g) Elemental mapping of (f) carbon and (g) silica. (h) Overlapping image showing (e) and (g).
- Figure 3-13.** Cross-sectional FE-SEM of PAALi-SNPs_50wt% (b-c) Elemental mapping of (b) carbon and (c) silica. (d) Overlapping image showing (a) and (c). (e) Cross-sectional FE-SEM of PAALi-SNPs_60wt% (f-g) Elemental mapping of (f) carbon and (g) silica. (h) Overlapping image showing (e) and (g).

Figure 3-14. Appearance of Poly(lithium acrylate) SPEs with different ratio of SNPs

Figure 3-15. Electrochemical properties of fiber-shaped supercapacitor composed of the lithium acrylate-based SPE (PAALi-SNPs_20wt%). (a) Cyclic Voltammetry profiles at different scan rates from 10 to 100mV/s. (b) Galvanostatic charge-discharge profiles at various current densities from 33.3mA/g to 777.8mA/g. (c) Specific capacitance vs. current density (square symbols, left and bottom axes) and Ragone plot of power density vs. energy density (circle symbols, right and top axes). (d) Capacitance retention as a function of cycle number.



List of Tables

- Table 2-1.** Fitting Parameters of the VTF Equation for DC Conductivity, Eq 2-4
- Table 2-2.** Electrochemical Performance of Either SPE- or GPE-based Supercapacitors
- Table 3-1.** Main peaks in the FT-IR spectrum of SNPs with their assignment according to refs.
- Table 3-2.** All peaks in the FT-IR spectrum of PAA-SNPs and PAALi-SNP with their assignment according to refs.
- Table 3-3.** Fitting Parameters of the VTF Equation for different charge carrier's DC conductivity, Eq 3-1.
- Table 3-4.** Fitting Parameters of the VTF Equation for different ratio of monomer's DC conductivity, Eq 3-1.

Acknowledgments

학부과정부터 석사과정까지 꾸준히 밝음을 유지하면서 즐겁게 학위 논문을 완성할 수 있었습니다. 많은 분들의 도움이 없었다면 이는 불가능했기에 감사의 말씀을 전합니다.

가장 먼저, 부족하고 모자람 많은 학생인 저를 항상 믿고 길러주신 저의 인생 멘토, **최우혁 교수님**께 먼저 감사의 말씀을 드립니다. 교수님의 지도 하에서 공부하면서 손으로 셀 수 없이 수많은 본받을 점이 있었지만 그 중 공부가 재밌어지는 방법을 배울 수 있어서 정말 행복했습니다. 늘 무엇을 하고 싶은 지, 왜 그런 지에 대해 고민할 수 있는 기회를 주시며 막힐 때면 저와 보폭을 맞춰 주시면서 걸어갈 수 있는 방법에 대해 알려주셨기에 전공에 대한 애착과 사랑을 가질 수 있었습니다.

학, 석사 과정동안 고분자에 대한 흥미와 애정을 가질 수 있게 명강의를 해 주신 **민성기 교수님, 박찬영 교수님, 이봉 교수님, 박상보 교수님, 이원기 교수님, 김주현 교수님**, 그리고 저의 논문 심사를 맡아 주신 **유성일 교수님, 엄영호 교수님**께 깊은 감사의 마음을 드립니다.

저의 대학원 절친(B.F.F)이자 영혼의 랩 메이트인 **puij**, LiMFSI 합성의 대가이자 하나뿐인 랩실 동기 **호균선배**, 광명 찾고 실험 열심히 하는 **민웅선배**, 남다른 친화력과 사려 깊은 마음을 가진 아기같은 **지원이**, 언제나 즐겁고 이야기하는 것을 좋아하는 **효정이**, 학점 많이 들어서 힘들지만 파이팅 넘치는 **영수**, 주경야독하며 브리토를 사랑하는 **준성선배**까지 고분자에너지재료 식구들이라는 든든한 버팀목이 있어 지치지 않고 ‘에너지자이저’처럼 즐겁게 생활할 수 있었기에 감사의 마음을 전합니다.

다른건 안 되도 고기는 사줄 수 있다고 하시던 **성국선배**, 그것도 모르냐며 항상 챙겨 주시는 촌테레 **재영선배**, 두 분의 식사생활 선배님이 계셨기에 방향을 잃지 않고 앞으로 나아갈 수 있었습니다. 도시 남자 같지만 알고 보면 되게 순박한 매력을 가진 진모델 **호철선배**, 누구보다 멋있는 식사가 될 매력부자 손존잘 **동환선배**, 이 두 분의 크로스피터들 덕분에 정신도 몸도 모두 건강한 식사생활을 할 수 있었습니다. 고민이 있을 때면 언제든 달려와주는 119 같은 8년지기 친구 **예진이**, 그리고 항상 옆에서 힘이 되어주며 저의 돌파구가 되어주는 **동근선배**가 있었기에 천군만마를 얻은 장수처럼 든든하게 생활할 수 있었습니다. 저의 친구로 존재해주고 의지할 수 있게 해준 친구들에게 고마운 마음을 전합니다.

마지막으로 제가 세상에서 가장 사랑하는 우리 아빠 **송유중**, 엄마 **손진숙**, 그리고 하나뿐인 내 동생 **호정**에게 감사의 마음을 전합니다. 제가 어떠한 결정을 하든지 항상 믿어 주시고 지원해 주시며 세상을 행복하게 바라보는 제가 존재할 수 있게 해주셔서 감사드립니다. 그리고 사랑합니다.

2020 년 02 월

송 연 화 올림



Chapter I. Introduction

I-1. Introduction and Motivation

In 2008, the concepts of developing a flexible display were first conceived by Nokia Morph. A few years after the first flexible concept was released, Samsung and Nokia exhibited a curved prototype. Recently, Samsung launched a new foldable phone in 2019 (See Figure 1). With the rapid development of portable and wearable devices such as roll-up displays, foldable cell phones, smartwatches, and electronic skins, it is necessary to develop flexible and stretchable energy storage devices, for example, lithium-ion batteries or supercapacitors.¹⁻⁵

To realize such advanced flexible devices, high capacitance, energy density, columbic efficiency, and electrochemical retention must be maintained, even at high mechanical strains. In spite of the numerous efforts on the design and fabrication of wearable electronic applications,⁶ it is still challenging to assemble a high-performing flexible energy storage device into the wearable and portable systems.⁷

Conventional energy storage devices are composed of electrodes (cathode and anode), separator, and liquid electrolyte. During stretching or deformation, however, the devices have some critical issues, which are leakage of harmful liquid electrolyte, causing, environmental problems, as well as an acceleration of lithium dendrite growth, leading to safety problems.^{8,9}

To overcome these problems, solid polymer electrolytes (SPEs) are widely envisioned to be promising materials to replace for conventional liquid electrolytes, because SPE has dimensional stability and outstanding mechanical properties.

However, developing SPE with good ion transport properties has been challenging owing to the strong coupling between ion motion and polymeric segmental dynamics. One approach to the enhancement of ion transport in a polymeric medium is to prepare SPEs by mixing ion solvating polymer with lithium salts or ionic liquids,^{10,11} which is a dual-ion conductor. The other way to increase ion transport is to prepare a single-ion conductor (so-called ionomer),¹²⁻¹⁴ where the one type of ions (either cation or anion) is covalently attached to polymers, thus the other ion only becoming mobile. In this study, to develop electrically high ion-conducting and mechanically stable SPE for the development of safety energy storage applications, we studied epoxy-based SPEs (dual-ion conductors) and lithium acrylate-based SPEs (single-ion conductors), shown in chapter 2 and 3, respectively.

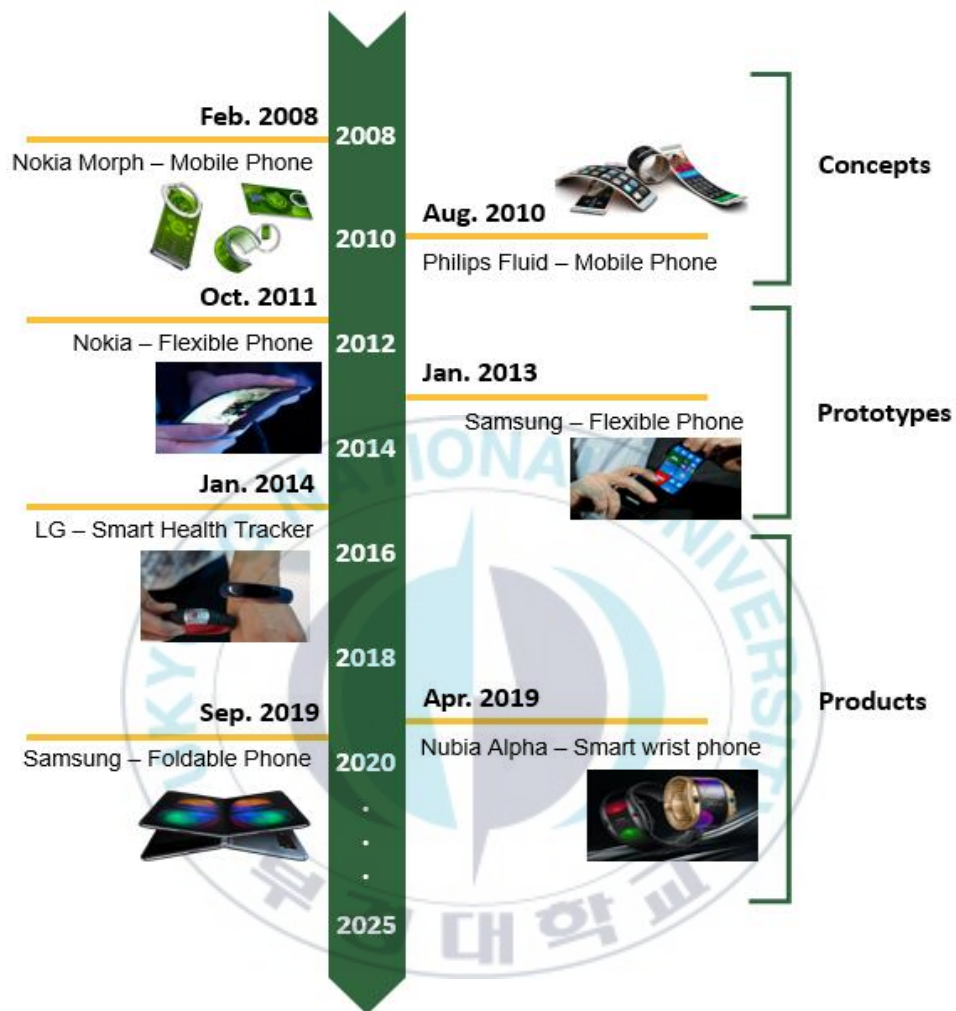


Figure 1-1. Development history of flexible electronic devices.¹⁵

I-1.1 Dual Ion Polymer Electrolytes

Usually, molten salts, dissolved in organic solvents, and ionic liquids are used as commercial dual ion electrolytes as a substance with both cations and anions that contribute to the ionic conduction. However, these electrolytes are in a liquid-state that could lead to safety issues (such as flammability and explosion). In many alternatives, dual ion polymer electrolytes have been intensively studied for several decades.

High ionic conductivity is one of the parameters that can determine whether polymer electrolytes have a good performance. To achieve high ionic conductivity, many researchers have developed many types of dual ion electrolytes.

The first type is generally fabricated from lithium salts and ionic liquids dissolved in a stable alkaline ion-solvating polymer matrix. Yang et al. synthesized poly(ethylene oxide) based dual ion polymer electrolytes blending with a lithium salt and ionic liquid.¹⁶ The parts of ether oxygen on a PEO make cation separate from ionic liquids by coordinating with cations that lead to increase ionic conductivity.

The second type is molten salt solvating in ionic liquid combined with the polymer matrix. Watanabe et al. prepared poly(methyl methacrylate) based dual ion polymer electrolytes by mixing it with a glyme-Li salt solvate ionic liquid¹⁷. A solvating ionic liquid, $\text{Li}(\text{G4})_1[\text{TFSA}]$ is selected because they serve as non-flammable plasticizers and ion charge carriers.

Third, Ionic liquids dissolved in the functionalized polymer matrix. Kim et. al prepared thermoplastic polyurethane-based dual ion polymer electrolytes embedding an ionic liquid, 1-ethyl-3-methyl imidazolium bis(trifluoromethyl sulfonyl)imide.¹⁸ These polymer electrolytes exhibit not only ionic conductivity but also transparent and stretchable ability by inheriting polymer properties.

Last, disperse fillers into the polymer electrolytes matrix. This system is usually known by composite polymer electrolytes (CPEs). CPEs can be one of the ways to enhance mechanical properties without sacrificing ionic conductivity. Chen et.al used ordered mesoporous material SBA-15 in a poly(ethylene oxide) based dual ion polymer electrolytes.¹⁹ SBA-15 acts as a physical cross-linking center of polymer chains and improves the mechanical stability of the electrolyte.

Dual ion electrolytes can be also used at an electric double-layer capacitor (EDLC), where the charge separation creates the Helmholtz double-layer, resulting in double-layer capacitance. Since EDLC needs to double layer at the interface between electrode and electrolyte, the dual-ion electrolytes can be one of the ideal systems for supercapacitors.

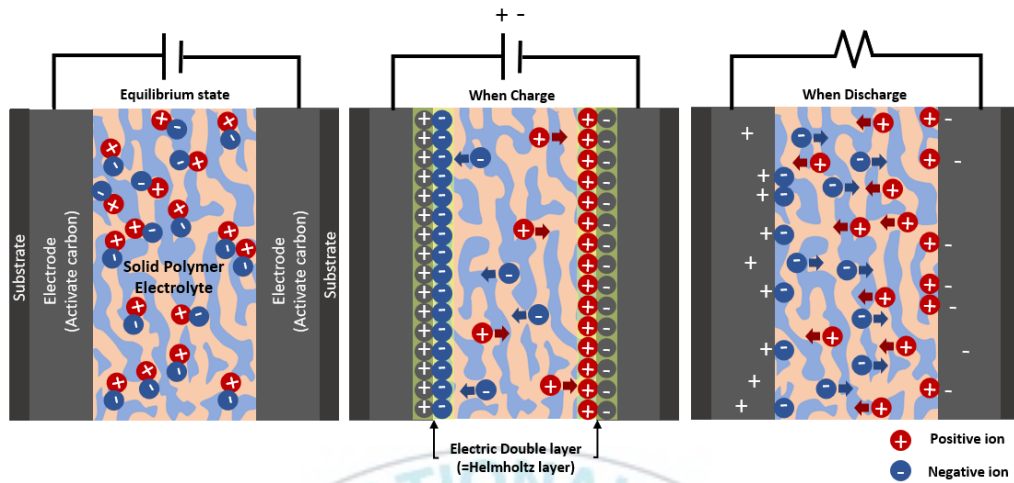


Figure 1-2. Schematic Process in Electrical Double Layer Capacitor (EDLC)

I-1.2 Single Ion Polymer Electrolytes

When the only one type of ions, either cation or anion, is mobile under an applied electric field, the electrolyte is a single-ion electrolyte. In the electrolyte for lithium-ion batteries, it is an advantage to create channels for ionic charge carriers between the cathode and anode.²⁰ When dual ion electrolytes are used in lithium-ion batteries, both lithium cations and anions can move between the cathode and anode during the charge and discharge process, indicating lower lithium transference number less than 1. This leads to severe concentration polarization at the interface of the electrolyte and electrode and also restricts the performance of lithium-ion batteries.²¹ On the other hand, single-ion electrolytes with high lithium-ion transference number (closed to unity) are suitable in lithium-ion batteries. In 1993, Newman et al. reported that high transference number ($t_{Li} = 1$) would improve battery performance as compared to low transference number ($t_{Li} = 0.3$).²²

There are a lot of efforts to restrict the anion movement using primary or secondary bonds, producing a high transference number, like ionomers. Colby et al. reported polysiloxane based single ion electrolytes containing weak-binding novel anionic borates and cyclic carbonate as side chains.²³ Polysiloxane-based single ion electrolyte shows relatively high conducting ion (cation) content and low activation energy. Myes et al. prepared poly(ethylene oxide) block copolymer-based single ion electrolytes, and the block copolymer allows providing microphase separation into the electrolyte.²⁴ Lithium-ion is dissociated from carboxylate anions and easily migrated

into the other domain, resulting in an increase in the ionic conductivity to 10^{-5} S/cm) at 70 °C and preventing anions from migrating to the electrode.

However, single-ion conductors usually have a low conductivity property. In order to overcome the drawback, Choi et al. proposed functionalized single-ion conducting mesoporous silica nanoparticles that can be incorporated into the PEO matrix as hybrid nanocomposite SPE.¹⁴ Incorporating mesoporous silica nanoparticles affords ionic conductivity and boosts mechanical property at the same time.

Recently, there are many types of development for multifunctional single ion polymer conductors. Hydrogel having environmentally-friendly (medium is water) and elastic properties (highly stretchable) is the one type of single ion polymer conductor. Polyacrylic acid (PAA)²⁵, polyacrylamide (PAM)²⁶ and polyvinyl alcohol (PVA)²⁷ are widely used in hydrogel-based single-ion conductors because of the functional groups of each polymer, which provides solubility in a water and elasticity, self-healing properties.

I-2. Background of Ion conduction in polymer electrolyte

Among the properties of polymer electrolytes, ion conduction is an important key for use as an energy storage device. In general, polymers do not contain ions, so they do not have ion conduction properties. However, polymer electrolytes contain ions, and thus they are influenced by ions, resulting in ion conduction properties and dynamic intrinsic properties. To determine ion conduction and dielectric relaxation, electrical and dielectric measurements are used by analyzing the complex conductivity and dielectric functions over a wide frequency range. Therefore, analyzing the ionic behavior of the polymer electrolyte and the relaxation of the dielectric is important to understand the ion conductivity of the polymer electrolyte.

I-2.1 Ion conductivity analysis

Ion conductivity refers to the properties of ions and dipole moment molecules in a polymer matrix when they move directionally by an external electric field. Ion conductivity can be expressed as a complex function. The complex function of ion conductivity came from the complex dielectric function, Eq. 1-2 by measuring the complex impedance, Eq. 1-1. The complex function was appeared due to the lag of the orientation of any dipoles in the electric displacement.²⁸

$$Z^*(\omega) = Z'(\omega) + iZ''(\omega) \quad (1-1)$$

$$\varepsilon^*(\omega) = \varepsilon'(\omega) + i\varepsilon''(\omega) \quad (1-2)$$

To get the value of ion conductivity, the complex functions can be defined by following equation 1-3 and 1-4, where C_0 is the vacuum capacitance, ω is the angular frequency, ε_0 is the vacuum permittivity, L is the distance between the electrodes (top, bottom), and A is the area of electrode.²⁹

$$\varepsilon^*(\omega) = \frac{1}{C_0} \frac{1}{i\omega Z^*(\omega)} = \frac{L}{A \varepsilon_0} \frac{1}{i\omega Z^*(\omega)} \quad (1-3)$$

$$\sigma^*(\omega) = i\omega \varepsilon_0 \varepsilon^*(\omega) \quad (1-4)$$

Using the above equations, we can get the complex ion conductivity function which divided by the real part (σ') and imaginary part (σ'') of ion conductivity (See Eq. 1-5).

$$\sigma^*(\omega) = \sigma'(\omega) + i\sigma''(\omega) \quad (1-5)$$

The real part (σ') of ion conductivity in a wide range of frequency can find DC conductivity that is the point where is the steady-state of the real part (in-phase) of ion conductivity at any frequency even if the direction of the electric field changes.

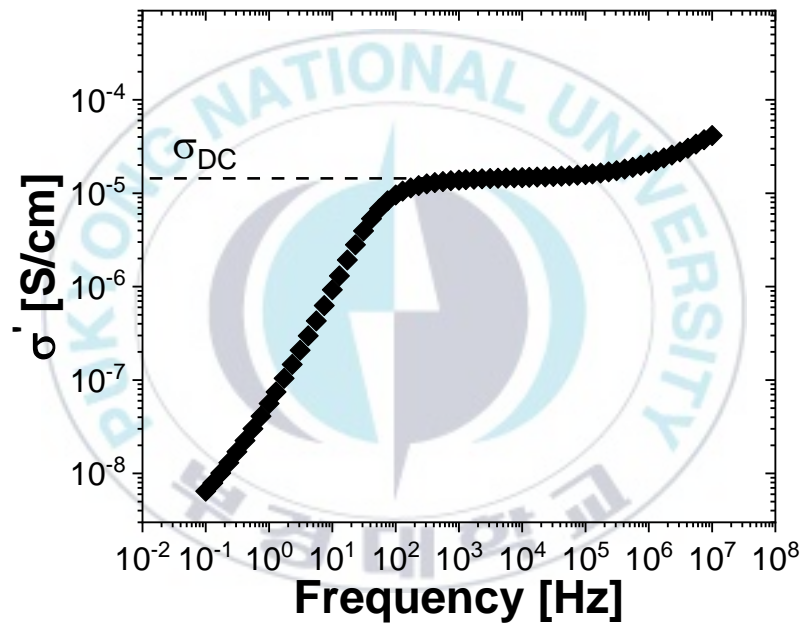
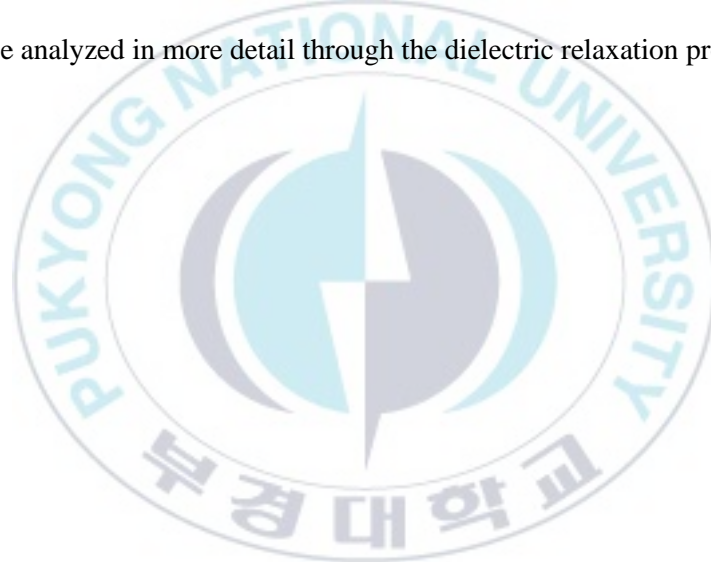


Figure 1-1. Angular frequency dependence of in-phase conductivity $\sigma'(\omega)$.

Moreover, ionic conductivity could provide information about the characteristic of polymer electrolytes. It can be divided into three parameters: the electric charge ($e = 1.6 * 10^{-19}$ C), the ion mobility (μ), and the number density of conducting ions (ρ), as shown in equation 1-6.

$$\sigma = e * \mu * \rho \quad (1-6)$$

The ion mobility μ in polymer electrolyte means polymer segmental motion, which can be analyzed in more detail through the dielectric relaxation process.



I-2.2 Dielectric relaxation analysis

Dielectric relaxation is the lag in the molecular polarization of the material with an alternating electric field. Ion-containing polymer electrolyte generally appeared four major processes of polarization: dipolar local relaxation (β), segmental relaxation (α), hopping polarization (α_2) and electrode polarization (EP) (See Figure I-2).

Dipolar local relaxation (β) is associated with the localized rotation of molecules and can move even at relatively low temperatures. So, β appears at high frequencies among four major processes of polarization. The segmental relaxation (α) is related to dynamic glass transition and the motion of polymer chains is bigger than β , so that it needs more time (lower frequency). Both of β and α process are related to orientational polarization. After relaxation by the polymer chains at high frequencies (faster motion), the hopping polarization (α_2) that ions exchange between ion states was observed due to ionic orientational polarization. EP has occurred at low frequencies (lowest motion), where the ions in electrolyte have enough time to move the blocking electrode.

To analysis dielectric relaxation (α_2 and α) in ion-containing polymer electrolytes, Havriliak-Negami (HN) functions can be used at dielectric loss derivative spectra. Furthermore, a physical model of electrode polarization (EP) can separate ionic conductivity (Eq. 1-6) into the number density of conducting ions and trapped ion fraction and their mobility.^{13,31,32}

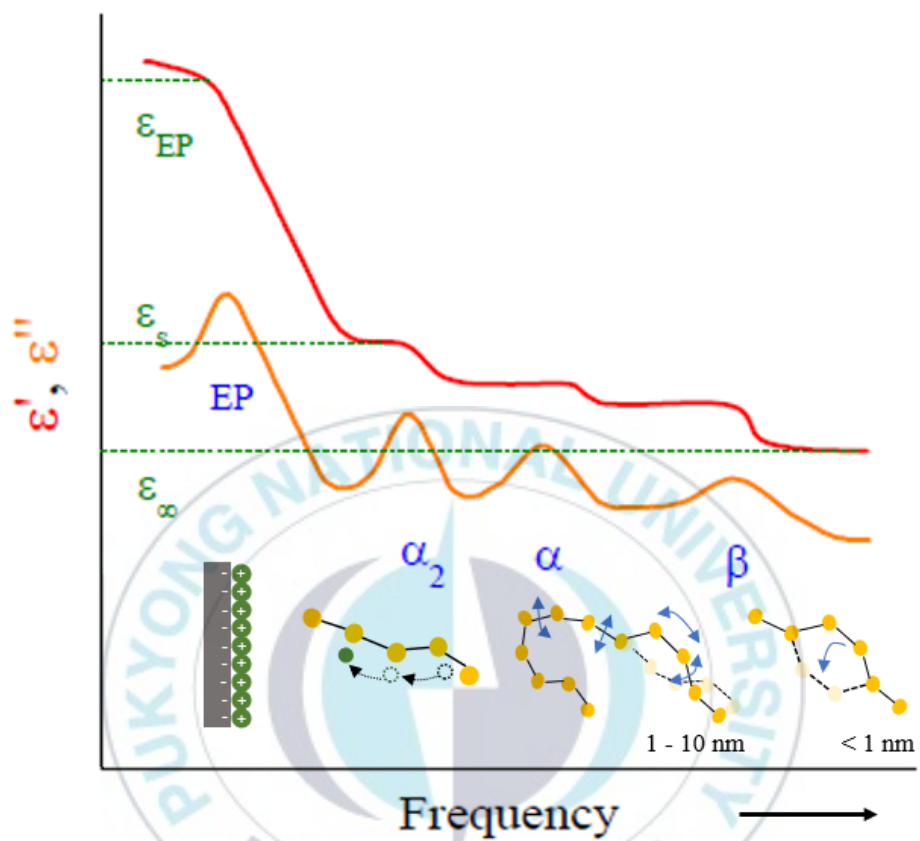


Figure 1-3. Schematic representation of the dielectric relaxation process of ion-containing polymer electrolyte.³⁰

I-3. References

1. Dong, L. *et al.* Flexible electrodes and supercapacitors for wearable energy storage: A review by category. *J. Mater. Chem. A* **4**, 4659–4685 (2016).
2. Pan, S., Ren, J., Fang, X. & Peng, H. Integration: An Effective Strategy to Develop Multifunctional Energy Storage Devices. *Adv. Energy Mater.* **6**, 1–19 (2016).
3. Yao, B. *et al.* Paper-Based Electrodes for Flexible Energy Storage Devices. **1700107**, (2017).
4. Wang, X., Liu, Z. & Zhang, T. Flexible Sensing Electronics for Wearable/Attachable Health Monitoring. *Small* **13**, 1–19 (2017).
5. Lee, S., Jeong, D., Mativenga, M. & Jang, J. Highly Robust Bendable Oxide Thin-Film Transistors on Polyimide Substrates via Mesh and Strip Patterning of Device Layers. *Adv. Funct. Mater.* **27**, 1–9 (2017).
6. Heo, J. S., Eom, J., Kim, Y. H. & Park, S. K. Recent Progress of Textile-Based Wearable Electronics: A Comprehensive Review of Materials, Devices, and Applications. *Small* **14**, 1–16 (2018).
7. Chen, X., Rogers, J. A., Lacour, S. P., Hu, W. & Kim, D. H. Materials chemistry in flexible electronics. *Chem. Soc. Rev.* **48**, 1431–1433 (2019).
8. Snyder, J. F., Carter, R. H. & Wetzel, E. D. Electrochemical and mechanical behavior in mechanically robust solid polymer electrolytes for use in multifunctional structural batteries. *Chem. Mater.* **19**, 3793–3801 (2007).
9. Re, N. I ss ue s and challenge s facing rechargeable lithium batterie s. 359–367 (1972).
10. Kwon, S. J., Kim, T., Jung, B. M., Lee, S. B. & Choi, U. H. Multifunctional Epoxy-Based Solid Polymer Electrolytes for Solid-State Supercapacitors. *ACS Appl. Mater. Interfaces* **acsami.8b11016** (2018). doi:10.1021/acsami.8b11016
11. Jang, H. K., Jung, B. M., Choi, U. H. & Lee, S. B. Ion Conduction and Viscoelastic Response of Epoxy-Based Solid Polymer Electrolytes Containing Solvating Plastic Crystal Plasticizer. *Macromol. Chem. Phys.* **219**, (2018).
12. Lee, M., Kwon, Y. K., Kim, J. & Choi, U. H. Effect of Poly(ethylene glycol) Crystallization on Ionic Conduction and Dielectric Response of Imidazolium-Based Copolyester Ionomers. *Macromolecules* **52**, 2314–2328 (2019).

13. Choi, U. H. *et al.* Ionic conduction and dielectric response of poly(imidazolium acrylate) ionomers. *Macromolecules* **45**, 3974–3985 (2012).
14. Kim, Y. *et al.* High Ion Conducting Nanohybrid Solid Polymer Electrolytes via Single-Ion Conducting Mesoporous Organosilica in Poly(ethylene oxide). *Chem. Mater.* **29**, 4401–4410 (2017).
15. Dai, Liming, Zhi, C. *Flexible Energy Conversion and Storage Devices*. Wiley-VCH (2018).
16. Zhu, C., Cheng, H. & Yang, Y. Electrochemical characterization of two types of PEO-based polymer electrolytes with room-temperature ionic liquids. *J. Electrochem. Soc.* **155**, 569–575 (2008).
17. Kido, R. *et al.* Li⁺ Ion Transport in Polymer Electrolytes Based on a Glyme-Li Salt Solvate Ionic Liquid. *Electrochim. Acta* **175**, 5–12 (2015).
18. Jin, M. L. *et al.* An Ultrasensitive, Visco-Poroelastic Artificial Mechanotransducer Skin Inspired by Piezo2 Protein in Mammalian Merkel Cells. *Adv. Mater.* **29**, 1–9 (2017).
19. Zhou, J. & Fedkiw, P. S. Ionic conductivity of composite electrolytes based on oligo(ethylene oxide) and fumed oxides. *Solid State Ionics* **166**, 275–293 (2004).
20. Amereller, M. *et al.* Electrolytes for lithium and lithium ion batteries: From synthesis of novel lithium borates and ionic liquids to development of novel measurement methods. *Prog. Solid State Chem.* **42**, 39–56 (2014).
21. Fuller, T. F., Doyle, M. & Newman, J. Simulation and Optimization of the Dual Lithium Ion Insertion Cell. *J. Electrochem. Soc.* **141**, 1–10 (1994).
22. Doyle, M., Fuller, T. F. & Newman, J. The importance of the lithium ion transference number in lithium/polymer cells. *Electrochim. Acta* **39**, 2073–2081 (1994).
23. Liang, S., Choi, U. H., Liu, W., Runt, J. & Colby, R. H. Synthesis and Lithium Ion Conduction of Polysiloxane Single-Ion Conductors Containing Novel Weak-Binding Borates. (2012). doi:10.1021/cm3005387
24. Ryu, S. W. *et al.* Effect of counter ion placement on conductivity in single-ion conducting block copolymer electrolytes. *J. Electrochem. Soc.* **152**, 158–163 (2005).
25. Huang, Y. *et al.* A self-healable and highly stretchable supercapacitor based on a dual crosslinked polyelectrolyte. *Nat. Commun.* **6**, 1–8 (2015).

26. Huang, Y. *et al.* An Intrinsically Stretchable and Compressible Supercapacitor Containing a Polyacrylamide Hydrogel Electrolyte. 9269–9273 (2017). doi:10.1002/ange.201705212
27. Wang, Z., Tao, F. & Pan, Q. A self-healable polyvinyl alcohol-based hydrogel electrolyte for smart electrochemical capacitors. *J. Mater. Chem. A* **4**, 17732–17739 (2016).
28. Barsoukov, E. & Macdonald, J. R. *Impedance Spectroscopy: Theory, Experiment, and Applications*. *Journal of Applied Electrochemistry* **125**, (John Wiley & Sons, Inc., 2005).
29. Choi, U. H. & Jung, B. M. Ion Conduction, Dielectric and Mechanical Properties of Epoxy-Based Solid Polymer Electrolytes Containing Succinonitrile. *Macromol. Res.* **26**, 459–465 (2018).
30. Choi, U.H. “Understanding Ion Transport In Ion-Containing Polymers For Energy Applications” PhD diss., The Pennsylvania State University (2012)
31. Macdonald, J. R. Theory of ac space-charge polarization effects in photoconductors, semiconductors, and electrolytes. *Phys. Rev.* **92**, 4–17 (1953).
32. R Coelho. Sur la relaxation d’une charge d’espace. *Rev. phys. Appl.* **18**, 137–146 (1983).

Chapter II. Influence of Li salt concentration on Ion Conduction of epoxy-based solid polymer electrolyte for supercapacitors

II-1. Introduction

In recent years, highly flexible and stable energy storage devices are of great interest for a wide range of applications in wearable electronic or health systems and bendable displays.¹⁻⁶ In order to realize such an advanced flexible energy device, it is desirable to sustainably store and release energy for these devices, even under high mechanical deformation, and also to easily control or integrate multifunctional properties into such a functional device. In spite of the numerous efforts on the design and fabrication of wearable electronic applications,⁷ it is still challenging to assemble a high-performing flexible energy storage device, which should be solid-state, into the wearable and portable systems.^{8,9} Therefore, it is necessary to replace a conventional liquid electrolyte with a robust solid electrolyte, thereby allowing not only for leakage prevention of the harmful and flammable liquid electrolyte from the devices, but also for more adaptable designs for the incorporation of the physical features, such as flexibility, stability, and sustainability, during system integration.

Among various solid-state electrolytes,^{10–13} solid polymer electrolytes (SPEs) have received significant attention due to their multifunctional characteristics of flexibility, thin-film forming ability, nonflammability, and electrochemical stability.^{14–18} In 1973, Wright et al. first reported the alkali metal salt-containing poly(ethylene oxide) (PEO)-based SPE, and these materials have been extensively studied since.¹⁹ The alkali metal ion (either sodium or lithium) transport in the PEO-based SPEs was assisted by ion-solvating polymer segmental motion, so that their ionic conductivities (σ_{DC}) followed a Vogel-temperature dependence, indicating that a lower glass transition temperature (T_g) results in higher σ_{DC} . Such a coupling ion dynamics with polymer chains, however, leads a relatively lower ionic conductivity of the SPE ($< 10^{-5}$ S/cm at 25 °C), compared to that of the counterpart liquid electrolyte ($\sim 10^{-3}$ S/cm at 25 °C). To overcome the low ionic conductivity of the SPE, gel polymer electrolytes (GPEs), composed of liquid solvent (such as propylene carbonate, ethylene carbonate, or their 1:1 mixture), ion salt, and their mechanical supporting polymer matrix [for example, poly(vinylidene fluoride), poly(acrylonitrile), or poly(vinyl alcohol)], have been considered as promising solutions.²⁰ The organic polar liquid solvents with a high dielectric constant ($\epsilon > 60$) allow not only to lower T_g , thereby giving rise to fast segmental motion of polymer chain, but also to facilitate the dissolution of salts, thus increasing conducting charge carrier concentration. As a result, these plasticizing and solvating effects enable a significant increase in σ_{DC} value, which is close to that of the liquid electrolyte, but the addition of liquid solvent concurrently leads to a profound reduction in the

mechanical strength of the GPEs, resulting in a recurrence of the safety problem observed in liquid electrolytes. Therefore, it is necessary to decouple and independently control these two conflicted physical properties, allowing for a simultaneous increase in the ionic conductivity and mechanical modulus.

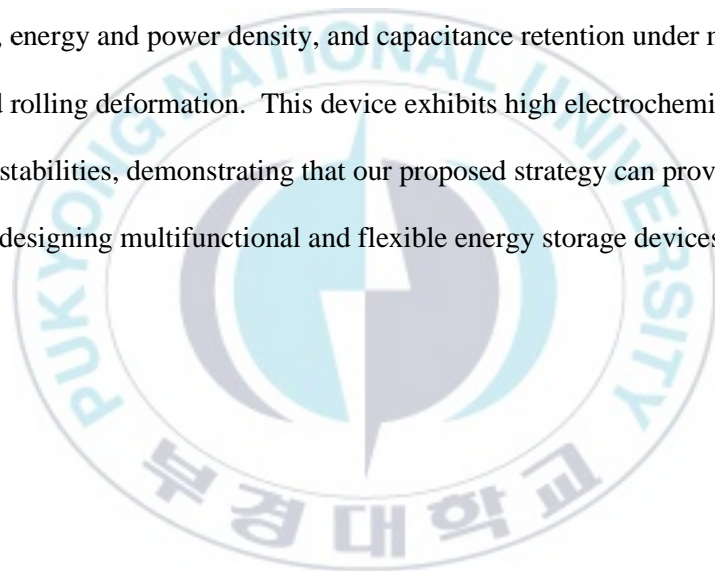
In order to overcome the characteristic trade-off between microscopic ion transport and macroscopic mechanical support, inducing microphase separated morphologies in nanostructured polymeric electrolyte materials has been immensely studied.^{21,22} The microphase separation enables the formation of a nanoscale network morphology, where a conducting phase as the channel for fast ion diffusion can be bicontinuously interlaced with the other insulating phase as the framework for mechanical strength,^{23,24} by the thermodynamic competition between the component volume fractions and the relative interactions of the two phases. Recently, Oh and co-workers developed an ionic liquid-containing poly(ethylene oxide)-*b*-poly(styrene-*co*-divinylbenzene) [PEO-*b*-P(S-*co*-DVB)]-based SPE having the advantages of mechanical (elastic modulus ~ 10 MPa at 298 K) and ion-conducting ($\sigma_{DC} \sim 10^{-4}$ S/cm at 298 K) properties, via reversible addition-fragmentation chain transfer polymerization.²⁵ The polymerization gives rise to polymerization-induced microphase separation (PIMS) within the block copolymer-based SPE. This PIMS method has been also used to prepare other block copolymer-based SPEs with high mechanical and electrical performances.^{24,26} In addition to the PEO-*b*-PS block copolymer electrolytes, synthesized by relatively complex radical initiation

polymerization processes, the epoxy-based SPEs (called structural electrolytes), prepared from a simple cross-linking reaction, have been explored for the development of structural batteries or supercapacitors, carrying mechanical loadings and energy storage function in next-generation electric vehicles that require significant weight savings.^{27,28,37,38,29–36} Shirshova et al. reported ionic liquid/epoxy resin-based structural electrolytes, where the combination of 70 wt% of conducting ionic liquid and 30 wt% of structural epoxy resin led to a multifunctional electrolyte with a room temperature ionic conductivity of 8×10^{-4} S/cm and Young's modulus of 0.2 GPa, attributed to a spinodal microstructure.²⁷ Pint and co-workers demonstrated the fabrication of structural supercapacitors based on the bisphenol A epoxy resin/ionic liquid electrolytes, but their electrolytes still showed the trade-off between Young's modulus (from 100 to 0.1 MPa) and ionic conductivity (from 10^{-7} to 10^{-4} S/cm).²⁹ Johansson and co-workers reported another epoxy-based electrolyte containing a lithium salt mixture with two organic solvents of dimethyl methylphosphonate and ethylene carbonate for structural lithium-ion batteries, and the electrolyte showed an ionic conductivity of 1.5×10^{-4} S/cm and a storage modulus of 750 MPa, prepared by either thermal or UV curing process, but its electrochemical and mechanical stabilities have not been tested yet.^{30,36} Previously, we also reported the multifunctional lithium salt-containing epoxy-based SPEs combined with either plastic crystals, Al_2O_3 nanowires, or ionic liquids, and their morphology, ion conduction, dielectric, and viscoelastic responses were thoroughly investigated using various experimental measurements and theoretical calculations.^{31–34,39} The Al_2O_3

incorporation allowed for the simultaneous increase in ionic conductivity (σ_{DC}) and Young's modulus (E) of the nanocomposite SPEs, thus achieving $\sigma_{DC} \sim 3 \times 10^{-4}$ S/cm and $E \sim 1$ GPa. Although these epoxy-based SPEs can be one of the solutions to concurrently achieve the conflicting physical properties, these SPEs cannot be used as flexible or bendable energy storage systems owing to their brittle characteristics without significant elastic deformation; i.e., elongation at break < 20 %.[34] Therefore, to install an additional third feature in the SPE, it is important to understand how to induce and customize the SPE multifunction.

Here, we prepared epoxy-based flexible, conductive, and sturdy network SPEs, where a cross-linkable robust epoxy resin (diglycidyl ether of bisphenol-A, referred to as DEBA) was combined with lithium solvating oligoethers (tetraethylene glycol dimethyl ether, TG), weak-binding lithium salts [lithium bis(trifluoromethanesulfonyl)imide salt, LiTf₂N], and high-conductivity ionic liquids [1-butyl-3-methylimidazolium bis(trifluoromethylsulfonyl)imide, BMIM-Tf₂N = BT], via a facile one-pot epoxy ring-opening polymerization, resulting in an integration of high ionic conductivity, modulus, and elongation at break by PIMS, for the development of all-solid-state flexible supercapacitors. To understand and tune these multifunctional physical properties of the eligible SPEs, the effects of electrolyte type and concentration on morphologic, dielectric, and mechanical properties were thoroughly explored by microstructural, dielectric relaxation, and mechanical measurements. We find that the lithium salt (LiTf₂N) concentration within the

electrolyte mixture plays a vital role in the formation of a bicontinuous nanoscale ion channel confined in the epoxy matrix (Figure 2-1). This allows us to thermodynamically control the size of ionic and epoxy domains in order to increase the microscopic ion diffusion rate as well as the macroscopic flexibility of the SPEs. Furthermore, an all-solid-state bendable and rollable supercapacitor based on the flexible epoxy-based SPE and symmetric activated carbon (AC) electrodes was fabricated, and its electrochemical performance was explored by measuring specific capacitance, energy and power density, and capacitance retention under mechanical bending and rolling deformation. This device exhibits high electrochemical and mechanical stabilities, demonstrating that our proposed strategy can provide useful insights for designing multifunctional and flexible energy storage devices.



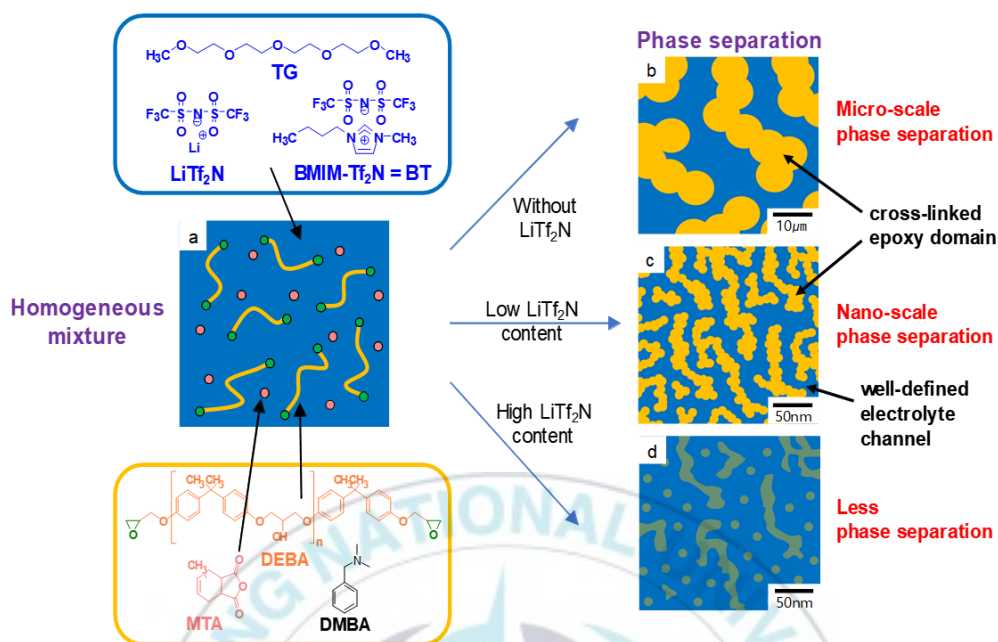


Figure 2-1 Schematic description of bicontinuous network morphology generation by PIMS. (a) A homogeneous mixture containing electrolyte (blue) components (TG, LiTf₂N, and BT) and epoxy (yellow) components [DEBA, methyl tetrahydrophthalic anhydride (MTA) curing agent, and N,N-dimethylbenzylamine (DMBA) catalyst] and showing chemical structures of each component. (b, c, and d) Varying LiTf₂N salt content tunes phase-separated morphology: (b) micro-scale phase separation, (c) nano-scale phase separation, and (d) less phase separation.

II-2. Experimental Section

II-2.1 Materials

Lithium bis(trifluoromethanesulfonyl)imide salt (LiTf_2N) was purchased from Sigma Aldrich and dried in a vacuum oven at 120 °C before use. Purified tetraethylene glycol dimethyl ether (TG), 1-butyl-3-methylimidazolium bis(trifluoromethylsulfonyl)imide ($\text{BMIM-Tf}_2\text{N} = \text{BT}$), *N,N*-dimethylbenzylamine (DMBA), poly(vinylidene fluoride-*co*-hexafluoropropylene) (PVDF-HFP), and 1-methyl-2-pyrrolidinone (NMP) were purchased from Sigma Aldrich and used as received. Methyl tetrahydrophthalic anhydride (MTA) and diglycidyl ether of bisphenol-A (DEBA) from Kukdo Chemical were used as received. Active carbon (AC with a surface area of 2000 m^2/g) and conductive carbon (CC with a surface area of 62 m^2/g) powders were purchased from MTI.

II-2.2 Synthesis of epoxy-based solid polymer electrolyte

Different molarity of Li salt was completely dissolved in TG and BT solution. The solvating ionic liquids was mixed with epoxy components which were composed of DEBA, MTA, and BDMA in the ratio of 100:90:1.5. After degassing under vacuum for 30 min, the blends (termed X M_Y%, where X and Y are LiTf₂N molarity (X = 0, 0.5, 1, 1.5, 2 and 4.5) and electrolyte weight fraction (Y = 30, 50 and 70), respectively) were cured at elevated temperatures from 120 to 180 °C with 1 °C/min heating rate for 2 h in an oven.



II-2.3 Fabrication of epoxy-based supercapacitor

For electrodes of our SPE-based supercapacitor, carbon slurries were prepared by dissolving AC active material, CC conductive additive, and PVDF-HFP binder in NMP (with the mass ratio of AC:CC:PVDF-HFP = 80:17:3). The mixtures were stirred until their homogeneous slurries were formed. The prepared carbon slurries were coated onto a nickel foam current collector using a film applicator. These AC-based electrodes were dried at 120 °C in a vacuum oven for 12 h to remove the NMP solvent remained in the carbon materials. All-solid-state supercapacitor was then fabricated by sandwiching an epoxy-based SPE (1 M_70%) between the two AC electrodes. Finally, the assembled supercapacitor was sealed by aluminum-laminated films to make a supercapacitor pouch cell.

II-2.4 Characterization

Thermal stabilities of these SPEs were investigated by thermogravimetric analysis (TGA) thermograms using a Perkin Elmer TGA-7 instrument Pyris-1 with a heating rate of 10 K/min from 30 to 900 °C under N₂. TGA 5% weight loss was 311 °C. Glass transition temperature (T_g) measurements were conducted using a TA Instrument Q2000 differential scanning calorimeter (DSC) with 10 K/min heating and cooling rates under an inert atmosphere. Sample weights were maintained approximately 7-10 mg and sealed in an aluminum pan. The T_g was taken as the inflection point in the DSC thermogram from the second heating scan using TA Instruments Universal Analysis software.

FE-SEM images were recorded on JSM-6700F (JEOL), with an accelerating voltage of 15.0 kV, after Pt sputter coating for 30 min. To clearly observe SPE morphology, prior to FE-SEM analysis, each sample was placed in ethanol for 3 days, allowing to extract electrolyte components from SPE, and then dried in a vacuum oven for overnight at room temperature to perfectly remove the ethanol.

The stress-strain curves at room temperature were measured using a Q800 dynamic mechanical analyzer (TA Instrument). Samples were cut into rectangular films with dimensions of approximately 20 (length) x 2 (width) x 1.5 (thickness) mm. All tensile tests were conducted using a film tension clamp with a stress ramp rate of 1 N/min, and each sample was tested at least five times to verify the data.

The ionic conductivity and complex permittivity measurements were conducted by Novocontrol GmbH Concept 40 broadband dielectric relaxation spectrometer using a sinusoidal voltage with amplitude 0.1 V. Samples were prepared by sandwiching SPE with ~1.5 mm thickness between two polished brass electrodes having two different diameters [such as 10 mm (top electrode) and 20 mm (bottom electrode)]. The prepared samples were placed in the Quatro Cryosystem sample chamber and then annealed at 120 °C for 1 h prior to the measurements to remove any residual water. Data were collected in isothermal frequency sweeps from $10^7 - 10^{-1}$ Hz in the temperature range from 120 to -50 °C.

FTIR spectra were investigated using a Perkin Elmer Spectrum X, equipped with a diamond attenuated total reflection cell, at room temperature.

The electrochemical characteristics of the assembled AC/SPE/AC supercapacitor were investigated by cyclic voltammetry (CV) and galvanostatic charge-discharge (GCD) experiments using VSP 300 from Bio-Logic Science Instruments. The CV tests were conducted in a potential range from 0 to 3 V with a scan rate of 10, 20, 30, 50, and 100 mV/s. The GCD performance was explored at various current densities from 0.16 to 1.8 A/g with the same potential range as the CV tests.

II-3. Result and Discussion

II-3.1 Thermal Analysis

Figure 2-2 shows glass transition temperature (T_g) that was only observed in these epoxy-based SPEs containing an electrolyte mixture of LiTf_2N , TG, and BT ($\text{LiTf}_2\text{N} + \text{TG} + \text{BT}$) by DSC. The neat epoxy matrix without the electrolyte components (0%) has a single $T_g = 407 \text{ K}^{34}$ (indicated by a horizontal dotted line in Figure 2-2b), and the single T_g is also observed in the SPE with less than 50 wt% electrolyte (2 M_30% with $T_g = 276 \text{ K}$). Incorporating 50 or 70 wt% electrolyte into the epoxy resin, however, creates the SPEs with two T_g s as shown in Figure 2-2b, where 70 wt% electrolyte containing SPEs with various LiTf_2N mol concentrations (0, 0.5, 1, 1.5, and 2 M_70%) have two different T_g s, indicating the occurrence of microphase separation into epoxy- and electrolyte-rich domains. In each SPE, the higher T_g is for the epoxy-rich microphase (T_g^{epo} , open symbols), whereas the lower T_g is for the electrolyte-rich microphase (T_g^{ele} , filled symbols), consistent with previous work³⁴ and the following microstructural investigation by FE-SEM, discussed in a later section. The T_g^{epo} values are $\sim 160 \text{ K}$ higher than the T_g^{ele} values, which are in the range of 187 K (= T_g of BT) to 219 K (= T_g of a mixture of TG and LiTf_2N).

To further understand the two T_g s observed in these SPEs, the prediction from the Fox equation (Eq. 2-1, dashed curve in Figure 2-2c) and Gordon-Taylor equation (Eq. 2-2, solid curves in Figure 2-2c) was compared to the composition dependence of DSC glass transition temperature.

$$\frac{1}{T_g^{\text{SPE}}} = \frac{1-\Phi_{\text{BT}}}{T_g^{\text{Pure Epoxy}}} + \frac{\Phi_{\text{BT}}}{T_g^{\text{BT}}} \quad (2-1)$$

$$T_g^{\text{epo}}(\text{or } T_g^{\text{ele}}) = \frac{(1-\Phi_{\text{BT}})T_g^{\text{Pure Epoxy}} + K\Phi_{\text{BT}}T_g^{\text{BT}}}{(1-\Phi_{\text{BT}}) + K\Phi_{\text{BT}}} \quad (2-2)$$

where T_g^{SPE} is the epoxy-based SPE T_g , Φ_{BT} is the weight fraction of BMIM-Tf₂N (BT), K is a fitting parameter connected to the degree of curvature of T_g vs Φ_{BT} curve, $T_g^{\text{Pure Epoxy}} = 407$, and $T_g^{\text{BT}} = 187$ K. The simple two component Fox prediction does not describe the T_g characteristic of the microphase separated SPE with two resolvable T_g s; i.e., the measured T_g^{epo} (open symbols) and T_g^{ele} (filled symbols) are consistently above and below the Fox prediction (dashed curve), respectively. On the contrary, the Gordon-Taylor equation reasonably describes the T_g -composition (Φ_{BT}) dependence of the SPEs with $K^{\text{epo}} = 15$ for T_g^{ele} (black solid curve) and $K^{\text{ele}} = 0.22$ for T_g^{epo} (red solid curve), reflecting the presence of favorable intermolecular interaction between the epoxy and electrolyte components. The observation of $K^{\text{epo}} > K^{\text{ele}}$ presumably indicates that the interaction strength within the epoxy-rich microphase is relatively higher than that within the electrolyte-rich microphase.

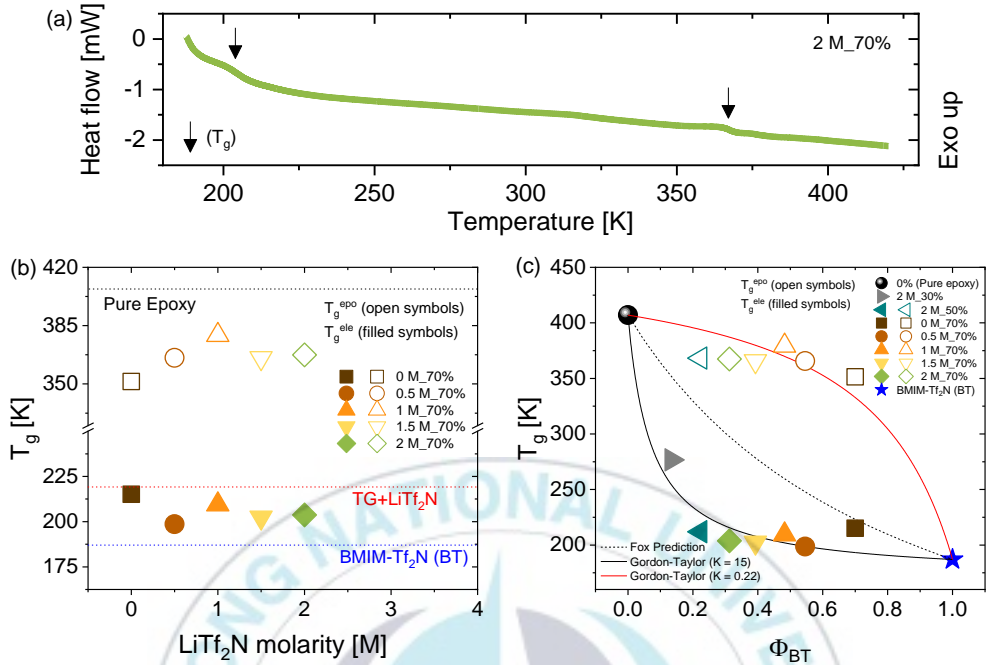


Figure 2-2. (a) Representative DSC thermogram of 2 M_{70%} with its T_gs, indicated by the arrows. Compositional variation of (b) the LiTf₂N molarity and of (c) the weight fraction of BT (Φ_{BT}) in the glass transition temperature T_g for epoxy-based SPEs, where two T_g values are observed: T_g of epoxy-rich domain (T_g^{epo}, open symbols) and T_g of electrolyte-rich domain (T_g^{ele}, filled symbols). The horizontal dotted lines indicate T_g of pure epoxy (0%, black color), a mixture of TG and LiTf₂N (red color), and BT (blue color). The dashed and solid curves represent Fox prediction (Eq 2-1) and Gordon-Taylor equation fits (Eq 2-2 with K = 15 for T_g^{ele} and K = 0.22 for T_g^{epo}), respectively.

II-3.2 Morphology

To confirm the microphase separation in the epoxy-based SPEs, their microstructural investigation was performed using FE-SEM analysis (Figure 2-3). For the epoxy-based SPEs, the fully miscible homogeneous mixture of epoxy resin (DEBA), curing agent (MTA), and electrolyte components (TG, BT, and LiTf₂N) is initially prepared, and then the mixture solution can be converted to two separated microphases during the curing process via PIMS. For the SPE without LiTf₂N (0 M_70%), its FE-SEM image (Figure 2-3a) shows spherical epoxy nodules with a diameter of ~3 μ m that are connected with each other, allowing to create a micro-scale porous network structure. Such a morphology has been also observed in other epoxy-based SPEs.^{28,40} The addition of 0.5 M LiTf₂N to the SPE (0.5 M_70%) significantly reduces the nodule size to ~50 nm by sixty times, and the nano-size nodules are well connected to each other (Figure 2-3b). This produces a finely microphase-separated bicontinuous network morphology, where an ionic conducting electrolyte-rich phase is effectively arranged along the continuous nanoporous channel (dark regions in Figure 2-3b) separated from the epoxy-rich phase (bright regions in Figure 2-3b).

Further increasing LiTf₂N molarity to 1, 1.5, 2, and 4.5 M LiTf₂N likely leads to multiple connections between the epoxy nodules, i.e., nodule coarsening (Figure 2-3c). This results in the formation of the continuous epoxy matrix, where discrete pores of the electrolyte domains are randomly dispersed (Figures 2-3d and 2-3e). The isolated pores seem to become smaller as further increasing LiTf₂N content, indicating that the

microphase separation becomes less pronounced at higher LiTf₂N content. For the SPE with the maximum LiTf₂N molarity (4.5 M_70%), eventually no pores are observed at a sub-micron scale (Figure 2-3f), presumably indicating that the electrolytes uniformly exist in the epoxy matrix without a well-defined microphase separation. This is presumably why 4.5 M_70% with the highest LiTf₂N content does not exhibit two T_gs unlike the other lower LiTf₂N containing SPEs (Figure 2-2).

Such a significant dependence of the LiTf₂N molarity on the epoxy-based SPE morphology can be explained by the change in an intermolecular interaction between epoxy and electrolyte components during PIMS. The mean-field theory^{41,42} allows us to understand the change in the binary mixing free energy ΔF_{mix} of a polymer solution, assuming that for our epoxy-based SPE, the epoxy-derived species (DEBA and MTA) and electrolyte species (TG, BT, and LiTf₂N) are the component 1 and 2 of the binary polymer solution, respectively, during PIMS via a ring-opening polymerization:

$$\Delta F_{\text{mix}} \sim kT \left(\frac{\phi_1}{N_1} \ln \phi_1 + \frac{\phi_2}{N_2} \ln \phi_2 + \chi \phi_1 \phi_2 \right) \quad (2-3)$$

where $0 \leq \phi \leq 1$ and N are the volume fraction and degree of polymerization of each component, respectively, and χ is the interaction parameter (or solubility parameter difference) between the components. Throughout the polymerization reaction, the second entropy term $\phi_2 \ln \phi_2 / N_2$ of the electrolyte species remains constant because of the constant of both ϕ_2 and $N_2 = 1$, whereas the first entropy term

$\phi_1 \ln \phi_1 / N_1$ increases (or becoming less negative with $N_1 > 1$) and the third enthalpy term $\chi \phi_1 \phi_2$ also increases with decreasing miscibility of the components. The ΔF_{mix} being positive results in phase separation into two phases, suggesting that N_1 and χ are the main factors to control morphology (micro-scale pore vs nano-scale pore) of these epoxy-based SPEs. On the base of the previous FTIR and rheological measurements as well as density functional theory studies,^{31,39} demonstrating a favorable intermolecular ion-dipole interaction between LiTf₂N (Li⁺ cation) and MTA [ether oxygen in cyclic anhydride (C-O-C) group], it is expected that the solubility difference (or interaction parameter) changes with LiTf₂N molarity. During the cross-linking reaction, the epoxy species become insoluble in the electrolyte species due to the increase in solubility difference by opening anhydride bond for constituting cross-linking (i.e., esterification reaction) between MTA and the epoxide groups of DEBA.⁴³ In the absence of LiTf₂N, the phase separation presumably occurs at the beginning of the reaction because the increase in the free energy of mixing is high enough, thereby creating micro-scale porous morphology (Figure 2-3a). On the other hand, the LiTf₂N presence, improving the solubility of DEBA in the electrolyte (relatively lower χ), seems to delay the microphase separation,²⁸ providing the well-defined bicontinuous nano-scale porous morphology (Figure 2-3b). Further increasing LiTf₂N content, however, considerably reduces the driving force for the PIMS by the decrease in both the solubility difference and the cross-linking length (lowering χ and N_1 ,

respectively), leading to the formation of single-phase or nonporous morphology (Figure 2-3f).



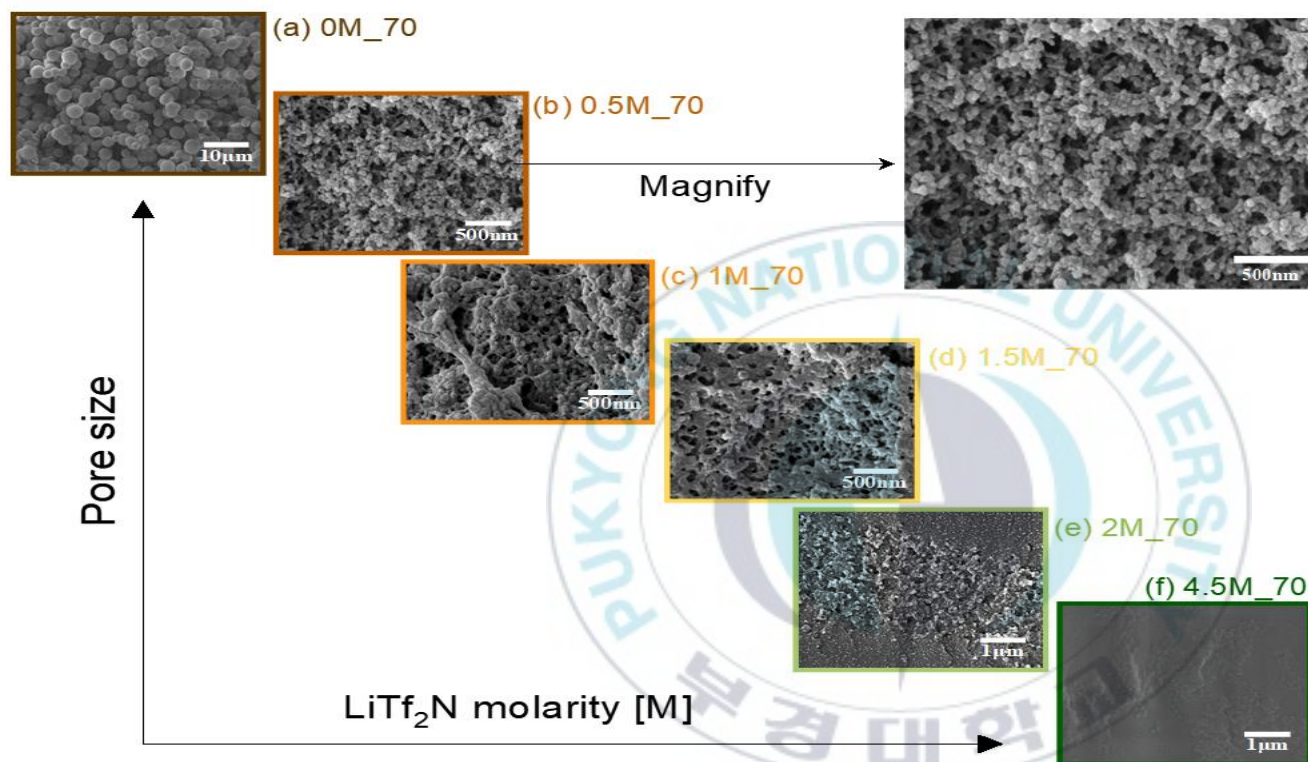


Figure 2-3. FE-SEM micrographs of (a) 0 M₇₀%, (b) 0.5 M₇₀%, (c) 1 M₇₀%, (d) 1.5 M₇₀%, (e) 2 M₇₀%, and (f) 4.5 M₇₀%, showing that the extraction of electrolyte components from SPE produces percolating pores (black regions) in a cross-linked epoxy matrix (bright regions), and the pore size decreases with increasing LiTf₂N molarity.

II-3.3 Ionic conductivity

Figure 2-6a displays the temperature dependence of DC ionic conductivity $\sigma_{DC}(T)$, obtained from the angular frequency ω dependence of in-phase conductivity $\sigma'(\omega)$ (Figure 2-4), for these epoxy-based SPEs with various LiTf_2N molarities. Their $\sigma_{DC}(T)$ temperature dependence is well described by a Vogel-Tammann-Fulcher (VTF) equation^{34,44}

$$\sigma_{DC}(T) = \frac{A}{T^{1/2}} \exp \left[-\frac{E_a}{R(T-T_0)} \right] \quad (2-4)$$

The solid curves in Figure 2-6a are fits to equation 2-4 with three fitting parameters T_0 , E_a , and A , listed in Table 2-1, indicating the Vogel temperature, the activation energy for ion conduction, and the pre-exponential constant at infinite temperature (proportional to the number of charge carries), respectively. For the SPEs containing LiTf_2N , increasing the LiTf_2N molarity leads to a continuous decrease in the ionic conductivity, so that 0.5 M_70% with the lowest LiTf_2N molarity ($\sigma_{DC} \sim 1.1 \times 10^{-3}$ S/cm) exhibits ~30 times higher room temperature σ_{DC} than 4.5 M_70% with the highest LiTf_2N molarity ($\sigma_{DC} \sim 4.3 \times 10^{-5}$ S/cm). Such an effect of LiTf_2N content on the conductivity is more clearly observed in the inset of Figure 2-6a, showing σ_{DC} vs T_0/T , where the Vogel temperatures T_0 of these SPEs show a typical correlation with the glass transition temperature (i.e., $T_g^{\text{ele}} - T_0 \sim 42$ K, listed in Table 2-1).⁴⁴ With the excluded plasticization (T_0) effect from $\sigma_{DC}(T)$, the

conductivity data were not merged into a single curve, but 0.5 M_70% showed the highest $\sigma_{DC}(T_0/T)$ among the SPEs studied.

To further understand the influence of LiTf₂N on the ionic conductivity of these SPEs, Figure 2-6b compares the room temperature ionic conductivities of the SPEs containing 70% electrolyte (σ_{DC}^{SPE} , filled symbols) with those of their corresponding pure electrolytes without the epoxy component (σ_{DC}^{ele} , open symbols). For σ_{DC}^{ele} , the neat electrolyte without LiTf₂N (0 M_100%, open square symbol) has the highest room temperature ionic conductivity (6×10^{-3} S/cm), and the LiTf₂N incorporation (0.5, 1, 1.5, 2, and 4 M_100%) leads to a monotonic decrease in σ_{DC}^{ele} (approaching to 2×10^{-3} S/cm) with increasing LiTf₂N content. On the other hand, after the thermal cross-linking a mixture of the neat electrolyte and epoxy resin, the SPE room temperature ionic conductivity (σ_{DC}^{SPE}) is lower than its corresponding neat electrolyte (σ_{DC}^{ele}), as expected. Unlike the neat electrolyte, the highest ionic conductivity among the SPEs was observed in the SPE with 0.5 M LiTf₂N, whose $\sigma_{DC}^{SPE} \sim 1 \times 10^{-3}$ S/cm is more than three times the conductivity of the SPE with no LiTf₂N ($\sigma_{DC}^{SPE} \sim 3 \times 10^{-4}$ S/cm). The superior conductivity in 0.5 M_70% with the nano-scale porous morphology (shown in Figure 2-3 b) rather than 0 M_70% with the micro-scale porous morphology (Figure 2-3 a) can be explained by the activation energy for the conduction (E_a , X symbols in Figure 2-6 b). The addition of 0.5 M LiTf₂N leads to a decrease in E_a from 8.4 (0 M_70%) to 6.2 kJ/mol (0.5 M_70%), where ions in the nanoporous channel seems to be fast diffused with the lower activation energy than

those in the microporous channel with the higher activation energy. This nanochannel diffusing ion state has lower activation energy ($E_a \sim 6.2$ kJ/mol) than the other epoxy-based SPEs containing either a LiTf₂N mixture with ionic liquid ($E_a \sim 8.4$ kJ/mol)³⁴ or succinonitrile ($E_a \sim 32$ kJ/mol).³¹ Then, further increasing LiTf₂N molarity continuously increases E_a to 12 kJ/mol of 4.5 M_70% that has the lowest ionic conductivity among the SPEs studied. This is exactly the same tendency of the room temperature ionic conductivity of the SPEs; the lower E_a , the higher σ_{DC}^{SPE} , as shown in Figure 2-6b. The same activation energy dependence of ionic conductivity is also observed in these SPEs with different electrolyte contents or types (Figure 2-5).

For the pre-exponential constant A (filled symbols in Figure 2-6c) revealing the number of charge carriers that participate in the ionic conductivity, the incorporation of LiTf₂N into the SPE initially increases A with LiTf₂N molarity, up to 1.5 M LiTf₂N, indicating that the more ions participate in the ion conduction through the well-defined bicontinuous morphology as observed in the FE-SEM (Figures 2-3a-d), while the addition of more than 2 M LiTf₂N leads to a decrease in A , indicating that all the ions cannot take part in the ionic conductivity, consistent with the less-pronounced microphase separated structure by the FE-SEM measurement (Figures 2-3e-f). A similar result can be also noticed in the FTIR spectra ($\Delta\omega$, open symbols in Figure 2-6c) for various LiTf₂N compositions of the epoxy-based SPEs. The peak at $\omega_{BT} \sim 1050$ cm⁻¹ corresponding to the vibration of the SNS of Tf₂N anion of BT

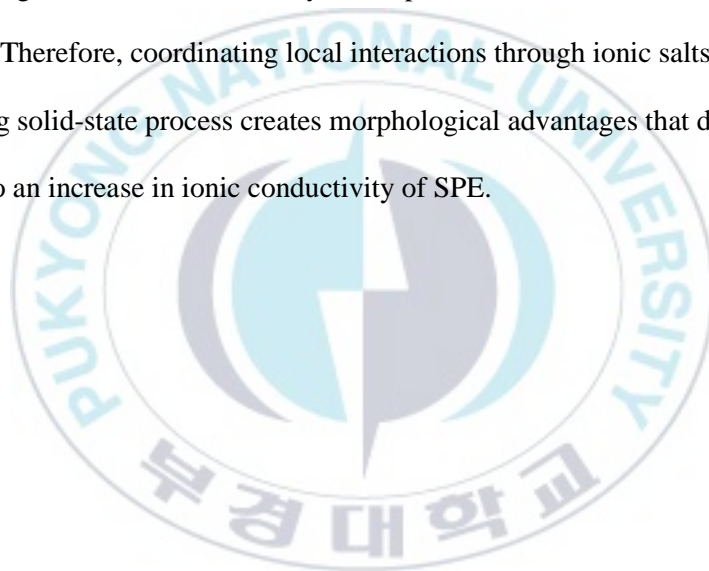
shows systematic movements to either lower or higher wavenumber with changing LiTf₂N molarity (Figure 2-7).⁴⁵ Figure 2-6c exhibits the wavenumber difference $\Delta\omega = \omega_{\text{BT}} - \omega_{\text{SPE}}$ (open symbols) of the SNS peak between the pure ionic liquid BT and the SPE as a function of LiTf₂N content. Like the pre-exponential constant A, upon the addition of LiTf₂N from 0 to 1.5 M, the characteristic SNS band difference $\Delta\omega$ systematically increases, whereas further increasing LiTf₂N molarity (2 M and 4.5 M) leads to a decrease in $\Delta\omega$. This presumably indicates that the LiTf₂N addition provides various complex formations between BT, LiTf₂N, and TG, owing to ion-dipole interaction between TG and either BMIM⁺ in BT or Li⁺ in LiTf₂N, enabling to change the number density of free Tf₂N⁻, BMIM⁺, or Li⁺ in the SPE, which is directly correlated to the concentration of charge carrier contributing to the ionic conductivity.^{46,47}

To confirm the morphology advantage on the ionic conductivity of these SPEs, each SPE room temperature conductivity ($\sigma_{\text{DC}}^{\text{SPE}}$, filled symbols in Figure 2-6b) was divided by the corresponding neat electrolyte conductivity ($\sigma_{\text{DC}}^{\text{ele}}$, open symbols in Figure 2-6b) and its volume fraction ($\Phi_{\text{ele}} = 0.7$), introducing the effective conductivity σ_{eff} (Figure 2-6d),^{31,34,48}

$$\sigma_{\text{eff}} = \frac{\sigma_{\text{DC}}^{\text{SPE}}}{\sigma_{\text{DC}}^{\text{ele}} \Phi_{\text{ele}}} = \frac{1}{\tau} \quad (2-5)$$

with assuming that ion transport across the SPE conducting phase is identical to that of the intrinsic neat electrolyte. The σ_{eff} is also inversely related to the tortuosity τ ,

telling us the conducting network topology (inset of Figure 2-6d). The LiTf₂N incorporation substantially raises σ_{eff} from 0.08 (0 M_70%) to 0.37 (0.5 M_70%), so that the tortuosity decreases by 5 times from $\tau \sim 12$ (0 M_70%) to $\tau \sim 2.7$ (0.5 M_70%) (see inset of Figure 2-6d). The fact that 0.5 M LiTf₂N shows the lowest τ , whose value is within the predicting scope of the reported bicontinuous network structure ($1.5 \leq \tau \leq 3$),^{26,29,49} suggests an ionic nano-channel being effectively arranged along the continuous electrolyte-rich phase intertwined with the epoxy-rich framework. Therefore, coordinating local interactions through ionic salts during a cross-linking solid-state process creates morphological advantages that directly contribute to an increase in ionic conductivity of SPE.



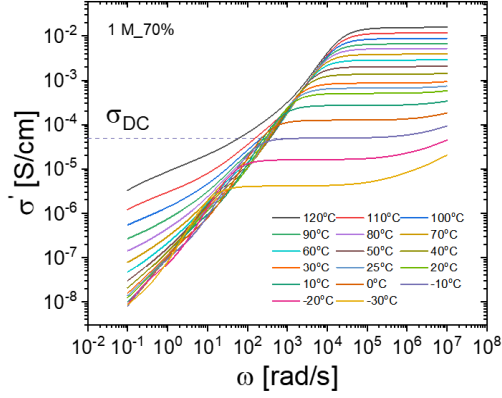


Figure 2-4. Angular frequency dependence of in-phase conductivity $\sigma'(\omega)$ at various temperatures from 120 to -30 °C. The horizontal dashed line indicates the DC ionic conductivity σ_{DC} .

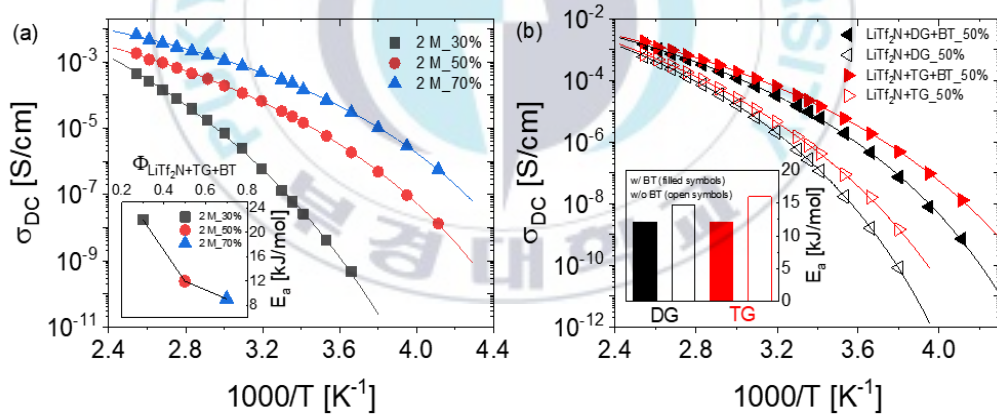


Figure 2-5 Temperature dependence of ionic conductivity for (a) epoxy-based SPEs with different electrolyte contents ($\Phi_{\text{LiTF}_2\text{N}+\text{TG}+\text{BT}} = 30, 50$ or 70 wt%) and for (b) epoxy-based SPEs with and without BT: the solid curves are the VTF equation fits (Eq 2-4). The insets in (a) and (b) show activation energies E_a s for ion conduction.

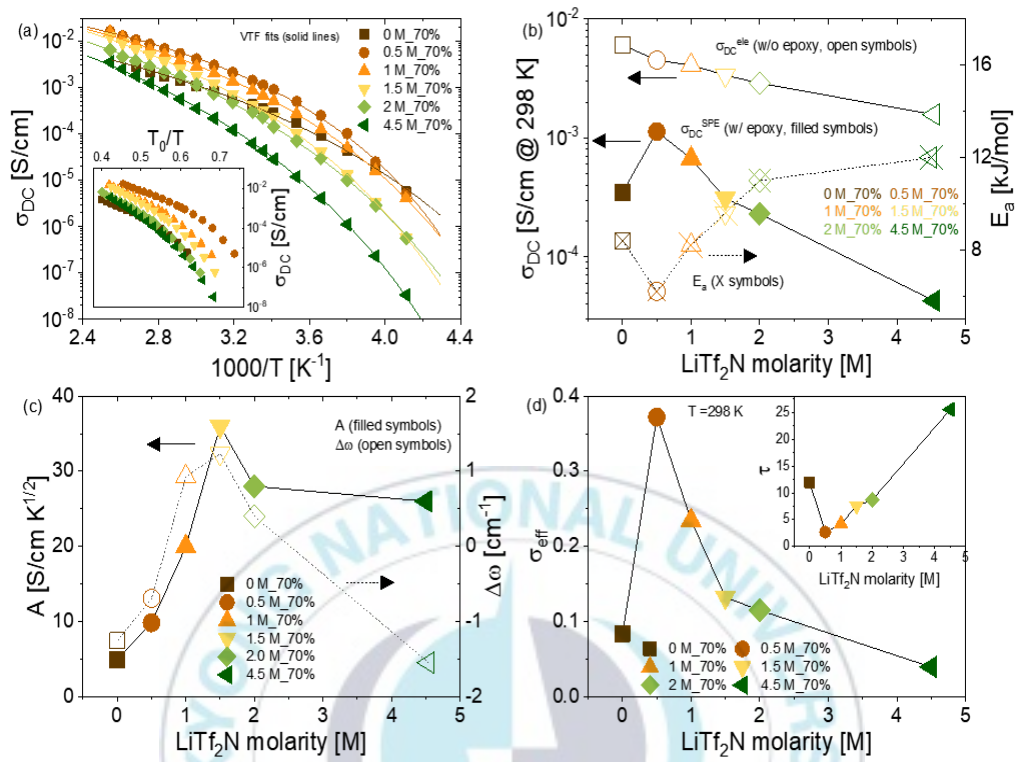


Figure 2-6. (a) Temperature dependence of ionic conductivity for epoxy-based SPEs with various LiTf_2N molarities (σ_{DC} vs T_0/T in the inset): the solid curves are VTF (Eq 2-4) fits to data. LiTf_2N molarity variation in (b) room temperature ionic conductivity of SPEs ($\sigma_{\text{DC}}^{\text{SPE}}$, filled symbols, left axis) and their corresponding pure electrolytes ($\sigma_{\text{DC}}^{\text{ele}}$, open symbols, left axis) and activation energy (E_a , X symbols, right axis), in (c) pre-exponential constant (A , filled symbols, left axis) and wavenumber difference ($\Delta\omega$, open symbols, right axis), and in (d) effective conductivity (σ_{eff}) and tortuosity (τ , in the inset): the solid and dashed lines are only guides for the eyes.

Table 2-1. Fitting Parameters of the VTF Equation for DC Conductivity, Eq 2-4.

Sample	A (S/cm K ^{1/2})	E _a (kJ/mol)	T ₀ (K)	T _g -T ₀ (K)
0 M_70%	4.9	8.4	150	65
0.5 M_70%	9.8	6.2	179	20
1 M_70%	20	8.2	165	44
1.5 M_70%	36	9.6	167	35
2 M_70%	28	11	158	45
4.5 M_70%	26	12	166	41



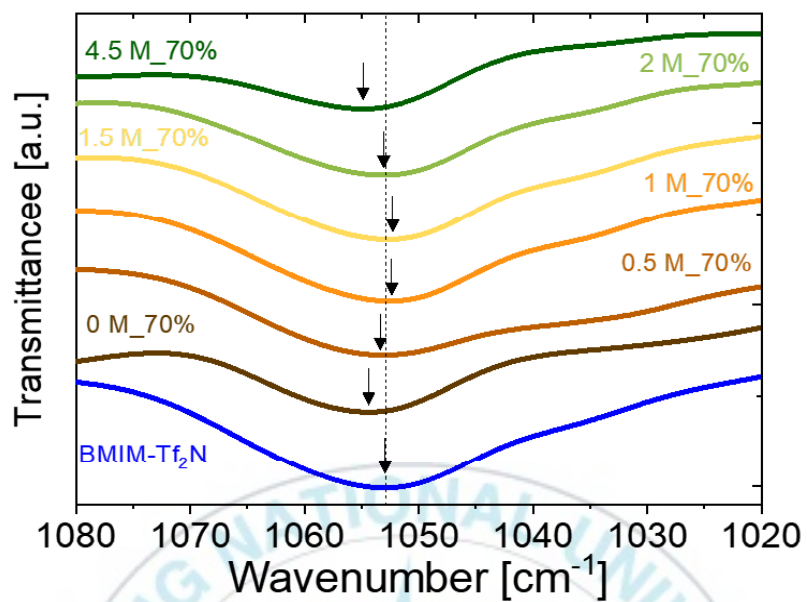


Figure 2-7. ATR-FTIR spectra of BMIM-Tf₂N, 0 M_70%, 0.5 M_70%, 1 M_70%, 1.5 M_70%, 2 M_70%, and 4.5 M_70% in the region from 1080 to 1020 cm^{-1} at room temperature.

II-3.4 Dielectric Relaxation

To further investigate the conductivity difference between 0 M_70% and 0.5 M_70% in terms of micro-scale vs nano-scale ion channel, their dielectric relaxation processes were explored with the dielectric derivative spectra,⁵⁰⁻⁵⁴

$\varepsilon_{\text{der}} = (-\pi/2)\partial\varepsilon'(\omega)/\partial \ln \omega$, as shown in Figure 2-9a. We then fit ε_{der} using the Havriliak-Negami (HN) function⁵⁵ (see solid and dashed lines in Figure 2-9a), and Supporting Information contains the ε_{der} analysis in detail with Figure 2-8.

The dipolar relaxations were explored by fitting the derivative spectra ε_{der} with one power law for electrode polarization (EP) plus two Havriliak-Negami (HN) functions for the two dielectric relaxations (MWS (or α_2) and α)

$$\varepsilon_{\text{der}} = A\omega^{-s} - \frac{\pi}{2} \left(\left[\frac{\partial \varepsilon_{\text{HN}}'(\omega)}{\partial \ln \omega} \right]_{\alpha_2 \text{ (or MWS)}} + \left[\frac{\partial \varepsilon_{\text{HN}}'(\omega)}{\partial \ln \omega} \right]_{\alpha} \right) \text{ with } \varepsilon_{\text{HN}}'(\omega) = \text{Real} \left\{ \frac{\Delta\varepsilon}{[1 + (i\omega/\omega_{\text{HN}})^a]^b} \right\} \quad (2-6)$$

wherein A and s are constants, $\Delta\varepsilon$ is the relaxation strength, a and b are shape parameters and ω_{HN} is a characteristic frequency related to the frequency of maximal loss ω_{max} by⁵⁵

$$\omega_{\text{max}} = \omega_{\text{HN}} \left(\sin \frac{a\pi}{2+2b} \right)^{1/a} \left(\sin \frac{ab\pi}{2+2b} \right)^{-1/a} \quad (2-7)$$

Such fits approximate the data quite well (Figure 2-8) and yield ω_{max} and $\Delta\varepsilon$ for the MWS, α_2 and α processes.

In Figure 2-9a, the SPEs with higher LiTf₂N molarity (1 M_{70%} and 1.5 M_{70%}, also shown in Figures 2-8c and 2-8d, respectively) exhibit two relaxation processes α_2 (ion rearrangement at lower frequency) and α (segmental motion at higher frequency), which are typical dipolar relaxations observed in ion-containing polymers.^{33,53,54} For 0.5 M_{70%}, it also has the two relaxation processes of the α_2 and α (Figures 2-9a and 2-8b), but the reduction of LiTf₂N content to 0.5 M considerably increases the α_2 relaxation strength $\Delta\epsilon_{\alpha_2}$ from $\Delta\epsilon_{\alpha_2} = 41$ for 1.5 M_{70%} and $\Delta\epsilon_{\alpha_2} = 39$ for 1 M_{70%} to $\Delta\epsilon_{\alpha_2} = 210$ for 0.5 M_{70%} (inset of Figure 2-9a). This is consistent with the ~3 times increase in the static dielectric constant (ϵ_s , indicated by solid horizontal lines in Figure 2-9b) upon the reduction of LiTf₂N content from 1.5 M and 1 M to 0.5 M (inset of Figure 2-9b). This presumably indicates that the well-defined bicontinuous nano-scale porous channel (Figure 2-3b) allows ions to easily hop from one state to the other state, thereby enhancing $\Delta\epsilon_{\alpha_2}$ or ϵ_s , while all the ions within the less-pronounced microphase separated structure (Figures 2-3c and 2-3d) may not participate in the ionic orientation polarization (α_2), but instead some of them are trapped in the form of ionic cluster, resulting in a lowering of $\Delta\epsilon_{\alpha_2}$ (Figure 2-9a), ϵ_s (Figure 2-9b), σ_{DC} (Figure 2-6b), and σ_{eff} (Figure 2-6d).

For the SPE without LiTf₂N showing micro-scale porous morphology (Figure 2-3a), however, its ϵ_{der} displays an enormously strong relaxation process, designated as

Maxwell-Wagner-Sillars (MWS),⁵⁵ at lower frequency (Figures 2-9a and 2-8a). The MWS relaxation strength $\Delta\epsilon_{\text{MWS}} = 3817$ (or $\epsilon_s = 3842$) is one or two orders of magnitude higher than those of the SPEs with LiTf₂N (inset of Figures 2-9a and 2-9b). Since the $\Delta\epsilon_{\text{MWS}} > 1000$ is indeed too large to be attributed to a dipolar relaxation, the MWS relaxation observed in the SPE with no LiTf₂N originates from interfacial polarization,^{53,54,56} which is due to mobile charge carrier buildup at the interfacial boundary between the ion domains along the micro-scale channel and the micro-size epoxy nodules; the ionic conducting domain with higher conductivity and permittivity than the epoxy insulating domain, suggesting that 0 M_70% likely has trapped ions at the interface, which cannot take part in the DC conductivity. The same polarization process showed up in the frequency dependence of the in-phase of the conductivity $\sigma'(\omega)$ (filled symbols in Figure 2-9c). For 0.5 M_70%, its σ' starts to be constant at the frequency $\omega_{\alpha_2} \sim 10^6$ rad/s (red vertical dashed line in Figure 2-9c), when the α_2 process is relaxed, and this plateau maintains up to $\sim 10^4$ rad/s, defined as the DC conductivity σ_{DC} (black horizontal solid line in Figure 2-9c). Contrary to the observation of a single plateau in the LiTf₂N-containing SPEs, 0 M_70% exhibits two plateaus. After finishing the first plateau observed at higher frequency, the MWS polarization appears at the frequency $\omega_{\text{MWS}} \sim 2 \times 10^5$ rad/s (green vertical dashed line in Figure 2-9c), indicating diffusing ions being accumulated along the interface between ion and epoxy domains. Consequently, the trapped ions cannot take part in σ_{DC} any

more, but instead the rest of ions still diffuse through micro-scale porous channels, forming the second plateau at lower frequency and resulting in the $\sigma_{DC} \sim 4 \times 10^{-5} \text{ S/cm}$, which is four time lower that the first plateau value. The MWS interfacial polarization has been also observed in the phase-separated polymers, such as DEBA-based epoxy systems,^{57–59} copolymers,^{53,60,61} and ion-containing block copolymers,^{56,62–64} where an abrupt drop in the ionic conductivity occurs.

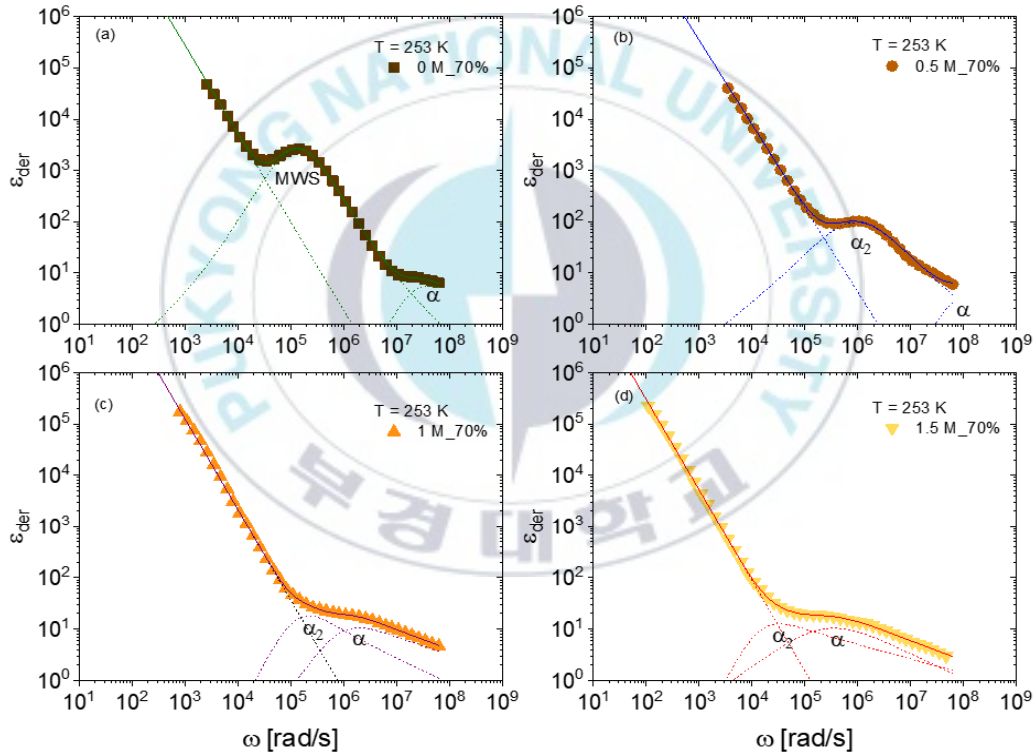


Figure 2-8. Dielectric derivative spectra ε_{der} at 253 K and their fits (solid lines) of the sum of a power law for electrode polarization (EP) and derivative forms of the HN

function for MWS, α_2 , and α processes (dashed lines) for (a) 0 M_70%, (b) 0.5 M_70%, (c) 1 M_70%, and (d) 1.5 M_70%.

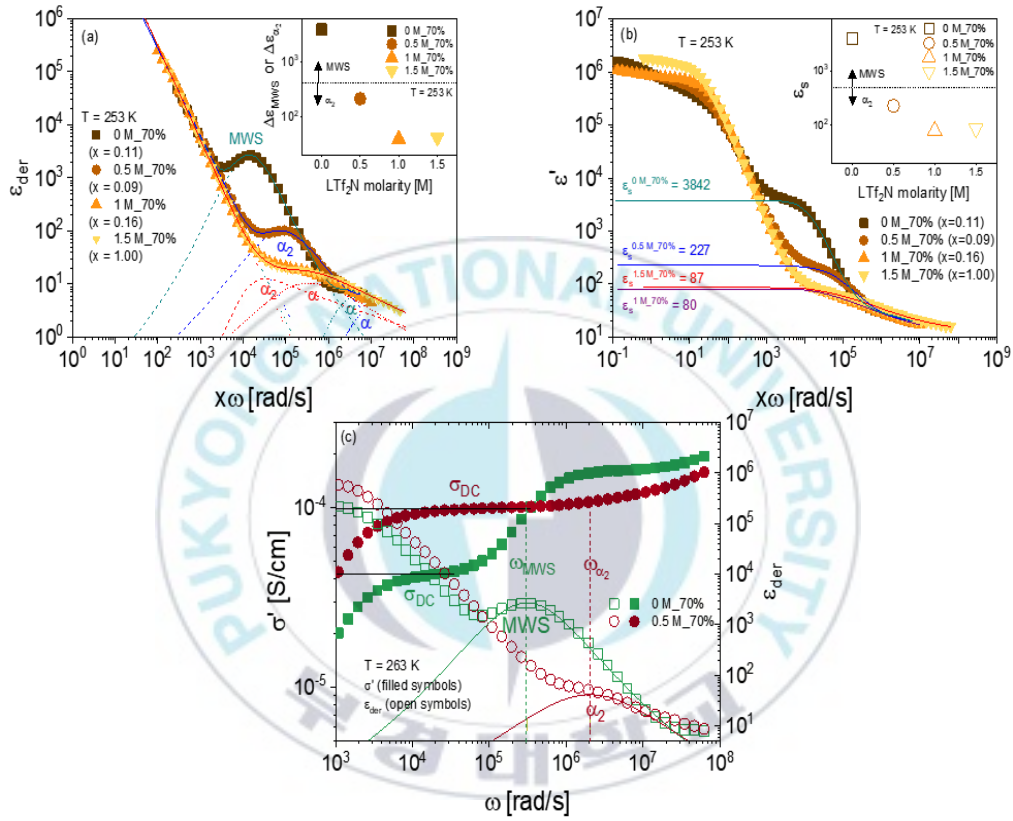


Figure 2-9. (a and b) Angular frequency dependence of (a) dielectric derivative $\varepsilon'_{\text{der}}(x\omega)$ and (b) dielectric permittivity $\varepsilon'(x\omega)$ at 253 K shifted by horizontal shift factor, x [0 M_70% ($x = 0.11$), 0.5 M_70% ($x = 0.09$), 1 M_70% ($x = 0.16$), and 1.5 M_70% ($x = 1.00$)], to superimpose in the region of electrode polarization; solid and dashed curves in (a) are fits of relaxation processes (Figure 2-8) and solid horizontal lines in (b) represent the static dielectric constant ε_s (Figure 2-10). The insets in (a) and (b) show $\Delta\varepsilon$ (filled symbols) and ε_s (open symbols) vs LiTf₂N molarity,

respectively. (c) Angular frequency dependence of in-phase conductivity σ' (left axis, filled symbols) and ε_{der} (right axis, open symbols) for 0 M_70% and 0.5 M_70% at 263 K; solid horizontal lines indicates the DC conductivity σ_{DC} and dashed vertical lines are the relaxation peak frequencies of the MWS and α_2 .

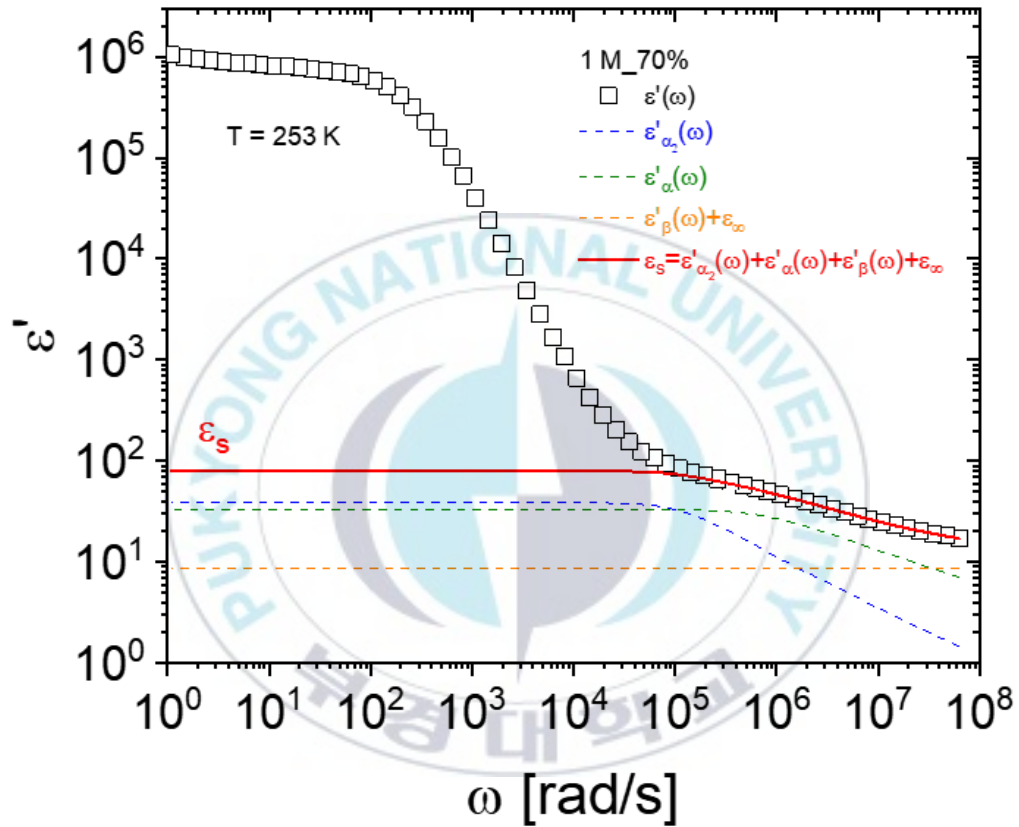


Figure 2-10. Dielectric permittivity $\varepsilon'(\omega)$ of 1 M_70% at 253 K is comprised of frequency-dependent contributions from $\varepsilon'_{\alpha_2}(\omega)$ (blue dashed line), $\varepsilon'_{\alpha_1}(\omega)$ (green dashed line), and $\varepsilon'_{\beta}(\omega) + \varepsilon_{\infty}$ (orange dashed line). The red solid line,

corresponding to the sum of $\varepsilon'_{\alpha_2}(\omega)$, $\varepsilon'_\alpha(\omega)$, and $\varepsilon'_\beta(\omega) + \varepsilon_\infty$, indicates the static dielectric constant $\varepsilon_s = \varepsilon'_{\alpha_2}(\omega) + \varepsilon'_\alpha(\omega) + \varepsilon'_\beta(\omega) + \varepsilon_\infty$.



II-3.5 Mechanical Property

The mechanical properties of Young's modulus and elongation at break were investigated from the stress-strain curves of these epoxy-based SPEs as shown in Figure 2-11 a. Among the SPEs studied, the 0 M_{70%} SPE with no LiTf₂N exhibits the highest tensile strength (5.6 MPa) and Young's modulus (150 MPa) (see Figure 2-11 a and its inset). However, the 0.5 M LiTf₂N incorporation significantly decreases Young's modulus to 1.4 MPa by two orders of magnitude. This can be ascribed to the 60 times decrease in the size of the epoxy nodule from $\sim 3\ \mu\text{m}$ (0 M_{70%}) to $\sim 50\ \text{nm}$ (0.5 M_{70%}), observed from the FE-SEM images (Figure 2-3 a and b). Further increasing LiTf₂N molarity continuously decreases Young's modulus, eventually approaching to $\sim 0.05\ \text{MPa}$ upon the 2 M LiTf₂N addition, as shown in Figure 2-11 b (filled symbols). Contrary to Young's modulus reduction, the elongation at break increases with increasing LiTf₂N content; i.e., the 5 times increase occurs in the elongation at break ($\sim 40\ \%$ for 0 M_{70%} and $\sim 210\ \%$ for 2 M_{70%}, open symbols in Figure 2-11 b). This is also correlated with the morphological observation from the FE-SEM; that is, the LiTf₂N addition leads to the multiple connections between the nano-sized epoxy nodules. Consequently, the nodule coarsening provides the SPE with considerably enhanced flexibility.

To select the best solid polymer electrolyte for flexible supercapacitors, Figure 2-12 a and 2-12 b display the correlations between ionic conductivity and either elongation at break or Young's modulus at room temperature for the SPEs studied

herein (red and blue colored symbols) and reported from literature (green colored symbols).^{29,65,66} For the 50% electrolyte-containing epoxy-based (blue colored symbols in Figure 2-12 a) and previously reported epoxy- or PEO-based (green colored symbols in Figure 2-12 a) SPEs, their room temperature ionic conductivities significantly decrease with increasing the SPE elongation. For the 70% electrolyte containing SPEs (X M_70%, red colored symbols in Figure 2-12 a), however, their break elongation was enhanced from ~50 to ~230%, via changing LiTf₂N molarity (X = 0, 0.5, 1, 1.5 & 2 M), without sacrificing ionic conductivity ($\sigma_{DC} > 10^{-4}$ S/cm). Such an independent tuning of multiple properties was also observed in the plot of ionic conductivity vs Young's modulus for the 70% electrolyte-containing SPEs, whose modulus increases by up to three orders of magnitude while maintaining the conductivity above 10^{-4} S/cm (red colored symbols in Figure 2-12 a). Furthermore, Figure 2-12 c exhibits the three-functional plot of ionic conductivity (left axis) and Young's modulus (right axis) as a function of elongation at break for all the SPEs studied herein (red and blue colored symbols), compared with literature values (green colored symbols). For the use of these SPEs in practical energy storage devices, the following minimum requirements¹⁷ should be simultaneously satisfied; i.e., the lower limit of Young's modulus, elongation at break, and ionic conductivity is 0.1 MPa, 100 %, and 10^{-4} S/cm, respectively, as indicated by orange colored area in Figure 2-12 c. With the threshold, 1 M_70% shows the best combination of Young's modulus (~0.2 MPa), elongation at break (~150 %), and ionic conductivity (~ 10^{-3} S/cm) among

the SPEs studied and other references.^{29,65,66} Then, the next step is to fabricate and demonstrate an all-solid-state flexible supercapacitor using the 1 M_70% SPE.

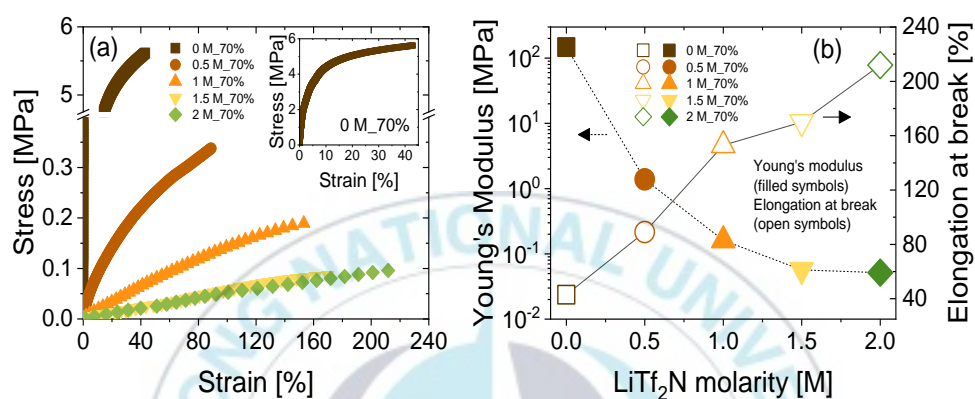


Figure 2-11. (a) Stress-strain curves of epoxy-based SPEs (0 M_70% in the inset) at room temperature. (b) Young's modulus (left axis, filled symbols) and elongation at break (right axis, open symbols) as a function of LiTf₂N molarity at room temperature.

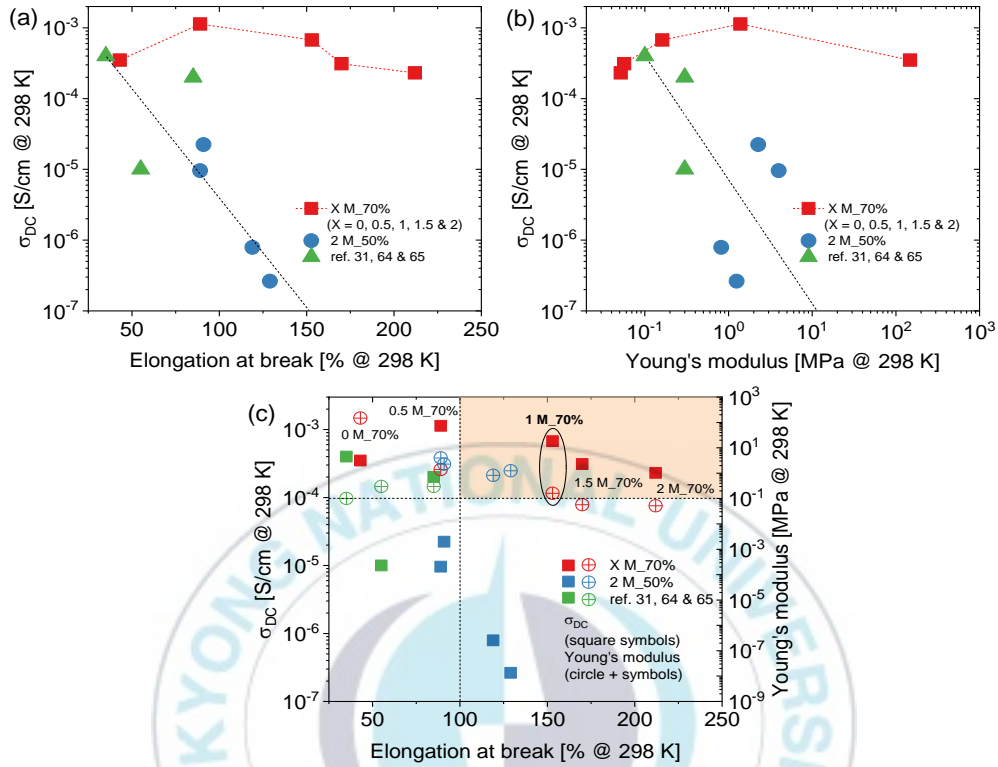


Figure 2-12. (a and b) Correlation plots of ionic conductivity vs either (a) elongation at break or (b) Young's modulus at room temperature for all the SPE studied [X M_70% and 2 M_50% (= LiTf₂N+TG+BT_50%, LiTf₂N+DT+BT_50%, LiTf₂N+TG_50%, and LiTf₂N+DT_50%)], including literature data from ref 31, 64, and 65. Dashed lines are only guides for the eye. (c) Multifunctional plot of room temperature ionic conductivity (left axis, square symbols) and Young's modulus (right axis, circle + symbols) as a function of elongation at break. The only 1 M_70% SPE is located in the orange area, where SPE has $\sigma_{DC} \geq 10^{-4}$ S/cm, elongation at break > 100%, and Young's modulus > 0.1 MPa at the same time.

II-3.6 Electrochemical Property of Solid-State Supercapacitor

To verify this epoxy-based solid polymer electrolytes as solid electrolytes for all-solid-state supercapacitors, their electrochemical measurements were conducted in the supercapacitor symmetric cell, where the epoxy-based SPE (1 M_70%) was assembled with the two activated carbon (AC) electrodes, at room temperature (Figure 2-13). Figure 2-13 a exhibits the scan rate (10 – 100 mV/s) dependent cyclic voltammetry (CV) curves of the supercapacitor pouch cell, whose photograph is shown in the inset of Figure 2-13 a, indicating electrical double-layer capacitor with a stable and symmetric shape between 0 and 3 V. To further evaluate the energy storage function of the supercapacitor, the galvanostatic charge-discharge (GCD) tests were performed with multiple current densities ranging from 0.1 to 1.8 A/g (Figure 2-13 b). The linear potential-time relation indicates stable performance of the supercapacitor during the charge-discharge cycle under 3 V, consistent with the observation from the CV tests. Although a current-resistance (IR) drop was observed in the discharge curves, this is probably due to relatively high contact resistance at the interface between the AC electrode and epoxy-based electrolyte (or internal resistance of the electrode).⁶⁷ For the supercapacitor device, its specific capacitance (C) values were then estimated from each GCD discharge curve excluding the IR drop part using the following equation,³⁴

$$C = 2 \frac{I}{m \cdot dV / dt} \quad (2-8)$$

wherein I , m , and dV/dt are the applied current, the mass of active materials in an electrode, and the slope of the discharge curve [voltage (V) vs time (t)], respectively.

In Figure 2-13 c showing the specific capacitance as a function of current density (green square symbols), the specific capacitance monotonically decreases with increasing discharge current density, ascribed to larger IR drop at larger current density. The highest specific capacitance value obtained from the epoxy SPE/AC-based supercapacitor is ~180 F/g at a current density of 0.1 A/g, and this value is much higher than those obtained from other epoxy SPE-based supercapacitors (~90 F/g at 0.13 A/g)³⁴ as well as ionic liquid electrolyte-based supercapacitors (< 85 F/g)⁶⁸⁻⁷¹ using the two AC electrodes. With the specific capacitance values, the energy (E) and power (P) density of the supercapacitor can be calculated using $E = 0.5CV^2$ and $P = E/t$ as shown in Figure 2-13 c displaying the Ragone plot of power density vs energy density (blue circle symbols). Our all-solid-state supercapacitor shows an energy density up to $E \sim 222$ Wh/kg and a power density up to $P \sim 14.1$ kW/kg at operating voltage of 3 V. This electrochemical performance is superior to that of other solid-state supercapacitors (Figure 2-14 and Table 2-2), where their specific capacitance, energy and power densities are in the range of 29 to 124 F/g, 21 to 75 Wh/kg, and 2 to 25 kW/kg, respectively. The long-term cycling stability of the supercapacitor was also explored in a potential window of 0 – 3 V via consecutive GCD cycling at a current density of 0.6 A/g (Figure 2-13 d). The capacitance

retention displays that the stable cycling characteristic is maintained during the 1000 cycles; i.e., after 100 charge-discharge cycles, the capacitance retention is ~91% and even after 1000 cycles, the supercapacitor retains a capacitance value as high as ~90% of the initial capacitance. Electrochemical impedance spectroscopy (EIS) measurements were also conducted in the supercapacitor, and the resultant Nyquist plots before and after the cycling test are depicted in the inset of Figure 2-13 d. The Nyquist plot was not changed even after 1000 continuous cycles (red circle symbols), compared to that obtained from the first cycle (blue square symbols), further indicating the good electrochemical cycling stability of our supercapacitor. The practical application of the superacapacitor was further demonstrated by powering light-emitting diode (LED). Our device could successfully turn on and off the red LED (1.8 – 2.1 V, 20 mA, 3 mm diameter) as shown in Figures 2-13 e and 2-13 f.

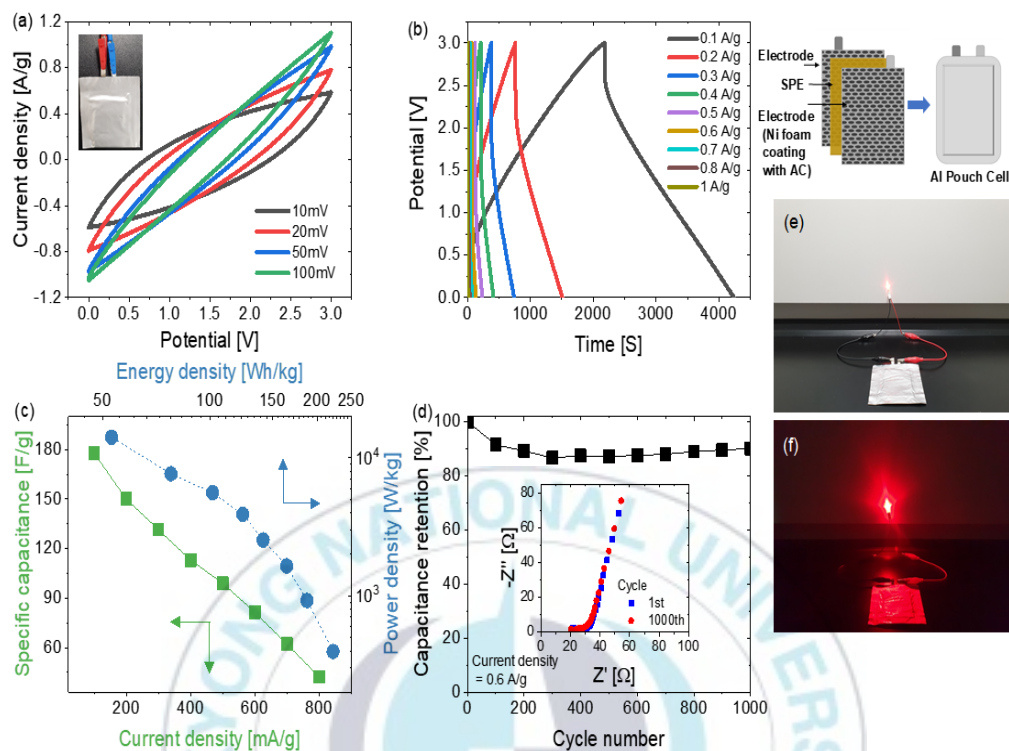


Figure 2-13. Electrochemical properties of all-solid-state supercapacitor composed of the epoxy-based SPE (1 M_70%) and two AC electrodes. (a) Potential dependence of current density (CV profiles) at different scan rates from 10 to 100 mV/s with the inset showing a photograph of the supercapacitor pouch cell. (b) Time dependence of potential (GCD profiles) at various current densities from 0.1 to 1 A/g. (c) Specific capacitance vs. current density (square symbols, left and bottom axes) and Ragone plot of power density vs. energy density (circle symbols, right and top axes). (d) Capacitance retention as a function of cycle number (Nyquist plot of the supercapacitor before and after cycling in the inset). (e and f) Photographs show the device powering a LED.

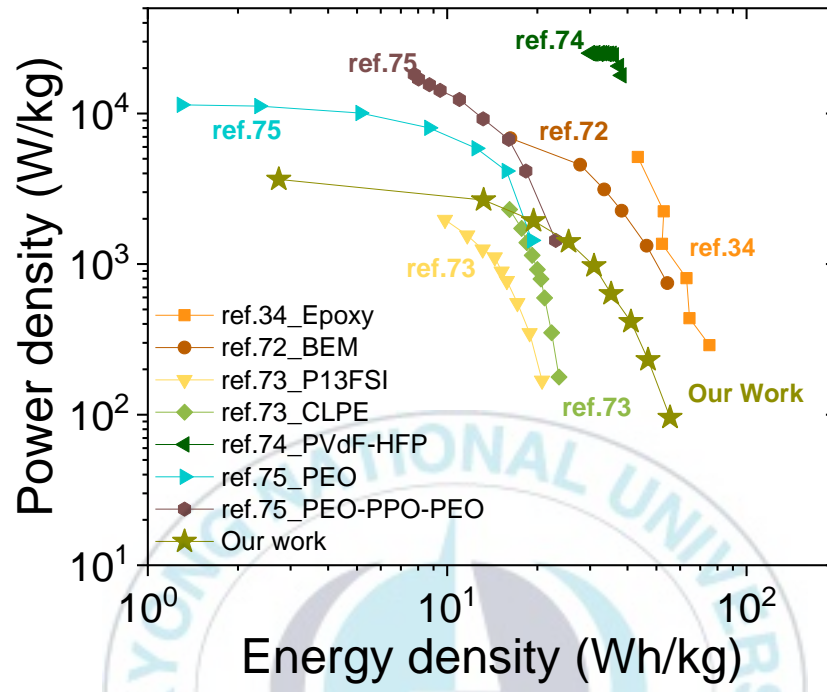


Figure 2-14. Ragone plot of power density vs. energy density of our supercapacitor, compared with literature values.

Table 2-2. Electrochemical Performance of Either SPE- or GPE-based Supercapacitors

Active materials	Polymer electrolyte	σ_{DC} at 25 °C [S/cm]	Specific capacitance [F/g]	Maximum energy density [Wh/kg]	Maximum power density [kW/kg]	Operating voltage	ref
AC	Epoxy based SPEs	6.9×10^{-4}	90 at 0.13A/g	75.2	9.3	0-2.5V	34
r-GO	BEM based GPEs	5.13×10^{-3}	39 at 0.5Ag	54.4	11.3	0-3.2V	72
r-GO	PEO based GPEs	2.14×10^{-3}	36 at 0.5A/g	47.3	3.8	0-3.2V	72
AC	P ₁₃ FSI based GPEs	9.9×10^{-3}	35 at 0.15A/g	23.6	2.0	0-2.5V	73
AC	CLPE based GPEs	1.6×10^{-3}	29 at 0.15A/g	20.7	2.3	0-2.5V	73
AC	PVdF-HFP based GPEs	6.4×10^{-3}	109 at 0.2A/g	38.1	25.1	0-2.5V	74
AC/Gr	PEO based GPEs	3.0×10^{-4}	93.5 at 0.1A/g	19.2	11.4	0-3V	75
AC/Gr	PEO-PPO-PEO based GPEs	6.5×10^{-3}	123.6 at 0.1A/g	23.0	18.2	0-3V	75
AC	Carboxylated chitosan based SPEs	8.69×10^{-2}	45.9 at 0.5A/g	5.2	2.2	0-0.9V	76
AC	Epoxy based SPEs	1.13×10^{-3}	178 at 0.1A/g	55.5	3.25	0-3V	Our Work

To investigate the mechanical flexibility of the epoxy-based supercapacitor and its effect on the electrochemical performance, the bending and rolling tests were carried out by continuously deforming the device at a diameter of 3 cm (bending) or 1.4 cm (rolling), as shown in Figure 2-15 a. The electrochemical characteristic of the epoxy/AC-based supercapacitor was first studied by CV experiments at 20 mV/s under two different mechanical deformations. When the flexible supercapacitor is bent, rolled, and then recovery to flat, no obvious CV changes are observed in Figure 2-15 b, demonstrating good electrochemical reliability of the devices during bending and rolling deformations. Its GCD experiments were also conducted at a current density of 0.7 A/g, and the calculated specific capacitance increases nearly 32 – 50% from 63 F/g (flat initial) to 94 F/g (bending), 83 F/g (rolling), and 87 F/g (flat recovery), as shown in Figure 2-15 c. This is presumably due to the bending processes facilitating contact between the AC electrode and epoxy SPE, resulting in an increase in the capacitance.⁷⁷ We further investigated the capacitance retention of the device under the rolling deformation, and observed a remarkable capacitive retention of ~80% even after the supercapacitor was continuously operated under the harsh rolling condition for 2000 cycles (Figure 2-15 d). This suggests a good mechanical integrity of the flexible supercapacitor, which still powers a LED even under the bending (Figure 2-15 e) and rolling (Figure 2-15 f) deformations.

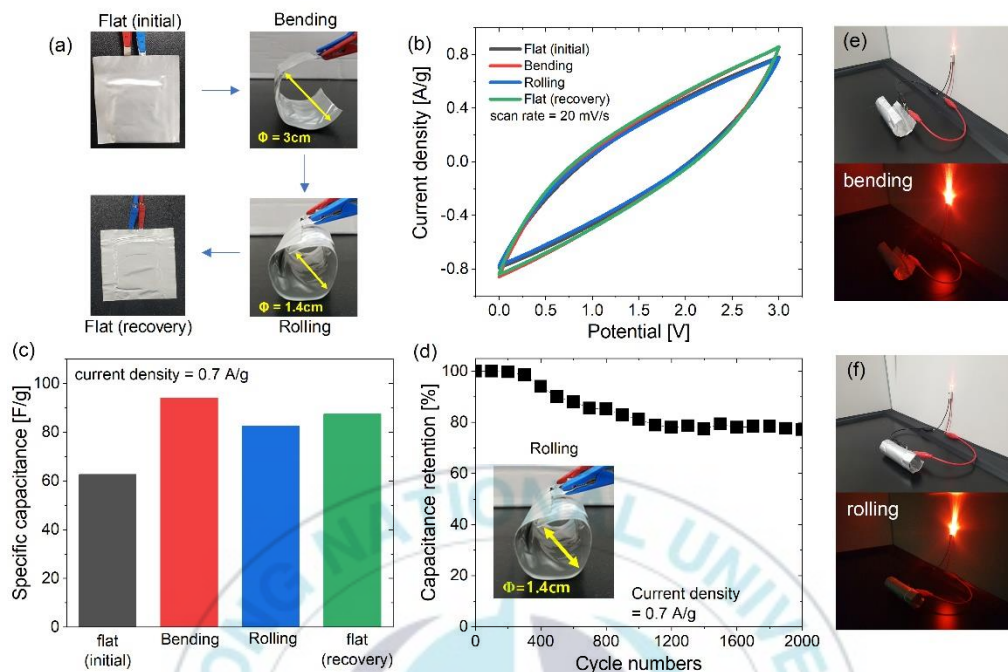


Figure 2-15. (a) Bending and rolling tests of epoxy/AC-based supercapacitor demonstrating a good flexibility. (b) CV curve comparison at 20 mV/s of flat (initial), bending, rolling, and flat (recovery) states, where no obvious change of capacitance is observed. (c) Specific capacitance obtained from GCD test at a current density of 0.7 A/g under four different mechanical deformation conditions. (d) Capacitance retention at a current density of 0.7 A/g under rolling. (e and f) Photographs show the supercapacitor powering a LED under (e) bending and (f) rolling.

II-4. Conclusions

We successfully demonstrate a simple and easy method to prepare a multifunctional solid polymer electrolyte by controlling Li salt concentration for the development of safe and flexible supercapacitors. The chemically cross-linked epoxy-based SPE was combined with a plasticizing oligoether, a high ion conducting ionic liquid, and a weak-binding Li salt, via single-pot ring opening polymerization. The polymerization leads to a bicontinuous microphase separation into microscopic fast ion-diffusing channel and macroscopic mechanical supporting cross-linked framework, consistent with the microstructural investigation of percolating pores as well as the observation of the two glass transition temperatures and low tortuosity. The ionic conductivity is enhanced with a decrease in the LiTf₂N molarity, so that the 0.5 M LiTf₂N-containing SPE with nano-scale phase separation exhibits the highest room temperature conductivity (1×10^{-3} S/cm) among the SPEs studied. The lower conductivity in the SPE with micro-scale phase separation (0 M_70%) than with nano-scale phase separation (0.5 M_70%) is due to interfacial polarization that causes ions to be trapped or immobile at the interface, consistent with the higher activation energy of ion conduction in the micro-scale phase separated SPE ($E_a^{0\text{ M}_70\%} > E_a^{0.5\text{ M}_70\%}$). The LiTf₂N molarity also modulates the SPE mechanical properties; i.e., increasing LiTf₂N content leads to an increase in the SPE flexibility. Furthermore, the flexible solid-state symmetrical supercapacitor, fabricated with this SPE and AC electrodes, provide a broad electrochemical potential window of 3 V, high specific capacitance of 178 F/g at 0.1 A/g, large energy and power density (55.5 Wh/kg at 99 W/kg and 3.25 kW/kg at

16.25 Wh/kg), and good capacitance retention of 90% over 1000 cycles. This outstanding electrochemical performance still maintains in this supercapacitor under bending and rolling tests, reflecting the simultaneous achievement of electrochemical and mechanical stabilities.



II-5. References

1. Dong, L. *et al.* Flexible electrodes and supercapacitors for wearable energy storage: A review by category. *J. Mater. Chem. A* **4**, 4659–4685 (2016).
2. Pan, S., Ren, J., Fang, X. & Peng, H. Integration: An Effective Strategy to Develop Multifunctional Energy Storage Devices. *Adv. Energy Mater.* **6**, 1–19 (2016).
3. Yao, B. *et al.* Paper-Based Electrodes for Flexible Energy Storage Devices. **1700107**, (2017).
4. Wang, X., Liu, Z. & Zhang, T. Flexible Sensing Electronics for Wearable/Attachable Health Monitoring. *Small* **13**, 1–19 (2017).
5. Lee, S., Jeong, D., Mativenga, M. & Jang, J. Highly Robust Bendable Oxide Thin-Film Transistors on Polyimide Substrates via Mesh and Strip Patterning of Device Layers. *Adv. Funct. Mater.* **27**, 1–9 (2017).
6. Raza, W. *et al.* Recent advancements in supercapacitor technology. *Nano Energy* **52**, 441–473 (2018).
7. Heo, J. S., Eom, J., Kim, Y. H. & Park, S. K. Recent Progress of Textile-Based Wearable Electronics: A Comprehensive Review of Materials, Devices, and Applications. *Small* **14**, 1–16 (2018).
8. Chen, X., Rogers, J. A., Lacour, S. P., Hu, W. & Kim, D. H. Materials chemistry in flexible electronics. *Chem. Soc. Rev.* **48**, 1431–1433 (2019).
9. Sun, C., Liu, J., Gong, Y., Wilkinson, D. P. & Zhang, J. Recent advances in all-solid-state rechargeable lithium batteries. *Nano Energy* **33**, 363–386 (2017).
10. Zhong, C. *et al.* A review of electrolyte materials and compositions for electrochemical supercapacitors. *Chem. Soc. Rev.* **44**, 7484–7539 (2015).
11. Manthiram, A., Yu, X. & Wang, S. Lithium battery chemistries enabled by solid-state electrolytes. *Nat. Rev. Mater.* **2**, 1–16 (2017).
12. Bachman, J. C. *et al.* Inorganic Solid-State Electrolytes for Lithium Batteries: Mechanisms and Properties Governing Ion Conduction. *Chem. Rev.* **116**, 140–162 (2016).
13. Wang, Q., Jiang, L., Yu, Y. & Sun, J. Progress of enhancing the safety of lithium ion battery from the electrolyte aspect. *Nano Energy* **55**, 93–114 (2019).

14. Long, L., Wang, S., Xiao, M. & Meng, Y. Polymer electrolytes for lithium polymer batteries. *J. Mater. Chem. A* **4**, 10038–10069 (2016).
15. Yue, L. *et al.* All solid-state polymer electrolytes for high-performance lithium ion batteries. *Energy Storage Mater.* **5**, 139–164 (2016).
16. Miller, T. F., Wang, Z. G., Coates, G. W. & Balsara, N. P. Designing polymer electrolytes for safe and high capacity rechargeable lithium batteries. *Acc. Chem. Res.* **50**, 590–593 (2017).
17. Morris, M. A., An, H., Lutkenhaus, J. L. & Epps, T. H. Harnessing the Power of Plastics: Nanostructured Polymer Systems in Lithium-Ion Batteries. *ACS Energy Lett.* **2**, 1919–1936 (2017).
18. Zhang, H. *et al.* Single lithium-ion conducting solid polymer electrolytes: advances and perspectives. *Chem. Soc. Rev.* **46**, 797–815 (2017).
19. Fenton, D. E., Parker, J. M. & Wright, P. V. Complexes of alkali metal ions with poly(ethylene oxide). *Polymer (Guildf)*. **14**, 589 (1973).
20. Cheng, X., Pan, J., Zhao, Y., Liao, M. & Peng, H. Gel Polymer Electrolytes for Electrochemical Energy Storage. **1702184**, 1–16 (2017).
21. Young, W. S., Kuan, W. F. & Epps, T. H. Block copolymer electrolytes for rechargeable lithium batteries. *J. Polym. Sci. Part B Polym. Phys.* **52**, 1–16 (2014).
22. Shin, D. W., Guiver, M. D. & Lee, Y. M. Hydrocarbon-Based Polymer Electrolyte Membranes: Importance of Morphology on Ion Transport and Membrane Stability. *Chem. Rev.* **117**, 4759–4805 (2017).
23. Seo, M. & Hillmyer, M. A. Reticulated Nanoporous Polymers by Controlled Polymerization-Induced Microphase Separation. *Science (80-.)*. **336**, 1422–1425 (2012).
24. Schulze, M. W., McIntosh, L. D., Hillmyer, M. A. & Lodge, T. P. High-modulus, high-conductivity nanostructured polymer electrolyte membranes via polymerization-induced phase separation. *Nano Lett.* **14**, 122–126 (2014).
25. Bae, S.-H. *et al.* Load-bearing supercapacitor based on bicontinuous PEO-b-P(S-co-DVB) structural electrolyte integrated with conductive nanowire-carbon fiber electrodes. *Carbon N. Y.* **139**, 10–20 (2018).
26. Chopade, S. A. *et al.* Robust Polymer Electrolyte Membranes with High Ambient-Temperature Lithium-Ion Conductivity via Polymerization-Induced Microphase Separation. *ACS Appl. Mater. Interfaces* **9**, 14561–14565 (2017).

27. Shirshova, N. *et al.* Structural supercapacitor electrolytes based on bicontinuous ionic liquid–epoxy resin systems. *J. Mater. Chem. A* **1**, 15300 (2013).
28. Shirshova, N. *et al.* Composition as a Means To Control Morphology and Properties of Epoxy Based Dual-Phase Structural Electrolytes. *J. Phys. Chem. C* **118**, 28377–28387 (2014).
29. Westover, A. S. *et al.* Multifunctional high strength and high energy epoxy composite structural supercapacitors with wet-dry operational stability. *J. Mater. Chem. A* **3**, 20097–20102 (2015).
30. Ihrner, N., Johannisson, W., Sieland, F., Zenkert, D. & Johansson, M. Structural lithium ion battery electrolytes: Via reaction induced phase-separation. *J. Mater. Chem. A* **5**, 25652–25659 (2017).
31. Jang, H. K., Jung, B. M., Choi, U. H. & Lee, S. B. Ion Conduction and Viscoelastic Response of Epoxy-Based Solid Polymer Electrolytes Containing Solvating Plastic Crystal Plasticizer. *Macromol. Chem. Phys.* **219**, (2018).
32. Choi, U. H. & Jung, B. M. Ion Conduction, Dielectric and Mechanical Properties of Epoxy-Based Solid Polymer Electrolytes Containing Succinonitrile. *Macromol. Res.* **26**, 459–465 (2018).
33. Kwon, S. J. *et al.* Influence of Al₂O₃ Nanowires on Ion Transport in Nanocomposite Solid Polymer Electrolytes. *Macromolecules* **51**, 10194–10201 (2018).
34. Kwon, S. J., Kim, T., Jung, B. M., Lee, S. B. & Choi, U. H. Multifunctional Epoxy-Based Solid Polymer Electrolytes for Solid-State Supercapacitors. *ACS Appl. Mater. Interfaces* acsami.8b11016 (2018). doi:10.1021/acsami.8b11016
35. Meng, C. *et al.* Multifunctional Structural Ultrabattery Composite. *Nano Lett.* **18**, 7761–7768 (2018).
36. Schneider, L. M., Ihrner, N., Zenkert, D. & Johansson, M. Bicontinuous Electrolytes via Thermally Initiated Polymerization for Structural Lithium Ion Batteries. *ACS Appl. Energy Mater.* **2**, 4362–4369 (2019).
37. Muralidharan, N. *et al.* Carbon Nanotube Reinforced Structural Composite Supercapacitor. *Sci. Rep.* **8**, 17662 (2018).
38. Ladpli, P., Nardari, R., Kopsaftopoulos, F. & Chang, F. K. Multifunctional energy storage composite structures with embedded lithium-ion batteries. *J. Power Sources* **414**, 517–529 (2019).

39. Park, B. *et al.* Influence of intermolecular interactions on molecular geometry and physical quantities in electrolyte systems. *Mol. Phys.* **0**, 1–6 (2018).
40. Shirshova, N. *et al.* Structural supercapacitor electrolytes based on bicontinuous ionic liquid-epoxy resin systems. *J. Mater. Chem. A* **1**, 15300–15309 (2013).
41. Rubinstein, M. & Colby, R. H. *Polymer Physics*. (Oxford University Press, 2003).
42. Kanamori, K., Nakanishi, K. & Hanada, T. Rigid macroporous poly(divinylbenzene) monoliths with a well-defined bicontinuous morphology prepared by living radical polymerization. *Adv. Mater.* **18**, 2407–2411 (2006).
43. Ollier-Dureault, V. & Gosse, B. Photooxidation of anhydride-cured epoxies: FTIR study of the modifications of the chemical structure. *J. Appl. Polym. Sci.* **70**, 1221–1237 (1998).
44. Diederichsen, K. M., Buss, H. G. & McCloskey, B. D. The Compensation Effect in the Vogel-Tammann-Fulcher (VTF) Equation for Polymer-Based Electrolytes. *Macromolecules* **50**, 3831–3840 (2017).
45. Echeverri, M., Kim, N. & Kyu, T. Ionic Conductivity in Relation to Ternary Phase Diagram of Poly(ethylene oxide), Succinonitrile, and Lithium Bis(trifluoromethane)sulfonimide Blends. *Macromolecules* **45**, 6068–6077 (2012).
46. Chen, Q. *et al.* Linear viscoelasticity and fourier transform infrared spectroscopy of polyether-ester-sulfonate copolymer ionomers. *Macromolecules* **47**, 3635–3644 (2014).
47. Wang, J. H. H. *et al.* Ion States and Transport in Styrenesulfonate Methacrylic PEO9 Random Copolymer Ionomers. *Macromolecules* **48**, 7273–7285 (2015).
48. J., S. & M., O. J. Modeling of transport of small molecules in polymer blends: Application of effective medium theory. *Polym. Eng. Sci.* **23**, 165–176 (2018).
49. Milhaupt, J. M. & Lodge, T. P. Homopolymer and small-molecule tracer diffusion in a gyroid matrix. *J. Polym. Sci. Part B Polym. Phys.* **39**, 843–859 (2001).
50. Wübbenhorst, M. & van Turnhout, J. Analysis of complex dielectric spectra. I. One-dimensional derivative techniques and three-dimensional modelling. *J. Non-Cryst. Solids* **305**, 40–49 (2002).
51. Choi, U. H. *et al.* Polymerized ionic liquids with enhanced static dielectric constants. *Macromolecules* **46**, 1175–1186 (2013).

52. Choi, U. H. *et al.* Dynamics of Precise Ethylene Ionomers Containing Ionic Liquid Functionality. *Macromolecules* **48**, 410–420 (2015).
53. Lee, M., Kwon, Y. K., Kim, J. & Choi, U. H. Effect of Poly(ethylene glycol) Crystallization on Ionic Conduction and Dielectric Response of Imidazolium-Based Copolyester Ionomers. *Macromolecules* **52**, 2314–2328 (2019).
54. Lee, M., Gibson, H. W., Kim, T., Colby, R. H. & Choi, U. H. Ion–Dipole-Interaction-Driven Complexation of Polyethers with Polyviologen-Based Single-Ion Conductors. *Macromolecules* **52**, 4240–4250 (2019).
55. Kremer, F. & Schönhals, A. *Broadband Dielectric Spectroscopy*. (Springer-Verlag, 2002).
56. Kohn, P., Schröter, K. & Thurn-Albrecht, T. Interfacial polarization and field-induced orientation in nanostructured soft-ion conductors. *Phys. Rev. Lett.* **102**, 216101 (2009).
57. Mijovic, J., Shen, M., Sy, J. W. & Mondragon, I. Dynamics and morphology in nanostructured thermoset network/block copolymer blends during network formation. *Macromolecules* **33**, 5235–5244 (2000).
58. Larranaga, M. *et al.* Cure kinetics of epoxy systems modified with block copolymers. *Polym. Int.* **53**, 1495–1502 (2004).
59. Serrano, E., Kortaberria, G., Arruti, P., Tercjak, A. & Mondragon, I. Molecular dynamics of an epoxy resin modified with an epoxidized poly(styrene-butadiene) linear block copolymer during cure and microphase separation processes. *Eur. Polym. J.* **45**, 1046–1057 (2009).
60. Castagna, A. M., Fragiadakis, D., Lee, H., Choi, T. & Runt, J. The role of hard segment content on the molecular dynamics of poly(tetramethylene oxide)-based polyurethane copolymers. *Macromolecules* **44**, 7831–7836 (2011).
61. Fragiadakis, D. & Runt, J. Molecular dynamics of segmented polyurethane copolymers: Influence of soft segment composition. *Macromolecules* **46**, 4184–4190 (2013).
62. Choi, U. H., Mittal, A., Price, T. L., Colby, R. H. & Gibson, H. W. Imidazolium-Based Ionic Liquids as Initiators in Ring Opening Polymerization : Ionic Conduction and Dielectric Response of End-Functional Polycaprolactones and Their Block Copolymers. *Macromol. Chem. Phys.* **217**, 1270–1281 (2016).
63. Wang, P., Xu, P., Wei, H., Fang, H. & Ding, Y. Effect of block copolymer containing ionic liquid moiety on interfacial polarization in PLA/PCL blends. *J. Appl. Polym. Sci.* 46161 (2018). doi:10.1002/app.46161

64. Harris, M. A. *et al.* Ion Transport and Interfacial Dynamics in Disordered Block Copolymers of Ammonium-Based Polymerized Ionic Liquids. *Macromolecules* **51**, 3477–3486 (2018).
65. Porcarelli, L., Gerbaldi, C., Bella, F. & Nair, J. R. Super Soft All-Ethylene Oxide Polymer Electrolyte for Safe All-Solid Lithium Batteries. *Sci. Rep.* **6**, 1–14 (2016).
66. Devaux, D. *et al.* Optimization of Block Copolymer Electrolytes for Lithium Metal Batteries. *Chem. Mater.* **27**, 4682–4692 (2015).
67. Zhang, L. L. & Zhao, X. S. Carbon-based materials as supercapacitor electrodes. *Chem. Soc. Rev.* **38**, 2520–2531 (2009).
68. Lazzari, M., Mastragostino, M. & Soavi, F. Capacitance response of carbons in solvent-free ionic liquid electrolytes. *Electrochem. commun.* **9**, 1567–1572 (2007).
69. Ania, C. O., Pernak, J., Stefaniak, F., Raymundo-Piñero, E. & Béguin, F. Solvent-free ionic liquids as in situ probes for assessing the effect of ion size on the performance of electrical double layer capacitors. *Carbon N. Y.* **44**, 3126–3130 (2006).
70. Chen, R. *et al.* Novel binary room-temperature complex system based on LiTFSI and 2-oxazolidinone and its characterization as electrolyte. *J. Phys. Chem. C* **111**, 5184–5194 (2007).
71. Largeot, C. *et al.* Relation between the ion size and pore size for an electric double-layer capacitor. *J. Am. Chem. Soc.* **130**, 2730–2731 (2008).
72. Jin, M. *et al.* High-Performance Ionic Liquid-Based Gel Polymer Electrolyte Incorporating Anion-Trapping Boron Sites for All-Solid-State Supercapacitor Application. *ACS Appl. Mater. Interfaces* **10**, 39570–39580 (2018).
73. Chaudoy, V., Tran Van, F., Deschamps, M. & Ghamouss, F. Ionic liquids in a poly ethylene oxide cross-linked gel polymer as an electrolyte for electrical double layer capacitor. *J. Power Sources* **342**, 872–878 (2017).
74. Pandey, G. P. *et al.* Thermostable gel polymer electrolyte based on succinonitrile and ionic liquid for high-performance solid-state supercapacitors. *J. Power Sources* **328**, 510–519 (2016).
75. Han, J. H., Lee, J. Y., Suh, D. H., Hong, Y. T. & Kim, T. H. Electrode-impregnable and cross-linkable poly(ethylene oxide)-poly(propylene oxide)-poly(ethylene oxide) triblock polymer electrolytes with high ionic conductivity and a large voltage window for flexible solid-state supercapacitors. *ACS Appl. Mater. Interfaces* **9**, 33913–33924 (2017).

76. Yang, H., Liu, Y., Kong, L., Kang, L. & Ran, F. Biopolymer-based carboxylated chitosan hydrogel film crosslinked by HCl as gel polymer electrolyte for all-solid-state supercapacitors. *J. Power Sources* **426**, 47–54 (2019).
77. Li, L. *et al.* Nitrogen-doped carbonized cotton for highly flexible supercapacitors. *Carbon N. Y.* **105**, 260–267 (2016).



Chapter III. High Stretchable and Ion Conductive Lithium acrylate Hydrogel polymer electrolyte for stretchable supercapacitors

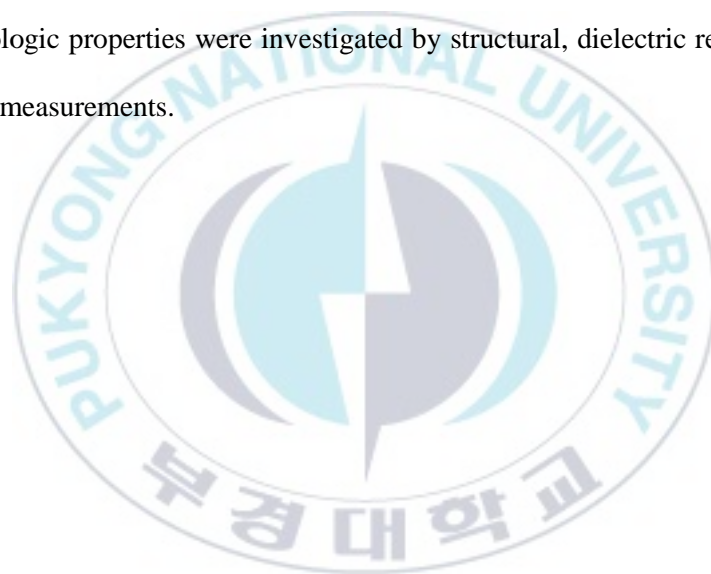
III-1. Introduction

Stretchable and flexible energy storage is becoming increasingly important as we mention in previous pages. However, stretchable all-solid-state energy storages devices are difficult to develop, despite lots of researchers were studied on them.¹⁻⁴ To develop stretchable all-solid-state energy storage devices, the unique properties of the material for the different components must be considered to mitigate unavoidable strain mismatches and interfacial resistance.⁵

Hydrogels have flexible and elastic properties due to crosslinked hydrated polymer chains having spaces filled with a high content of water.⁶ Also, as used at electrolyte, the charged functional groups on the polymer chains could effectively attract and localize the electrolytic ions within the network.⁷ These properties cause a high ionic conductivity which is similar to ionic liquids and also preserved the dimensional stability of the solid.⁸

Here, we prepared lithium acrylate-based high conductive, stretchable, and self-healable 3D network SPEs, where a lithium acrylate which has lithium-ion in polymer

functional group was chemically combined with cross-linkable silica nanoparticles containing vinyl groups (SNPs) and water as solvating lithium-ion, via a free radical polymerization. As a result, the lithium acrylate-based SPEs have a high ionic conductivity compared with ionic liquid, and a high stretchability, for the development of all-solid-state stretchable supercapacitors. To understand the role of each component and multifunctional physical properties of the SPEs, the effect of monomer type and molarity, SNPs concentration, and water concentration on conductivity, mechanical, and morphologic properties were investigated by structural, dielectric relaxation, and mechanical measurements.



III-2. Experimental Section

III-2.1 Materials

Triethoxyvinylsilane and Lithium Hydroxide (anhydrous) was purchased from Tokyo Chemical Industry and used as received. Acrylic acid, poly(vinylidene fluoride-*co*-hexafluoropropylene) (PVDF-HFP), and 1-methyl-2-pyrrolidinone (NMP) were purchased from Sigma Aldrich and used as received. Active carbon (AC with a surface area of 2000 m²/g) and conductive carbon (CC with a surface area of 62 m²/g) powders were purchased from MTL.



III-2.2 Synthesis of acrylic acid-based solid-state polymer electrolyte

High stretchable lithium acrylate-based SPEs were synthesized using three-step processes (shown in Figure 3-1), such as sol-gel reaction, lithium-ion exchange, and free radical polymerization. To prepare silica nanoparticles (SNPs) that are acting as covalent cross-linking points, triethoxyvinylsilane (0.95 g, Tokyo Chemical Industry) was vigorously mixed with de-ionized water (7.5 mL) via sol-gel reaction at ambient temperature during overnight (Figure 3-1a). To prepare lithium acrylate, acrylic acid (10 g, Sigma Aldrich) is mixing with lithium hydroxide (2.5 g, Tokyo Chemical Industry) using acetone as a solvent for 2 days and washed several times with acetone (Figure 3-1b). The free radical polymerization was used to chemically combine lithium acrylate (AALi) monomers as a network matrix with the as-prepared SNPs. A solution of lithium acrylate monomers in deionized water was added to the SNPs dispersion solution (0, 10, 20, 30, 40, 50, 60 wt%). The mixture was stirred vigorously for 30 mins, and then added ammonium persulfate (0.02 wt%, Alfa Aesar) as the initiator was added to the aqueous mixture. The solution was polymerized at 70 °C under nitrogen atmosphere for 2 hours to give solid-state SNPs cross-linking PAALi membrane (Figure 3-1c).

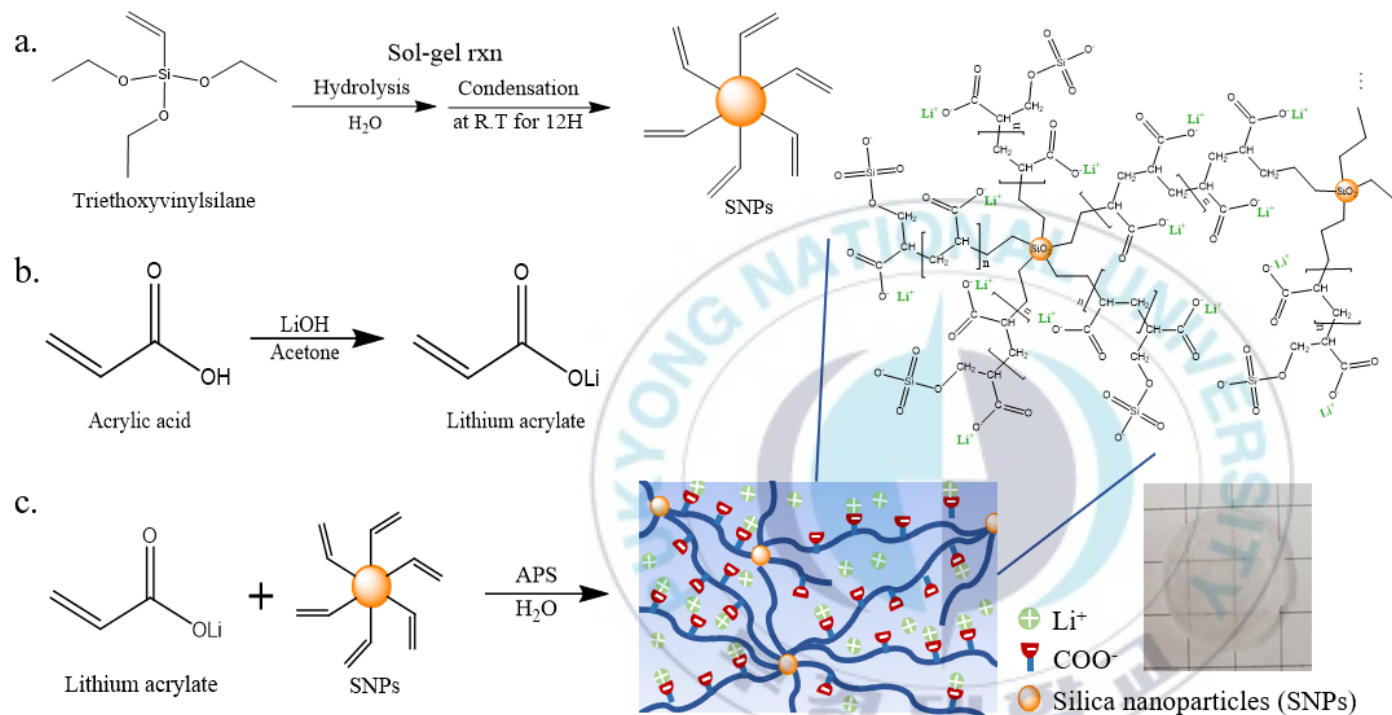


Figure 3-1. Synthesis of (a) vinyl silica nanoparticles, (b) lithium acrylate, and (C) poly(lithium acrylate) containing SNPs

III-2.3 Preparing stretchable all-solid-state supercapacitors

To make a tailorable supercapacitor, we get CNT fiber for KIMS. Using that CNT fiber, we soak two fibers at 20wt PAALi-SNPs solution and polymerization at 70°C for 2hours.



III-2.4 Characterization

FTIR spectra were investigated using a Perkin Elmer Spectrum X, equipped with a diamond attenuated total reflection cell, at room temperature. The plots were extracted CO₂ Peaks and the sample was measured as prepared.

Thermal stabilities of these SPEs were investigated by differential scanning calorimeter (DSC) using a TA Instrument Q2000 with 10 K/min heating and cooling rates under an inert atmosphere. DSC runs were repeated two times. Sample weights were maintained approximately 7-10 mg and sealed in an aluminum pan. The melting temperature (T_m), crystallization temperature (T_c) and glass transition temperature (T_g) were taken as the inflection point in the DSC thermogram from the second heating scan using TA Instruments Universal Analysis software.

FE-SEM images were recorded on JSM-6700F (JEOL), with an accelerating voltage of 15.0 kV, after Ag sputter coating for 30 min. To clearly observe SPE morphology, prior to FE-SEM analysis, each sample was freeze-dried for 3 days, allowing to extract water components from SPEs.

The stress-strain curves were measured using a 3340 Series universal testing machine (Instron, USA). Samples were cut into rectangular films with dimensions of approximately 20 (length) x 2 (width) x 1.5 (thickness) mm. All tensile tests were measured in a 100%/min strain ramp rate by gripped using a film tension clamp and each sample was tested at least five times to verify the data.

The ionic conductivity and complex permittivity measurements were conducted by Novocontrol GmbH Concept 40 broadband dielectric relaxation spectrometer using a sinusoidal voltage with amplitude 0.1 V. Samples were prepared by sandwiching SPE with ~1.5 mm thickness between two polished brass electrodes having two different diameters [such as 10 mm (top electrode) and 20 mm (bottom electrode)]. Data were collected in isothermal frequency sweeps from $10^7 - 10^{-1}$ Hz in the temperature range from 100 to -40 °C.

The electrochemical characteristics of the assembled AC/SPE/AC supercapacitor were investigated by cyclic voltammetry (CV) and galvanostatic charge-discharge (GCD) experiments using VSP 300 from Bio-Logic Science Instruments. The CV tests were conducted in a potential range from 0 to 0.6 V with a scan rate of 10, 20, 30, 50, and 100 mV/s. The GCD performance was explored at various current densities from 33.3 to 777.8 mA/g with the same potential range as the CV tests.

III-3. Result and Discussion

III-3.1 Structural properties of PAALi-SNPs

High stretchable lithium acrylate-based SPEs contained two main components, such as silica nanoparticles (SNPs) containing vinyl group and lithium acrylate. To confirm the SNPs are well synthesized via sol-gel reaction, we characterize of absorption peak with FT-IR analysis (Figure 3-2a) and all the band assignments are summarized in Table 3-1. From Figure 3-2a, triethoxyvinylsilane is possible to observe C-H asymmetric stretching in CH_3 at 2960cm^{-1} . However, SNPs cannot observe C-H asymmetric stretching in CH_3 due to condensation reaction from a sol-gel reaction. Around 1600 cm^{-1} broad bands are the result of stretching of different carbon double bond peak and it can prove the presence of vinyl groups at the surface in SNPs. Especially, we can observe a significant difference in the region $1150\text{-}750\text{ cm}^{-1}$ due to the stretching of Si-O-Si bonds⁹. Compared with triethoxyvinylsilane, SNPs show asymmetric stretching of Si-O-Si bonds at 1030 cm^{-1} and symmetric stretching of Si-O-Si bonds at 875 cm^{-1} . As shown in Figure 3-2b, the average SNPs sizes are 2-3nm as we can distinguish with the naked eye.

To confirm lithium acrylate monomers are well exchanged from acrylic acid, the lithium concentration values of lithium acrylate found through inductively coupled plasma analysis (See Figure 3-3) were compared with stoichiometric values. The result demonstrates that lithium ions of lithium acrylate are successfully exchanged from acrylic acid.

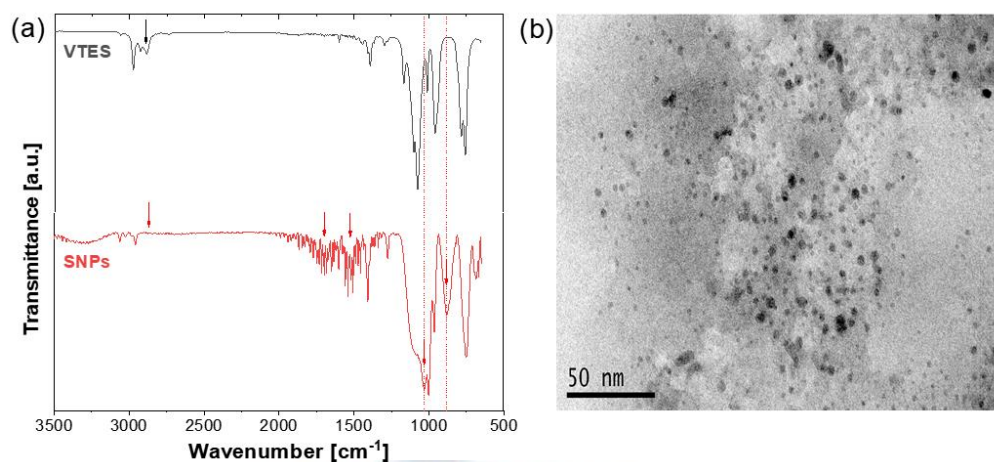


Figure 3-2. (a) FT-IR spectrum of VTES and SNPs (b) m-TEM (Transmission electron microscope) image of SNPs

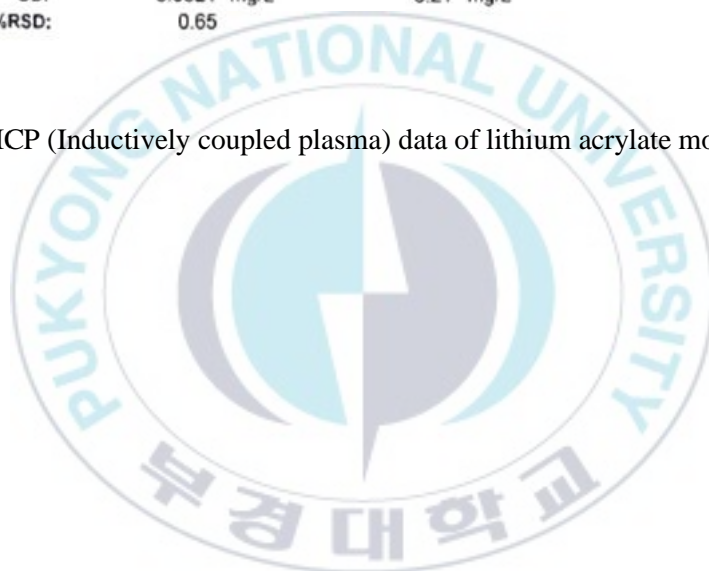
Table 3-1. Main peaks in the FT-IR spectrum of SNPs with their assignment according to refs.

Wavenumber (cm ⁻¹)	Assignment	Ref.
3500-3200	Water O-H stretching	10
2978	C-H stretching in CH ₃	11
2880	C-H symmetric stretching in O-CH ₃	9
1600	C=C stretching	12
1100	Si-O asymmetrical stretching vibrations	13
1030	Si-O-Si asymmetric stretching	14
875	Si-O-Si symmetric stretching	9
755	Si-O symmetric stretching vibrations	15

Li

Seq. No.	12	AS Loc:	35	Date:	2018-11-30 오후 2:46:1
Sample ID:	Li [100X]				
Analyte		Conc (Calib)	Conc (Sample)	Net Intensity	Corr. Intensity
Li 610.362					
	9.588 mg/L	958.8 mg/L		2,545,649.9	2
	9.550 mg/L	955.0 mg/L	2,434,177.0	2,534,823.8	2
	9.683 mg/L	968.3 mg/L	2,472,438.2	2,573,085.1	2
	9.552 mg/L	955.2 mg/L	2,434,615.3	2,535,262.1	2
	9.662 mg/L	966.2 mg/L	2,466,247.5	2,566,894.3	2
Mean:	9.607 mg/L	960.7 mg/L		2,551,143.0	
SD:	0.0621 mg/L	6.21 mg/L			
%RSD:	0.65				

Figure 3-3. ICP (Inductively coupled plasma) data of lithium acrylate monomer



To inspect the complexation and interactions between samples which is polymerized, FT-IR spectra are analyzed to compare the difference of lithium ion-based PAALi-SNPs and proton ion-based PAA-SNP (See Figure 3-4). All the band assignments of PAA-SNPs and PAALi-SNPs are summarized in Table 3-2. Apparently, for the PAA-SNPs sample, an intense peak is observed C=O stretching mode at 1700 cm^{-1} (See Figure 3-4(a)). However, as lithium-ion and carboxyl groups have a charge in the PAALi-SNPs system, the C=O band shifts to lower energy that asymmetric vibrational mode at 1547 cm^{-1} and symmetric vibrational mode at 1406 cm^{-1} due to deprotonation. This result demonstrates that lithium ions in poly(lithium acrylate) are ionized well in PAALi-SNPs. Both samples have silica nanoparticles which appear Si-O and Si-O-Si peaks in the region 1236 cm^{-1} and 1043 cm^{-1} , respectively.

Particularly, significant differences in the OH stretching bands of liquid water can be observed due to intermolecular interaction hydration structure (See Figure 3-4(b)). Each sample has two peaks in the O-H stretching bond which appear in the $3700 - 2800\text{ cm}^{-1}$ region. The higher frequencies peak at the 3400 cm^{-1} means the O-H stretching bond of the water, as it is generally accepted. The lowest wavenumber of the OH stretching band that is $3266, 3235\text{ cm}^{-1}$ can be assigned to that of the water molecules of the strongest hydrogen bond with the carboxylate of the polyacrylic acid and poly(lithium acrylate). It explains that the water molecules are in the first hydration layer which strongly bound with water and carboxylate of the polymer. To further investigate the interactions between samples and water, their FT-IR analysis was

explored with the multippeak fitting using the gaussian distribution. In the PAA-SNPs system, the ratio of each of two fitted peaks is about the same, indicating that the hydrogen bond interaction between water and carboxylic acid and the water interaction of PAA appear to be almost equivalent. However, in the PAALi-SNPs system, the distribution from the lowest wavenumber peak has a higher intensity, which means that the carboxylate and the water interaction is more dominate. And it also prevents the water can gather with other water molecules to form hydrogen bond interaction.

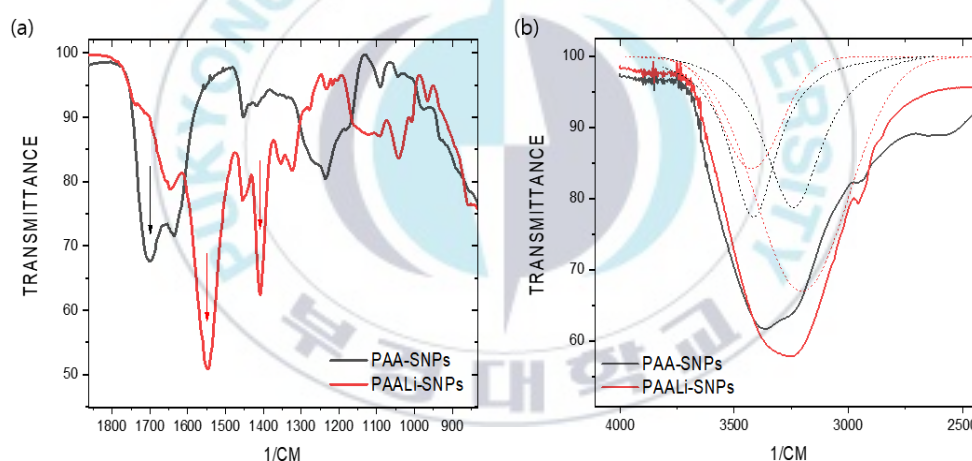


Figure 3-4. (a) Representative FT-IR spectrum of PAA-SNPs and PAALi-SNPs (b) The 3700 – 2800 cm^{-1} spectral region in OH peak (dashed curves in (b) are Gaussian fitting of OH peaks)

Table 3-2. All peaks in the FT-IR spectrum of PAA-SNPs and PAALi-SNP with their assignment according to refs.

Wavenumber (cm ⁻¹)	Assignment	Ref.
3400	Water O-H stretching	16
3266	Hydration water with PAA and O-H stretching mode of PAA	17,18
3235	Hydration water with PAALi	17
2950	C-H stretching in PAA	19
1700	C=O stretching mode of PAA	19
1547	C=O asymmetric vibrational mode in PAALi	20
1454	CH ₂ group asymmetric stretching mode of PAA	21
1416	In-plane C-O-H bonding vibrational mode of PAA	18
1406	C=O symmetric vibrational mode in PAALi	20
1236	Si-O asymmetrical stretching vibration	15
1089	C-O asymmetric stretching mode of PAA	21
1043	Si-O-Si asymmetric stretching	14
924	C-O symmetric stretching mode of PAA	18
782	CH ₂ rocking mode of PAA	18,19

III-3.2 Thermal Analysis

PAALi-SNPs have a strong relation with water due to its hydrogels. There was a traditional way to distinguish water molecules from the hydration shell²² using DSC. Cooling and heating experiments from 183.15 K to 353.15 K can investigate the difference in physical properties between frozen water in ice form (free water, freezing-bound water) and unfrozen water (non-freezing water) tightly bound to the polymer.^{16,17,22,23} Free water in the sample behaves like pure water and frozen around 0°C because it is unrelated to the polymer. Freezing-bound water is far from the polymer and melts at temperatures lower than water. Non-freezing water is limited to freezing around 0 °C, and the crystallization temperature (T_c) crystallizes well below 0 °C due to strongly fixing to the polymer through electrostatic interactions such as hydrogen bonding.

Figure 3-5 displays a representative DSC thermogram of PAA-SNPs and PAALi-SNPs, showing melting temperature (T_m) and crystallization temperature (T_c) that were observed in acrylic acid or lithium acrylate-based SPEs containing water as a solvent. The neat acrylic acid-based SPEs (PAA-SNPs) without lithium-ion has a larger $T_c = 256.75$ K that exothermic peak is appeared during water crystallization (See Figure 3-5 a). The melting peak is clearly observed two T_m peaks around 273.15 K in the inset of Figure 3-5 a, one is free water and the other is freezing-bound water. The melting enthalpy from T_m peaks is 204.3 J g^{-1} is lower than for the bulk water (ΔH_{m_water}

= 334 J g⁻¹)²⁴. However, in the PAA-SNPs system, there has a negligible effect due to weak interaction with PAA-SNPs system and water compared with PAALi-SNPs.

In Figure 3-5b, PAALi-SNPs has a significant difference that T_m and T_c were shifted to a lower temperature range ($T_m = 260.87$ K, $T_c = 219.70$ K). It demonstrates that freezing-bound waters melted at proportionally lower temperatures are dominate in PAALi-SNPs, and the melting enthalpy ($\Delta H_{m_PAALi-SNPs} = 92.90$ J g⁻¹) is also significantly lower than for the bulk water due to its different crystal morphology²². PAALi-SNPs also appeared cold crystallization behavior (T_{cc})²⁵ on heating which takes place when the sample is cooled rapidly and has no time to crystallize during the cooling phase. T_{cc} generally occurs in amorphous polymers where some glass parts of the polymer chain have enough mobility to crystallize during the heating scan. Since PAALi-SNPs with lithium ions in the polymer chain contains a lot of freezing-bound waters forming amorphous ice by quenching, unlike PAA-SNPs, PAALi-SNPs can be assumed that the amorphous parts appear as T_{cc} .²³

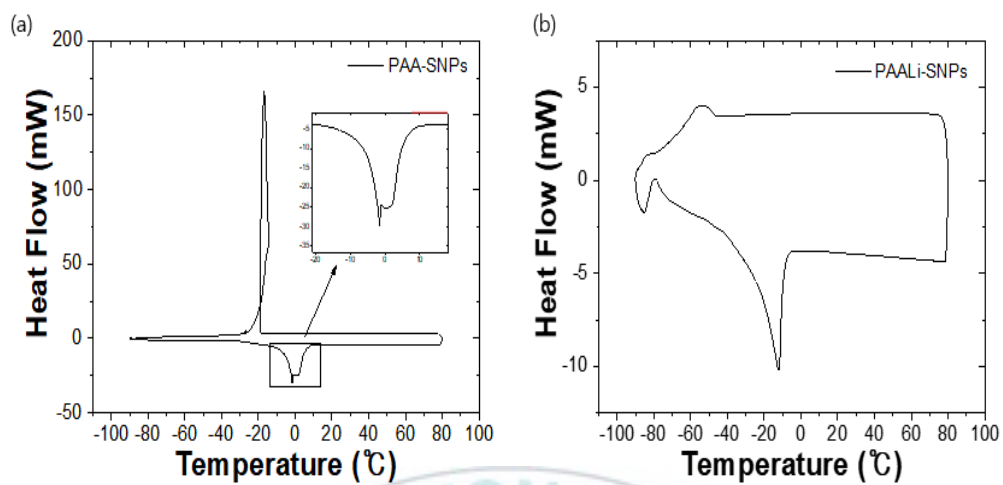


Figure 3-5. The DSC thermograms (a) PAA-SNPs (inset figure magnification of melting point) (b) PAALi-SNPs

III-3.3 Ionic Conductivity

The ionic DC conductivities of poly(acrylic acid) or poly(lithium acrylate) based SPEs were evaluated from the in-phase part of conductivities $\sigma'(\omega)$, where the DC conductivity σ_{DC} is a plateau value that is independent of frequency.²⁶ The temperature dependence of $\sigma_{DC}(T)$ for these two type of SPEs is displayed in Figure 3-6 (a) and (b). In Figure 3-6 (a), when PAA-SNPs was increased until 100°C, the DC conductivity was significantly dropped almost 2 order due to a weak binding with water solvent and counter-ion (proton). However, in Figure 3-5 (b), PAALi-SNPs relatively resist at water's boiling point because this system has a binding with water and counter-ion (lithium ion) as we can see at DSC data. To compare each sample more easily, we measure conductivities at 298K. Before raise the temperature, PAALi-SNPs is just one order higher conductivity than PAA-SNPs. However, after giving the high temperature, the differences with both samples are significantly increased to three order of conductivity (See Figure 3-6 (b)). It demonstrates that PAALi-SNPs has a resistance at high temperature although the sample contain water. Also, their $\sigma_{DC}(T)$ temperature dependence is well described by a Vogel-Tammann-Fulcher (VTF) equation.²⁷

$$\sigma_{DC}(T) = \frac{A}{T^{1/2}} \exp \left[-\frac{E_a}{R(T-T_0)} \right] \quad (3-1)$$

The solid curves in Figure 3-5a are fits to equation 3-1 with three parameters A, E_a , and T_0 , listed in Table 3-3, indicating the pre-exponential constant at infinite temperature (proportional to the number of charge carriers), the Vogel temperature, and

the activation energy for ion conduction, respectively. Based on the VFT fitting parameters, we can see that both PAA-SNP and PAALi-SNP show an increase in E_a due to water evaporation which has a role to transport ions as the solvent. PAA-SNPs's the pre-exponential constant A is almost approach to 0 S/cm $K^{1/2}$ because in this system there have a few charge carriers. (Acrylic acid $pK_a = 4.25$ at $25\text{ }^\circ\text{C}$)¹⁰

However, in the PAALi-SNPs system, the A is significantly increased because decreasing amounts of freezing-bound water with lithium-ion makes free-lithium ion having weak interaction.

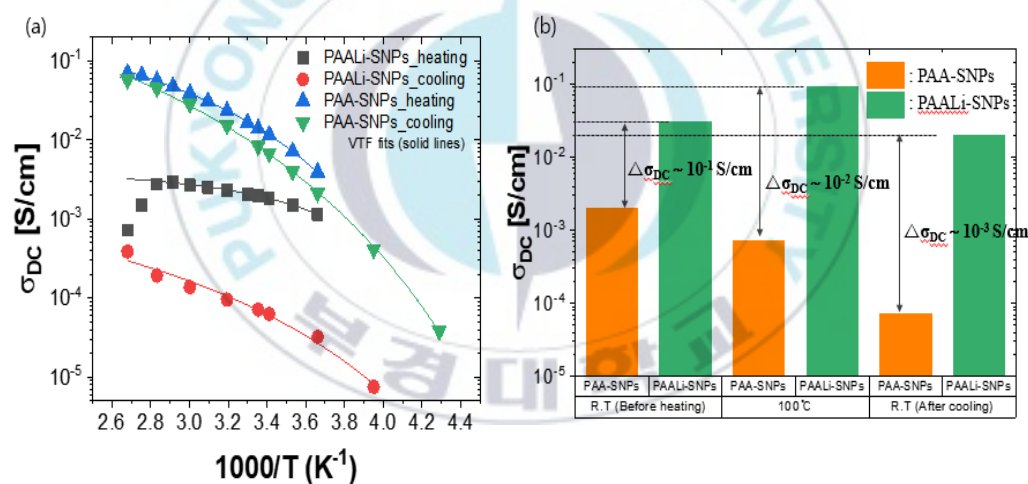


Figure 3-6. Temperature dependence on ionic conductivity and solid curves are VFT fitting Eq 3-1. (a) PAA-SNPs and PAALi-SNPs (b) Compare DC conductivity at 298K of PAA-SNPs and PAALi-SNPs

Table 3-3. Fitting Parameters of the VTF Equation for different charge carrier's DC conductivity, Eq 3-1.

Sample	A (S/cm K ^{1/2})	E _a (kJ/mol)	T ₀ (K)
PAA-SNPs_heating	0.12	0.81	219.66
PAA-SNPs_cooling	0.084	4.58	167.97
PAALi-SNPs_heating	15.76	3.56	195.24
PAALi-SNPs_cooling	64.42	6.97	161.17

As the PAALi-SNPs system have a high ionic conductivity property, we tried to change the monomer ratio containing lithium ions (See Figure 3-7). As the molarity of lithium acrylate increases, the pre-exponential constant A increases due to the number of lithium ions (See Table 3-4). However, the activation energy E_a is increasing according to the increasing molarity of lithium acrylate monomer, meaning that the ion migration is deteriorated by reducing the interaction between the solvent and the lithium ions. Therefore, we also give insight that interrelation between solvents and materials is important.

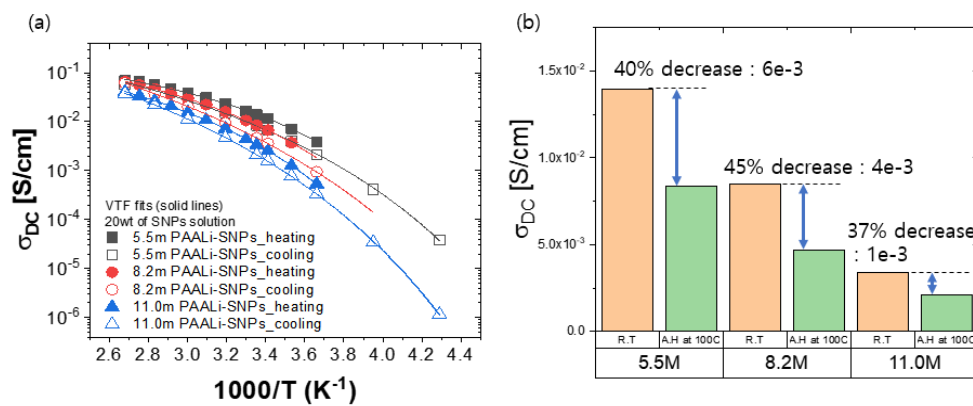


Figure 3-7. (a) The temperature dependence on ionic conductivity of different ratios of AALi monomer (5.49 m, 8.24 m, and 10.98 m) and solid curves are VTF fitting Eq. 3-1. (b) Compare DC conductivity at 298K (pristine and after heating at 100 °C) of different ratios of SPEs.

Table 3-4. Fitting Parameters of the VTF Equation for different ratios of monomer's DC conductivity, Eq 3-1.

Sample	A (S/cm K ^{1/2})	E _a (kJ/mol)	T ₀ (K)
5.49m PAALi-SNPs_heating	15.76	3.56	195.24
5.49m PAALi-SNPs_cooling	64.42	6.97	161.17
8.24m PAALi-SNPs_heating	29.38	4.76	189.99
8.24m PAALi-SNPs_cooling	190.23	9.20	155.63
10.98m PAALi-SNPs_heating	35.47	5.81	189.04
10.98m PAALi-SNPs_cooling	180.26	9.71	160.90

With the PAALi-SNPs system, we also tried to change SNPs concentration from 0 wt% to 60 wt%. The ionic conductivity was collected in isothermal frequency sweeps at room temperature. And the DC ionic conductivity (σ_{DC}) in Figure 3-8 was obtained by the plateau region in the in-phase part of conductivity $\sigma'(\omega)$ as mentioned in Chapter I-2.1.

In Figure 3-8, PAALi-SNPs_0wt which does not contain SNPs appeared 1.52×10^{-2} S/cm. The more concentration of SNPs this system has, the higher DC conductivity appeared until 20wt of SNPs (2.00×10^{-2} S/cm). The SNPs surface can appear dipole due to oxygen atom that bonding with silicon atoms. It makes poly(lithium acrylate) amorphous²⁸ and also assists ion transportation²⁹. Therefore, when SNPs insert into our system, it makes ionic segmental mobility increase and induces the higher ionic conductivity. However, more than 30 wt% of SNPs cause aggregation to block diffusion ions in the polymer chain, resulting in decreased ionic conductivity.

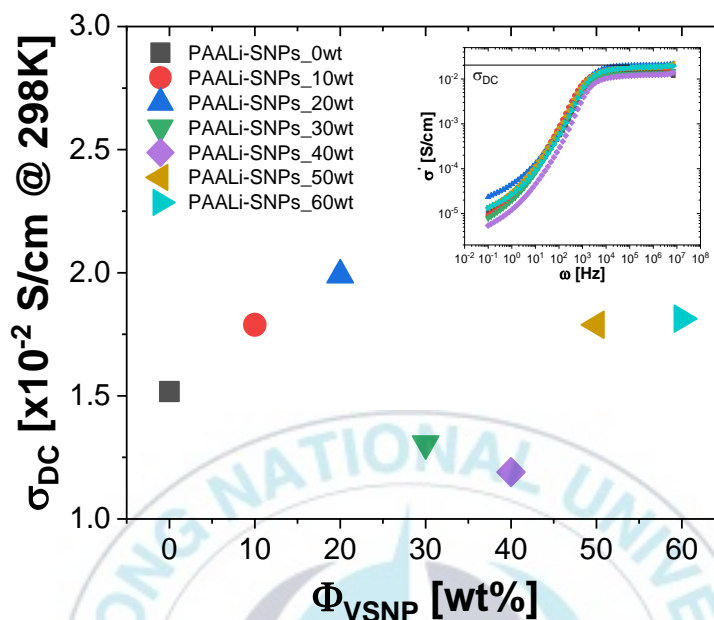


Figure 3-8. The ionic conductivity σ_{DC} of PAALi-SNPs with various content of SNPs at 298K. (Inset figure explains in-phase part of conductivity $\sigma'(\omega)$ as a function of angular frequency for the SPEs)

As can be seen from the DSC data, the relationship between water and lithium ions is very important. To know the effect of water at ionic conductivity, PAALi-SNPs was fully dried at 100°C for overnight and then soaked in water. Water has a role in solvating lithium-ion easier than without solvent so that immersing the water in the sample makes ionic conductivity higher. However, the water content of more than 70 wt% in the sample makes the ionic conductivity saturate due to all charge carriers already interact with water (See Figure 3-9).

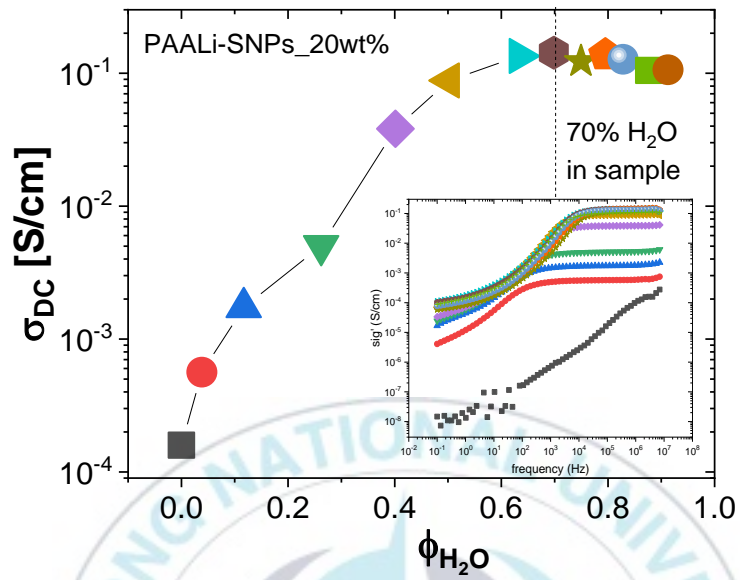


Figure 3-9. The ionic conductivity σ_{DC} of PAALi-SNPs with various content of water at 298K. (Inset figure explains in-phase part of conductivity $\sigma'_1(\omega)$ as a function of angular frequency for the SPEs)

III-3.4 Mechanical Property

To compare each sample (PAA-SNPs and PAALi-SNPs), the sample including the Li-ions has high mechanical properties such as tensile strength and elongation break even if it has the same amounts of SNPs (20 wt%) and monomer (See Figure 3-10 (a)). As we can see from Figure 3-10 (b), PAALi-SNPs's tensile strength is almost 4 times higher than pristine PAA-SP. Also, the PAALi-SNPs's elongation break is significantly higher than the other (See Figure 3-10 (c)).

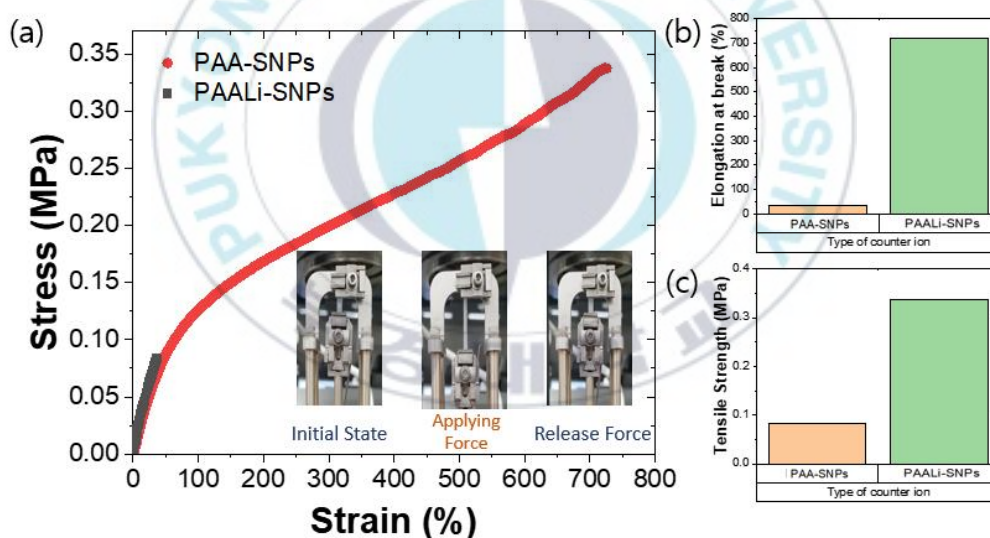


Figure 3-10. (a) Stress-strain curve of PAA-SNPs and PAALi-SNPs (b) Tensile strength of SPEs (c) Elongation break of SPEs

Furthermore, we investigate the effect of SNPs contents in the PAALi-SNPs system by comparing the elongation break values (See Figure 3-11 (a)). The higher content of SNPs shows the density of crosslinking points in the sample, indicating that have a strong effect on the mechanical properties.⁴ Also, PAALi-SNPs slightly appeared a self-healing property. The intermolecular secondary bonds between lithium-ion and the oxygen atom in the carboxyl group among the crosslinked polymer chains induced self-healing. In Figure 3-11 (b), we measured the stress-strain curve after self-healing at ambient temperature for each 1 hour. As a result, each self-healed sample of 1st and 2nd showed 200% and 150% elongation values. Although self-healing efficiency of elongation at break is low, the self-healing samples still have good stretchable properties. However, the self-healing efficiency of tensile strength is quite high value such as 0.75 and 0.8 (See Figure 3-11 (b) inset).

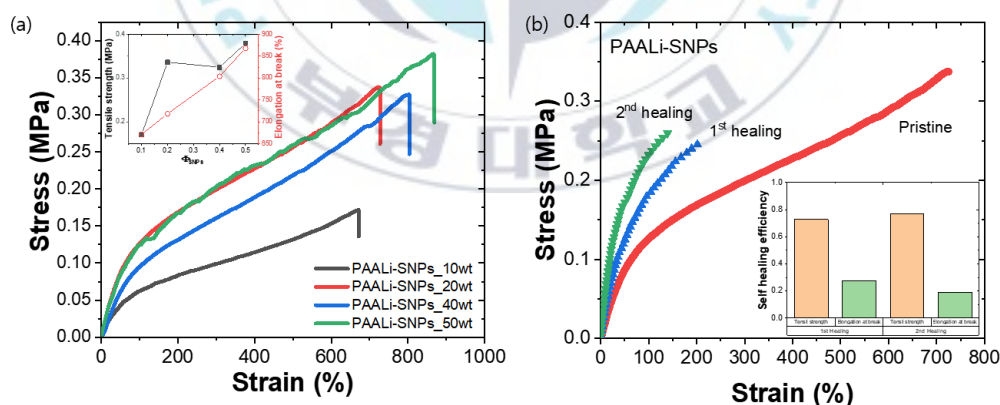


Figure 3-11. (a) Stress-strain curve of PAA-SNPs and PAALi-SNPs (b) Tensile strength of SPEs (c) Elongation break of SPEs

III-3.5 Morphology

To explain the phenomenon of mechanical property, we measured the morphology and Si atoms position of PAA-SNPs and PAALi-SNPs by Fe-SEM and EDS mapping (See Figure 3-12). PAA-SNPs shows well-dispersed SNPs in poly(acrylic acid) matrix. In Figure 3-12 (a), SNPs seem like invisible in PAA-SNPs as silica sizes are nano-size. However, we can confirm the silica using EDS mapping (See Figure 3-12 (c)). On the other hand, PAALi-SNPs show a micro-size of SNPs in poly(lithium acrylate) matrix due to SNPs aggregation caused by lithium acrylate monomer's charge. It leads that PAALi-SNPs have good stretchability than PAA-SNPs owing to low crosslinked point density, big crosslinked point size, and far crosslinked point distance.

When we changed the ratio of SNPs (20 wt%, 50 wt%, 60 wt%), the aggregation of SNPs is gradually increased as similar reasons for the former situation (See Figure 3-13). PAALi-SNPs_60 wt% looks highly aggregation of SNPs so that the silica blocking diffusion ions in the polymer chain. This phenomenon could support the reason for decreasing the ionic conductivity. Plus, we can observe increasing SNPs makes PAALi-SNPs series opaquer (Figure 3-14).

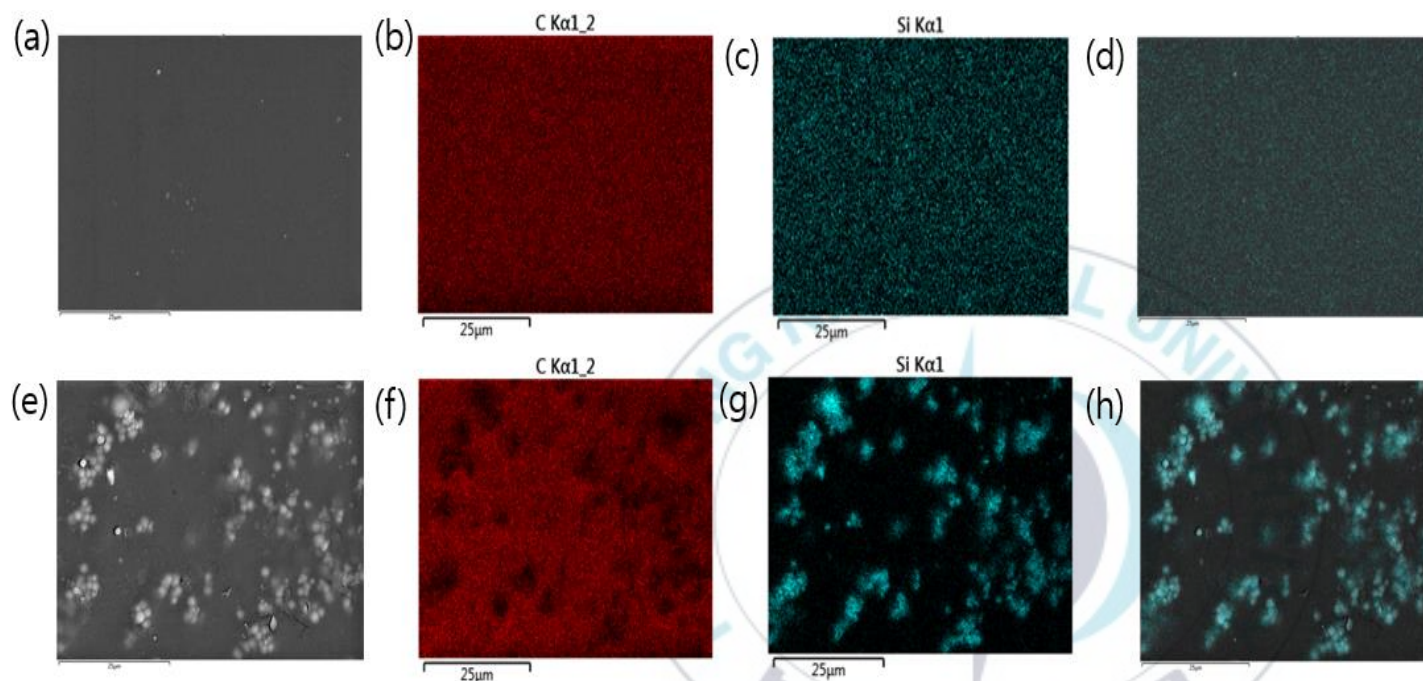


Figure 3-12. (a) Cross-sectional FE-SEM of PAA-SNPs (b-c) Elemental mapping of (b) carbon and (c) silica. (d) Overlapping image showing (a) and (c). (e) Cross-sectional FE-SEM of PAALi-SNPs (f-g) Elemental mapping of (f) carbon and (g) silica. (h) Overlapping image showing (e) and (g).

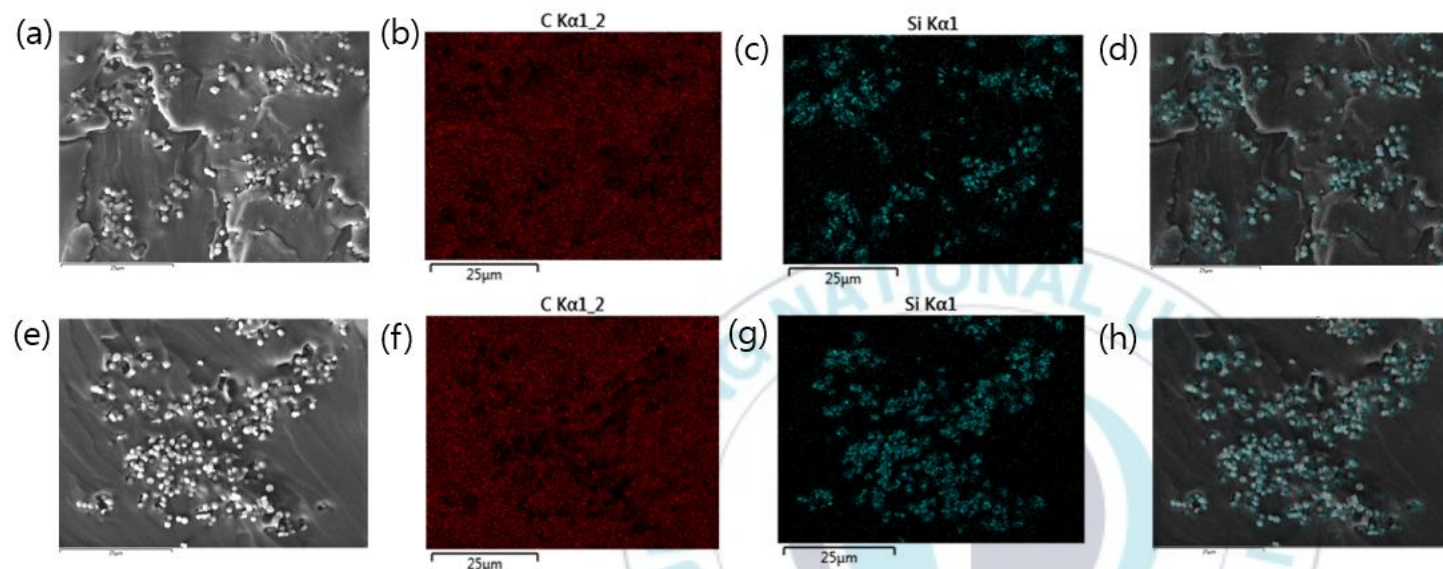


Figure 3-13. Cross-sectional FE-SEM of PAALi-SNPs_50wt% (b-c) Elemental mapping of (b) carbon and (c) silica. (d) Overlapping image showing (a) and (c). (e) Cross-sectional FE-SEM of PAALi-SNPs_60wt% (f-g) Elemental mapping of (f) carbon and (g) silica. (h) Overlapping image showing (e) and (g).



Figure 3-14. Appearance of Poly(lithium acrylate) SPEs with different ratio of SNPs

III-3.6 Electrochemical Property of fiber-shaped supercapacitor

To verify this lithium acrylate-based SPE as fiber-shaped supercapacitors for using at wearable devices, their electrochemical measurements were conducted in the fiber-shaped supercapacitors, where the lithium acrylate-based SPE (PAALi-SNPs_20 wt%) was coated with the two CNT-modified fiber electrodes at room temperature (Figure 3-15). Figure 3-15 (a) displayed a nearly rectangular-shaped window devoid of any redox peak within a potential range of 0 V to 0.6 V when cycled at a scan rate of 10 mV/s. Also, the CV curves retain their shape with a small difference even at the fast scan rate.³⁰

Galvanostatic Charge-Discharge (GCD) curves are shown nearly symmetric behavior without IR drop at 33.3 mA/g. It can explain high reversibility and storage capability at different current densities from 33.3 mA/g to 777.8 mA/g (See Figure 3-15 (b)).

The specific capacitance (C_s^{GCD} , Figure 9(c)) using the following equation³¹

$$C_s^{GCD} = 2 \frac{I}{g \times dV/dt} \quad (3-2)$$

where I is the applied current, g is the mas of electrode CNT fiber, and dV/dt is the slope of the discharge curve. The highest specific capacitance of 43 F/g is obtained from the poly(lithium acrylate) SPEs based supercapacitor at a current density of 11.11 mA^g⁻¹(See Figure 3-15 (c)). The CNT fibers generally have low specific capacitances,

for example, 4.5 Fg^{-1} .³² So, we can say our fiber shape supercapacitor is affordable to use. As we can see in Figure 3-15 (d), the poly(lithium acrylate) SPEs based supercapacitor indicated its excellent cycling stability by retained ~98% of its initial capacitance after 700 cycles.

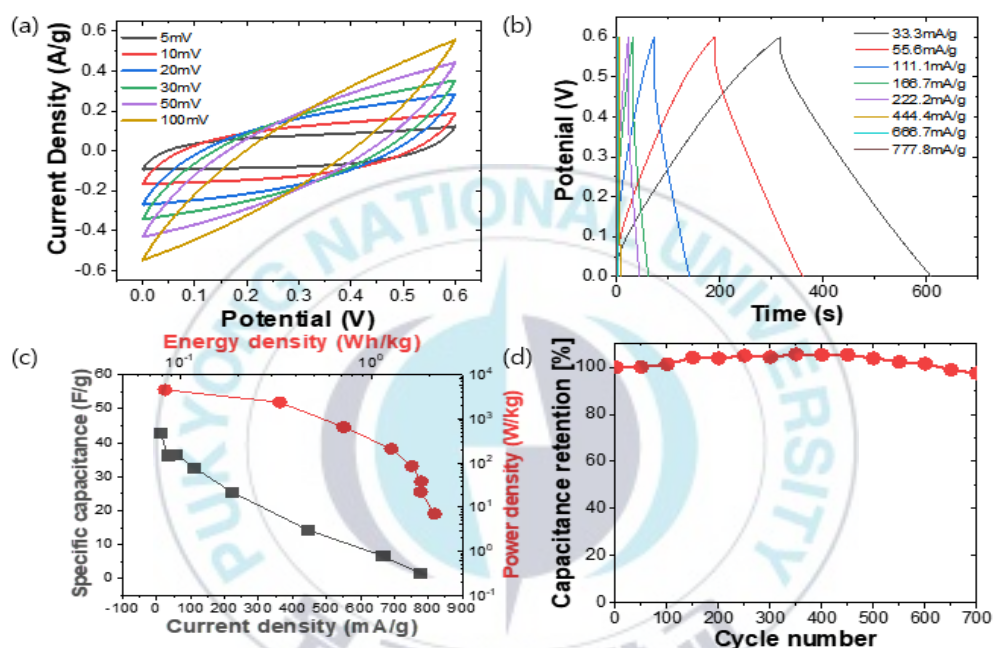


Figure 3-15. Electrochemical properties of fiber-shaped supercapacitor composed of the lithium acrylate-based SPE (PAALi-SNPs_20wt%). (a) Cyclic Voltammetry profiles at different scan rates from 10 to 100mV/s. (b) Galvanostatic charge-discharge profiles at various current densities from 33.3mA/g to 777.8mA/g. (c) Specific capacitance vs. current density (square symbols, left and bottom axes) and Ragone plot of power density vs. energy density (circle symbols, right and top axes). (d) Capacitance retention as a function of cycle number.

III-4. Conclusion

We successfully prepared PAALi-based SPEs with silica nanoparticles for the energy storage device. Compared poly(acrylic acid) containing proton, poly(lithium acrylate) SPEs based on lithium-ion exhibits high room temperature conductivity($\sigma_{DC} = 3.04 \times 10^{-2}$ S/cm) than PAA-SNPs conductivity($\sigma_{DC} = 1.97 \times 10^{-3}$ S/cm). In mechanical property, PAALi-SNPs appear highly stretchability until ~750%. Lithium aggregation (as a crosslinking point of SNP), observed by Fe-SEM, allows to boost stretchability as well as introduces a self-healing property. The cell using the PAALi-SNPs as an electrolyte exhibit stable cyclic retention. Therefore, the combination of the monomer, silica particles, and water plays a vital role in an improvement not only in ionic conductivity but also a mechanical property with a transparent appearance.

III-5. Reference

1. Li, H. *et al.* Ultraflexible and tailorable all-solid-state supercapacitors using polyacrylamide-based hydrogel electrolyte with high ionic conductivity. *Nanoscale* **9**, 18474–18481 (2017).
2. Zhao, Y. *et al.* Microgel-Enhanced Double Network Hydrogel Electrode with High Conductivity and Stability for Intrinsically Stretchable and Flexible All-Gel-State Supercapacitor. *ACS Appl. Mater. Interfaces* **10**, 19323–19330 (2018).
3. Huang, Y. *et al.* An Intrinsically Stretchable and Compressible Supercapacitor Containing a Polyacrylamide Hydrogel Electrolyte. *Angew. Chemie - Int. Ed.* **56**, 9141–9145 (2017).
4. Huang, Y. *et al.* A self-healable and highly stretchable supercapacitor based on a dual crosslinked polyelectrolyte. *Nat. Commun.* **6**, 1–8 (2015).
5. Wang, Z. *et al.* Hydrogel Electrolytes for Flexible Aqueous Energy Storage Devices. *Adv. Funct. Mater.* **28**, 1–30 (2018).
6. Gong, J. P. Materials both Tough and Soft. *Science (80-.)*. **344**, 161–162 (2014).
7. Kwon, H. J., Osada, Y. & Gong, J. P. Polyelectrolyte gels-fundamentals and applications. *Polym. J.* **38**, 1211–1219 (2006).
8. Choudhury, N. A., Sampath, S. & Shukla, A. K. Hydrogel-polymer electrolytes for electrochemical capacitors: An overview. *Energy Environ. Sci.* **2**, 55–67 (2009).
9. Portaccio, M. *et al.* FT-IR microscopy characterization of sol-gel layers prior and after glucose oxidase immobilization for biosensing applications. *J. Sol-Gel Sci. Technol.* **57**, 204–211 (2011).
10. Swift, T., Swanson, L., Geoghegan, M. & Rimmer, S. The pH-responsive behaviour of poly(acrylic acid) in aqueous solution is dependent on molar mass. *Soft Matter* **12**, 2542–2549 (2016).
11. Tsai, J. C., Lo, Y. L., Lin, C. Y., Sheu, H. M. & Lin, J. C. Feasibility of rapid quantitation of stratum corneum lipid content by Fourier transform infrared spectrometry. *Spectroscopy* **18**, 423–431 (2004).
12. Svatoš, A. & Attygalle, A. B. Characterization of Vinyl-Substituted, Carbon-Carbon Double Bonds by GC/FT-IR Analysis. *Anal. Chem.* **69**, 1827–1836 (1997).

13. Tangboriboon, N., Chaisakrenon, S., Banchong, A., Kunanuruksapong, R. & Sirivat, A. Mechanical and electrical properties of alumina/natural rubber composites. *J. Elastomers Plast.* **44**, 21–41 (2012).
14. G. Anbalagana, A. R. Prabakaranb, S. G. SPECTROSCOPIC CHARACTERIZATION OF INDIAN STANDARD SAND. *J. Appl. Spectrosc.* **77**, 124–128 (2010).
15. Lai, S. M. & Li, P. W. Effect of thermoplastic polyurethane-modified silica on melt-blended poly(lactic acid) (PLA) nanocomposites. *Polym. Polym. Compos.* **25**, 583–592 (2017).
16. States of water in different hydrophilic polymers - DSC and FTIR studies. *Polymer (Guildf).* **42**, 8461–8467 (2001).
17. Zundel, G. Hydration Structure and Intermolecular Interaction in Polyelectrolytes. *Angew. Chemie Int. Ed. English* **8**, 499–509 (1969).
18. Kam, W., Liew, C. W., Lim, J. Y. & Ramesh, S. Electrical, structural, and thermal studies of antimony trioxide-doped poly(acrylic acid)-based composite polymer electrolytes. *Ionics (Kiel)*. **20**, 665–674 (2014).
19. Liew, C.-W., Ng, H. M., Numan, A. & Ramesh, S. Poly(Acrylic acid)-Based Hybrid Inorganic–Organic Electrolytes Membrane for Electrical Double Layer Capacitors Application. *Polymers (Basel)*. **8**, 179 (2016).
20. Ryu, S. W. *et al.* Effect of counter ion placement on conductivity in single-ion conducting block copolymer electrolytes. *J. Electrochem. Soc.* **152**, 158–163 (2005).
21. Feng, L., Yang, H., Dong, X., Lei, H. & Chen, D. pH-sensitive polymeric particles as smart carriers for rebar inhibitors delivery in alkaline condition. *J. Appl. Polym. Sci.* **135**, (2018).
22. Průšová, A., Šmejkalová, D., Chytil, M., Velebný, V. & Kucerik, J. An alternative DSC approach to study hydration of hyaluronan. *Carbohydr. Polym.* **82**, 498–503 (2010).
23. Yoshida, H., Hatakeyama, T. & Hatakeyama, H. Characterization of water in polysaccharide hydrogels by DSC. *J. Therm. Anal.* **40**, 483–489 (1993).
24. Legates, D. R. Latent Heat. *Springer* 444–445 (2005).
doi:<https://doi.org/10.1007/1-4020-3266-8>
25. Tanaka, M. *et al.* Cold crystallization of water in hydrated poly(2-methoxyethyl acrylate) (PMEA). *Polym. Int.* **49**, 1709–1713 (2000).

26. Choi, U. H. *et al.* Ionic conduction and dielectric response of poly(imidazolium acrylate) ionomers. *Macromolecules* **45**, 3974–3985 (2012).
27. Diederichsen, K. M., Buss, H. G. & McCloskey, B. D. The Compensation Effect in the Vogel-Tammann-Fulcher (VTF) Equation for Polymer-Based Electrolytes. *Macromolecules* **50**, 3831–3840 (2017).
28. Kumar, R., Subramania, A., Sundaram, N. T. K., Kumar, G. V. & Baskaran, I. Effect of MgO nanoparticles on ionic conductivity and electrochemical properties of nanocomposite polymer electrolyte. *J. Memb. Sci.* **300**, 104–110 (2007).
29. Ramesh, S. & Wen, L. C. Investigation on the effects of addition of SiO₂ nanoparticles on ionic conductivity, FTIR, and thermal properties of nanocomposite PMMA-LiCF₃SO₃-SiO₂. *Ionics (Kiel)*. **16**, 255–262 (2010).
30. Wang, S. *et al.* Highly Stretchable and Self-Healable Supercapacitor with Reduced Graphene Oxide Based Fiber Springs. *ACS Nano* **11**, 2066–2074 (2017).
31. Kwon, S. J., Kim, T., Jung, B. M., Lee, S. B. & Choi, U. H. Multifunctional Epoxy-Based Solid Polymer Electrolytes for Solid-State Supercapacitors. *ACS Appl. Mater. Interfaces* **10**, 35108–35117 (2018).
32. Chen, J. *et al.* Nitrogen-Deficient Graphitic Carbon Nitride with Enhanced Performance for Lithium Ion Battery Anodes. *ACS Nano* **11**, 12650–12657 (2017).